EEG-fMRI: Novel Methods for Gradient Artefact Correction

Glyn S. Spencer, MEng.

Thesis submitted to The University of Nottingham
for the degree of Doctor of Philosophy

May 2015

Abstract

The general aim of the work detailed in this thesis is to improve the quality of electroencepholography (EEG) recordings acquired simultaneously with functional magnetic resonance imaging (fMRI) data.

Simultaneous EEG-fMRI recordings offer significant advantages over the isolated use of each modality for measuring brain function. The high temporal resolution associated with EEG complements the high spatial resolution provided by fMRI. However, combining the two modalities can have significant effects on the overall data quality. The gradient artefact (GA), which is induced on the EEG cables by the time varying magnetic fields associated with fMRI sequences, can be particularly problematic to correct for in experiments containing any subject movement. In this thesis, two novel, movement-invariant methods are introduced for correcting the GA.

The first method is named the gradient model fit (GMF) and relies upon the assumption that the GA can be modelled as a linear combination of basis components, where the relative weighting of each component varies dependent upon subject position. By modelling these underlying components, it is possible to characterise and remove the GA, which is particularly beneficial in the presence of subject movement.

The second method named the difference model subtraction (DMS) relies on the assumption that the GA varies linearly for small changes in subject position. By modelling the change in GA for a basis set of likely head movements, it was shown to be possible to combine DMS with standard GA correction methods to improve

the attenuation of the GA for data acquired during subject movement.

Both methods showed a significant improvement over the existing GA correction techniques, particularly for experiments containing subject movement. These methods are therefore relevant to any experimenter interested in working with subject groups such as children or patients where movement is likely to occur.

Acknowledgements

I would like to express my deepest gratitudes to Prof. Richard Bowtell, Dr. Paul Glover and Dr. Karen Mullinger for their patient guidance, support and advice throughout the last four years. Thank you for all your effort. Without your many contributions and input, this work would not have been possible. I can only apologise for my lack of organisation, I must have driven you all mad! I must also acknowledge the work of Dr. Andrew Peters. The patches he produced for the MR scanner were fundamental to these projects. I wish to acknowledge the work of Alan Dorkes in constructing various pieces of apparatus for my work. I must also acknowledge the people at Brain Products for their valuable input in various experiments and also for funding much of the work. Particular thanks must go to Dr. Robert Stoermer. I am also grateful to the Medical Research Council for financially supporting me throughout this project. Thanks must go to all those who either kindly volunteered for or assisted in the procedure of any of my experiments.

I would also like to especially thank everyone who has been working in the Sir Peter Mansfield Magnetic Resonance Centre over the last four years for all the support, advice and laughs that you have given me. I hope you can forgive me but there are far too many to mention you all by name. Your friendship over the years has been invaluable to me and I have so many fond memories to take away with me. It was an especial pleasure to serve the tea room for the past few years as its quiz master.

It would be impossible for me to not mention the family that I have in Sherwood Hall. I must particularly mention the support, encouragement and mentorship of

Dr. Antonino La Rocca and the friendship of Lamma Zghoul, Emre Gurpinar and Tianshuang Ge. Also, thanks to all the residents of 2013-2014 for giving me just the right amount of excitement (not too little or too much)!

Thank you to the many friends and family who have put up with me over the past few years. You have been there to laugh with me through the good times and carry me through the bad times.

Finally, thank you to my parents (Carol and Michael) who have been supporting me for longer than anyone else. You have always encouraged me in whatever I do and have always been there for me no matter what. I am truly blessed to have such great parents.

Contents

Chapter 1

Introduction

The investigation of the brain is a vast endeavor spanning many varied fields of study; whether it is Psychology, Chemistry, English, Biology, Physics, Philosophy... the list goes on. What is obvious though is that we are fascinated with how our brains work. Recent developments in neuroimaging techniques have opened up new opportunities for understanding the incredibly complex organ housed within our heads. In order to measure the brain function of a subject, two key technologies stand out: electroencephalography (EEG) and functional magnetic resonance imaging (fMRI).

EEG measures the electric field at the scalp of a subject using a set of surface electrodes. Since EEG directly measures voltages generated by neuronal activity in the brain it has a good temporal resolution. However it is unable reliably to localize the active brain tissue that gives rise to the potential measured at the scalp. This is because an infinite number of source distributions can generate the same observed spatial topography on the EEG trace and also because the conductive properties of the skull spatially smear the fields measured at the scalp.

fMRI is a fairly recent technique which takes advantage of the Blood-Oxygen-Level-Dependent (BOLD) effects on the amplitude of the MRI signal. The BOLD effect was discovered in 1990 [1] and refers to a difference in the Magnetic Resonance (MR) signal produced in the presence of oxy- and deoxyhaemoglobin. fMRI

measures and spatially maps the difference in the signal caused by changes in the relative concentrations of oxy- and deoxyhaemoglobin. These changes in concentrations are typically a result of the neuronal activity causing local modulations to the blood flow, blood volume and metabolism within the brain. Therefore, fMRI provides an indirect measurment of the electrical activity of the brain. The disadvantage though is that the temporal resolution of the haemodynamic response is poor and cannot provide much information concerning the timing of the neuronal activity. Also, because the nature of the neurovascular coupling is currently not well understood, it is impossible to draw conclusions concerning the underlying neuronal activity of the brain from fMRI data alone.

The complementary natures of the recordings provided by electroencephalography (EEG) and blood oxygen level dependent (BOLD) functional magnetic resonance imaging (fMRI) make the simultaneous acquisition of the two modalities an attractive option for the non-invasive measurement of human brain activity. The high resolution spatial information provided by fMRI makes up for the inadequate localization of the EEG and the accurate temporal information that EEG provides compensates for the poor temporal resolution of the fMRI data. Therefore, simultaneous acquisition of EEG and fMRI data not only offers an attractive insight into the neurovascular coupling, but also offers a brain imaging modality with high-spatial and high-temporal resolutions. However, due to the interaction between the EEG system and the MR scanner, such a multi-modal approach is technically challenging. The EEG system forms conductive loops via the scalp of the subject, and placing these loops inside a large temporally varying magnetic field causes massive voltage artefacts to be induced on the leads, swamping the EEG signals. While a number of ingenious methods have been developed to counter these artefacts, they still represent a significant challenge to simultaneous EEG-fMRI.

The work presented in this thesis focuses on understanding and correcting the gradient artefact (GA). Typically, the GA varies periodically with the MRI sequence and can readily be corrected by forming and subtracting a template based on av-

eraging across repeats of the GA [2]. However, when subject movement occurs during an experiment, the waveform of the GA can change such that the average template is no longer able to characterise the GA adequately. Therefore the aim of the work here is to understand better how subject movement affects the waveform of the GA and to exploit this understanding in the development of novel methods for correcting GA data corrupted by subject movement.

1.1 Thesis Overview

In addition to Chapter 1 this thesis is made up of the following chapters:

Chapter 2

This chapter provides a basic introduction to fMRI. It touches on the theory of nuclear magnetic resonance and how this phenomenon can be manipulated to form images. Following this is an overview of the mechanisms underlying the BOLD contrast and how this can be used measure changes in brain function. This chapter ends with a section on MRI safety.

Chapter 3

In this chapter the technique of EEG is reviewed, starting with the biophysical origins of the voltages measured at the scalp. Following this is a description of the hardware used to measure these voltages finishing with a brief overview of typical measurements that can be made.

Chapter 4

This final chapter in the background theory explores the combination of the two modalities (EEG and fMRI). The difficulties associated with the hardware compatibility, subject safety and data quality of the modalities are discussed with particular emphasis placed upon the GA. Current hardware and post-processing methods for dealing with the different EEG artefacts, caused the MR scanner environment, are also highlighted.

Chapter 5

The first experimental chapter details the development of a novel, movement-invariant GA correction method termed Gradient Model Fit (GMF). This method takes advantage of the assumption that even in the presence of small subject movements, the GA can be represented as a linear combination of underlying GA components. The GMF method generates models for each of these components which can then be adaptively fitted and subtracted from periods of GA. The method shows a significant improvement over the average template based methods as it is able to characterise the variation in the GA waveform due to subject movement.

Chapter 6

The second experimental chapter details the development of another novel movement-invariant GA correction method termed Difference Model Subtraction (DMS). This method takes advantage of the assumption that the GA varies linearly with small changes in subject head position. Preliminary phantom based work shows that this assumption is likely to be valid provided that the movements are small. The DMS method models the change in GA for a basis set of likely head-movements. These difference models are then adaptively fitted to and subtracted from periods of EEG that have already been corrected by the average template method. The DMS method was able to characterise the residual GA components due to the differences between the template and the GA waveform caused by variations in subject position.

Chapter 7

This short chapter presents some preliminary work comparing the performances of the GMF and DMS methods. The two methods were applied to the same set of recordings from a single subject and the results compared. While both methods outperformed the standard average template based methods, it appeared that the GMF method produced the best results overall.

Chapter 8

In this chapter, a preliminary experiment where the GMF method is applied to a three-dimensional (3D) MRI sequence is detailed. The results suggested that with minor alterations the GMF method can be applied to correct effectively EEG artefacts caused by 3D MRI sequences.

Chapter 9

This chapter summarizes the results of the experiments in Chapters 5 and 6 and presents a general discussion of the work. It includes comparisons with the work of others within the field and talks about some potential applications of simultaneous EEG-fMRI, highlighting the particular strengths and relevance of the methods presented in this thesis. Plans for future work are also discussed.

Chapter 10

This chapter draws general conclusions based upon the work.

Part I

Background Theory

Chapter 2

Functional Magnetic Resonance Imaging

2.1 Introduction

Magnetic Resonance Imaging (MRI) is a powerful, non-invasive and versatile technique for imaging many biological structures. Within diagnostic medicine it has developed into one of the primary imaging modalities, allowing clinicians to detect, characterise and track the evolution of numerous soft tissue pathologies. It is also used widely within research to chart the structure, function and chemical composition of living organisms.

In 1938 Isidor Rabi first observed the Nuclear Magnetic Resonance (NMR) phenomenon in molecular beams [3, 4]. His work was recognised in 1944 by the Nobel Prize Committee. Soon afterwards, in 1946, groups led by Felix Bloch and Edward Purcell independently extended the technique to investigate solid and liquid samples [5, 6]. While the groups differed in their measurement and description of the phenomena it is clear that these experiments were the beginning of the exciting, and still growing, field of NMR.

Many advances within the field of NMR were subsequently made. However, it was not until the early 1970s that the landmark revelation occurred which paved

the way for MRI. It was realised that by spatially varying the magnetic field during NMR experiments 2D images of the samples could be constructed from the recordings [7, 8, 9, 10]. In 2003 Sir Peter Mansfield and Paul Lauterbur were jointly awarded the Nobel prize for their respective contributions to the development of MRI.

In 1990 Ogawa *et. al.* published three papers exploring the effect of blood oxygenation level on the contrast of the MR images [1, 11, 12]. Using high speed imaging sequences these changes in contrast over time could be spatially mapped indicating areas of brain activation. The discovery of this blood oxygen level-dependent (BOLD) contrast created a new tool for researchers to measure the functional activity of the brain.

This chapter begins by introducing basic NMR theory and then building on that foundation to briefly describe some of the principles underpinning MRI. This is followed by a discussion of the hardware involved in recording and generating an MR image. Finally, functional MRI is introduced with a brief description of the underlying biophysics which gives rise to the observable BOLD contrast.

2.2 Proton Nuclear Magnetic Resonance (NMR)

The quantum mechanical property of spin is an intrinsic angular momentum, $\mathbf{J}$, possessed by many atomic nuclei (depending upon isotope). This angular momentum is linearly related to a nuclear magnetic moment, $\boldsymbol{\mu}$, by the gyromagnetic ratio γ [13, 14].

$$\boldsymbol{\mu} = \gamma \mathbf{J} \tag{2.1}$$

In general, MRI is only concerned with the hydrogen nucleus (proton) since it possesses a large gyromagnetic ratio ($\gamma = 42.576\,\mathrm{MHzT^{-1}}$) and is abundant in biological tissues [15]. The proton is a spin-$1/2$ particle and therefore can be characterised by two quantum eigenstates [14]. This means that the z-component of

the angular momentum can be measured with either a parallel orientation (spin-up) or an anti-parallel orientation (spin-down) with respective values $J_z = \pm\frac{\hbar}{2}$, where $\hbar$ is the reduced Planck constant.

When placed within an external, magnetic field, $B_0\hat{\mathbf{z}}$, the energy required to occupy each spin state along the z-axis becomes non-zero and has measurable values $E = -\mu_z B_0$ where the minus sign ensures that the lowest energy state is parallel with the field and the highest is anti-parallel [16]. The difference between the up and down states is therefore $\Delta E = \omega_0 \hbar$ where ω_0 is the Larmor frequency, which is given by,

$$\omega_0 = -\gamma B_0 \tag{2.2}$$

The hydrogen nuclei within an NMR sample prefer to occupy the lowest energy state and therefore there is a tendency for them to align parallel to the field. However, the thermal environment of the sample competes to equalize the populations of the two energy states. When the effects of these factors balance, the sample is in thermal equilibrium and the populations of the two states can be described using Boltzmann statistics. Therefore the polarization of the NMR sample at thermal equilibrium $\mathbf{M}_0$ is given by [14, 17]:

$$\begin{aligned}\mathbf{M}_0 &= \frac{\gamma\hbar\hat{\mathbf{z}}}{2}\left(n_\uparrow - n_\downarrow\right) \\ &= \frac{\gamma\hbar\hat{\mathbf{z}}}{2}n\tanh\frac{\gamma\hbar B_0}{2kT}\end{aligned} \tag{2.3}$$

where $n_\uparrow$ is the number of spins parallel with the field, $n_\downarrow$ is the number of spins anti-parallel to the field, n is the total number of spins, k is Boltzmann's constant and T is the temperature of the sample. For the majority of NMR experiments Equation 2.3 can be approximated to first order as:

$$\mathbf{M}_0 = \frac{n\gamma^2\hbar^2 B_0}{4kT}\hat{\mathbf{z}} \tag{2.4}$$

9

The evolution of the net magnetization vector $\mathbf{M}(t)$ is described phenomenologically by the Bloch equation [6, 16]:

$$\frac{d\mathbf{M}(t)}{dt} = \gamma \mathbf{M}(t) \times \mathbf{B}(t) - \mathbf{R}\left[\mathbf{M}(t) - M_0 \hat{\mathbf{z}}\right] \qquad (2.5)$$

where the matrix $\mathbf{R}$ contains the transverse and longitudinal relaxation time constants, $\frac{1}{T_2}$ and $\frac{1}{T_1}$ respectively.

$$\mathbf{R} = \begin{bmatrix} \frac{1}{T_2} & 0 & 0 \\ 0 & \frac{1}{T_2} & 0 \\ 0 & 0 & \frac{1}{T_1} \end{bmatrix} \qquad (2.6)$$

Transverse relaxation refers to a dephasing of the spins in the transverse plane. This dephasing occurs as a result of the close proximity of individual magnetic moments which give rise to fluctuating dipolar fields that cause the spins to have slightly different precessional frequencies [15]. As a result of these differences in the rate of precession, the spins spread out around the z-axis and the net magnetization in the transverse plane tends to zero. The time constant T_2 is used to describe this relaxation. However, due to the inhomogeneities of the magnetic field the T_2 decay can be shorter than expected. This apparent T_2 is labelled T_2^* [15]. Longitudinal relaxation describes the recovery of the equilibrium magnetization along the z-axis. This is caused by the random motion of the spins within the sample generating local fields which fluctuate at the Larmor frequency [17]. This induces transitions between the up and down states bringing the longitudinal magnetization back into equilibrium.

For $\mathbf{B} = B_0 \hat{\mathbf{z}}$ Equation 2.5 has the following solution:
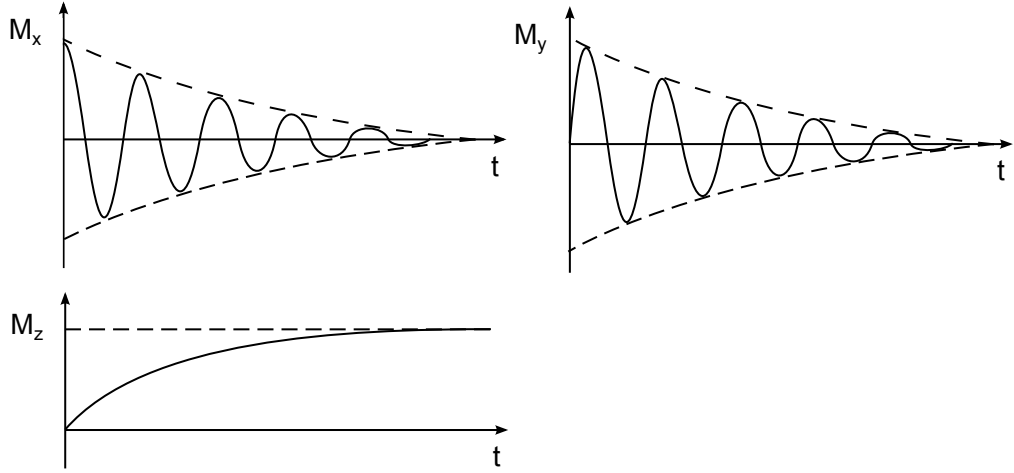
Figure 2.1: The relaxation of the magnetization vector back to equilibrium after the net magnetization has been disturbed such that it has been entirely tipped into the transverse plane. The top graphs show the FID while the bottom graph shows the recovery of longitudinal magnetization (adapted from notes by Granwehr [16]).

$$M_x(t) = \left(M_x(0) \cos \omega_0 t - M_y(0) \sin \omega_0 t \right) e^{-\frac{t}{T_2}} \tag{2.7a}$$

$$M_y(t) = \left(M_x(0) \sin \omega_0 t + M_y(0) \cos \omega_0 t \right) e^{-\frac{t}{T_2}} \tag{2.7b}$$

$$M_z(t) = M_0 - \left(M_0 - M_z(0) \right) e^{-\frac{t}{T_1}} \tag{2.7c}$$

It is clear from this that when the sample is disturbed from thermal equilibrium the bulk transverse magnetic vector $(M_x + \mathrm{i}M_y)$ follows a damped precession around the applied field, $B_0\hat{\mathbf{z}}$, with frequency, ω_0, and the longitudinal magnetization (M_z) steadily recovers back to thermal equilibrium (see Figure 2.1). If a tuned coil is placed nearby such that the transverse magnetization produces a changing flux through the coil, then it is possible to measure an NMR signal. This signal is called a free induction decay (FID) and also has the morphology of a damped oscillation.

In order to disturb the magnetization vector from equilibrium a pulse of circularly-polarized radio frequency (RF) oscillating at the Larmor frequency is applied. This pulse generates a transverse magnetic field (B_1) which rotates around the z-axis

with frequency ω_0 [15]. The magnetization vector $\mathbf{M}$ precesses around this new field as long as the RF-pulse is switched on. A pulse that tips the net magnetization (M_0) entirely into the transverse plane is called a 90° pulse, whereas a 180° pulse is one which simply inverts M_0.

By using the rotating frame (rotating at the Larmor frequency) the RF-pulse can be described as a stationary magnetic field, B_1, along the rotating x-axis. Mathematically this can be written as [16]:

$$\left(\frac{d\mathbf{M}}{dt}\right)_{\text{rot}} = \gamma \mathbf{M} \times \left(\mathbf{B}_0 + \frac{\boldsymbol{\omega}_0}{\gamma} + \mathbf{B}_1\right)$$
$$= \gamma \mathbf{M} \times \mathbf{B}_1 \tag{2.8}$$

with a solution:

$$M_{x'}(t) = 0 \tag{2.9a}$$
$$M_{y'}(t) = -M_0 \sin(\gamma B_1 t) \tag{2.9b}$$
$$M_{z'}(t) = M_0 \cos(\gamma B_1 t) \tag{2.9c}$$

If the RF-pulse is applied for a period of time $t = \tau$ such that $\gamma B_1 \tau = \frac{\pi}{2}$ (a 90° pulse), then it is straight forward to see that $M_{y'}(\tau) = -M_0$ and $M_{z'}(\tau) = 0$.

2.3 Magnetic Resonance Imaging

In the early 1970s both Dr. Paul Lautebur [7] and Sir Peter Mansfield [8] independently discovered that by using magnetic field gradients in an NMR experiment, information about the spatial distribution of the spins within a sample could be recorded. Looking at Equation 2.2 it is quite easy to see that if the magnetic field varies spatially then the resonant frequencies of the spins will also vary spatially.
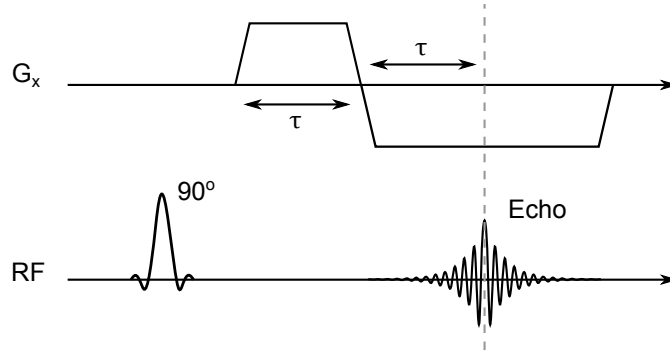
Figure 2.2: A diagram of a simple Gradient Echo experiment. After the application of a 90° pulse a field gradient G_x is applied for a period of time τ. The gradient is then reversed to produce an echo centred at the time point when the time integral of G_x is zero. This is the time when the phase differences of the spins cause by the initial gradient have been rewound to zero.

Therefore, by decomposing an FID measured in the presence of a linear field gradient into its spectral components a projection of the spatial distribution of the sample along the direction of the applied gradient can be observed [7]. It is this basic principle that allows MRI scanners to produce both 2D and 3D images of subjects around the world today.

2.3.1 Gradient Echo

MRI is facilitated by the application of magnetic field gradients across the sample of interest. However, these field gradients cause the FID to decay rapidly. This is because the field is inhomogeneous leading to a T_2^* effect (see Section 2.2). Fortunately the inhomogeneity is well characterised and can easily be reversed by switching the polarity of the applied gradients. This refocuses the spins producing what is called a gradient echo. This refocusing is an important concept underlying many basic imaging experiments. Figure 2.2 illustrates a simple gradient echo experiment. In this example a 90° pulse is used to tip the magnetization into the transverse plane. Afterwards, a linear field gradient is applied along the x-axis causing a rapid decay of the signal. The field gradient is then reversed, removing the position-dependent phase differences introduced by the initial gradient. This

results in a rephasing of the spins causing a gradient echo to form when the integral of the gradient with respect to time is zero [18].

2.3.2 Slice Selection
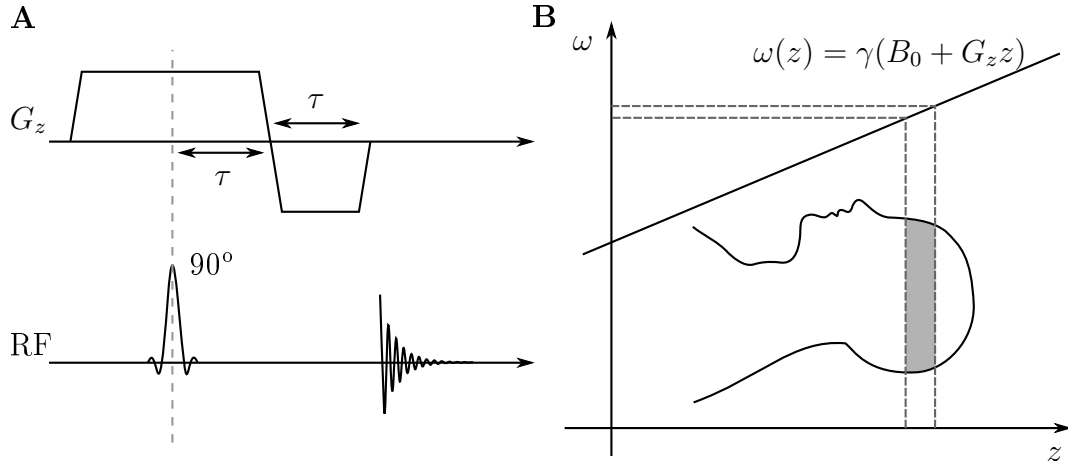
Figure 2.3: Slice selection is achieved by applying a RF pulse during the application of a linear field gradient (**A**) The polarity of the gradient is then reversed to refocus the spins and an FID can be measured. The position of the slice is a function of both the strength of the gradient applied and the chosen frequency band (**B**). By varying the strength of the gradient, the bandwidth of the RF pulse and the centre frequency of the RF pulse the position and width of the excited slice of a subject can be determined.

For most imaging sequences the first step is to excite the spins from a thin slab (slice) of the subject. This can be achieved through selective excitation [9]. From Section 2.2 we know that the application of a 90° RF pulse will excite all the spins which resonate at the frequency components of the pulse. Applying a magnetic field gradient along the z-direction alters the magnetic field such that the spins precess at different frequencies depending upon their position according to:

$$\omega(z) = \omega_0 + \gamma G_z z \qquad (2.10)$$

Therefore, if a linear field gradient is applied along the z-position during excitation, only spins from regions whose resonance frequencies match the excitation frequency components will be tipped into the transverse plane (see Figure 2.3).

14

In an ideal situation, the spectral profile of the RF pulse will be square, leading to a perfectly square 2D slice of the subject being excited. Unfortunately, this requires a sinc pulse of infinite duration to be used, which is not practical to implement. Instead a truncated sinc pulse is typically used and has a spectral profile of a box function with smoothed edges. While this is technically not perfect, it is suitable for imaging experiments.

2.3.3   Frequency and Phase Encoding

To encode the spins in the x-y directions more gradients are applied. To see how these additional gradients affect the recorded signal it is useful to consider the complex form of the transverse magnetization,

$$
\begin{aligned}
M_+(t) &= M_x(t) + \mathrm{i}M_y(t) \\
&= M_+(0)e^{-\mathrm{i}\omega t}e^{-\frac{t}{T_2}}
\end{aligned}
\tag{2.11}
$$

In the presence of a linear field gradient, G_x, the complex signal measured from a large excited volume after demodulation, $S(t)$, can be written as [19, 20, 14]:

$$
S(t) \propto \int M_+(x)e^{-\mathrm{i}\gamma G_x x t}\, \mathrm{d}x
\tag{2.12}
$$

Note that the relaxation term has been neglected for convenience. Substituting $k_x = \gamma G_x t$ produces the following Fourier transform pair:

$$
S(k_x) \propto \int M_+(x)e^{-\mathrm{i}k_x x}\, \mathrm{d}x
\tag{2.13}
$$

$$
M_+(x) \propto \int S(k_x)e^{\mathrm{i}k_x x}\, \mathrm{d}k_x
\tag{2.14}
$$

From this it is straightforward to see that the Fourier transform of the recorded

signal $S(k_x)$ is proportional to the projection of the object along the x-axis. This process is termed frequency encoding.

Encoding in the y-direction is achieved through phase encoding. If a gradient in the y-direction is applied prior to the gradient in the x-direction then the measured signal (recorded during the application of G_x) has a specific phase shift, $\phi = -\gamma G_y y\tau$, where τ is a constant period of time defining the duration of the y-gradient pulse. Since τ is a constant, the phase shift is dependent on the magnitude of the y-gradient. Therefore, by taking multiple measurements with a y-gradient of varying magnitude it possible to collect enough data to construct an image [19, 20, 14]. Such a signal could be represented mathematically as:

$$S(t) \propto \iint M_+(x,y)e^{-\mathrm{i}\gamma G_x xt}e^{-\mathrm{i}\gamma G_y y\tau}\,\mathrm{d}x\,\mathrm{d}y \qquad (2.15)$$

where substituting $k_y = \gamma G_y\tau$ [19] produces the following Fourier transform pairs:

$$S(k_x, k_y) \propto \iint M_+(x,y)e^{-\mathrm{i}k_x x}e^{-\mathrm{i}k_y y}\,\mathrm{d}x\,\mathrm{d}y \qquad (2.16)$$

$$M_+(x,y) \propto \iint S(k_x, k_y)e^{\mathrm{i}k_x x}e^{\mathrm{i}k_y y}\,\mathrm{d}k_x\,\mathrm{d}k_y \qquad (2.17)$$

These equations show that a 2D image, $M_+(x,y)$ can easily be reconstructed from the recorded data $S(k_x, k_y)$ using these encoding regimes.

2.3.4 Spoiler Gradient

After the application of a pulse sequence some residual magnetization is often left in the transverse plane. If not accounted for, this can interfere with the desired MR signal in subsequent acquisitions leading to artefacts in the images [21]. This problem can be resolved by leaving a sufficient time between acquisitions such that the transverse magnetization has been destroyed by the T_2 relaxation processes (see Section 2.2). However, this can increase the scan time. An alternative solu-

tion is to use spoiler gradients. These allow for shorter intervals between adjacent acquisitions. A spoiler gradient is typically applied between separate MR acquisitions to de-phase the spins along the gradient direction, therefore destroying the signal due to any residual, transverse magnetization. The area under the spoiler gradient profile is typically large compared to other lobes in the sequence and can be applied to any single or multiple gradient axes, preferably along the direction which will result in the largest destruction of the signal [21]. For simplicity the polarity of the spoiler gradient typically should match the polarity of the prior gradient lobe on that particular gradient axes [21]. This is so that the de-phasing due to the prior gradient is added rather than cancelled by the subsequent spoiler gradient.

2.3.5   Pulse-Sequences

For mathematical convenience MR researchers have adopted the notation system known as k-space when describing MRI experiments. k-space is defined in the following way:

$$\mathbf{k} = \int_0^t \gamma \mathbf{G}(\tau) d\tau \tag{2.18}$$

From this definition it is straightforward to see that the variables k_x and k_y as defined above are special cases of this notation for constant gradients. The combination of linear field gradients and RF-pulses is known as a pulse sequence. The job of the pulse sequence is to navigate k-space, such that it is adequately characterized for the sample. In the following two sections, two such pulse sequences are introduced.

Gradient Echo Sequence

A gradient echo (GE) sequence is arguably the most basic pulse sequence for acquiring MRI data. The basic sequence is shown in Figure 2.4. First a slice is excited using an RF pulse and gradient. The spins are then refocused along the
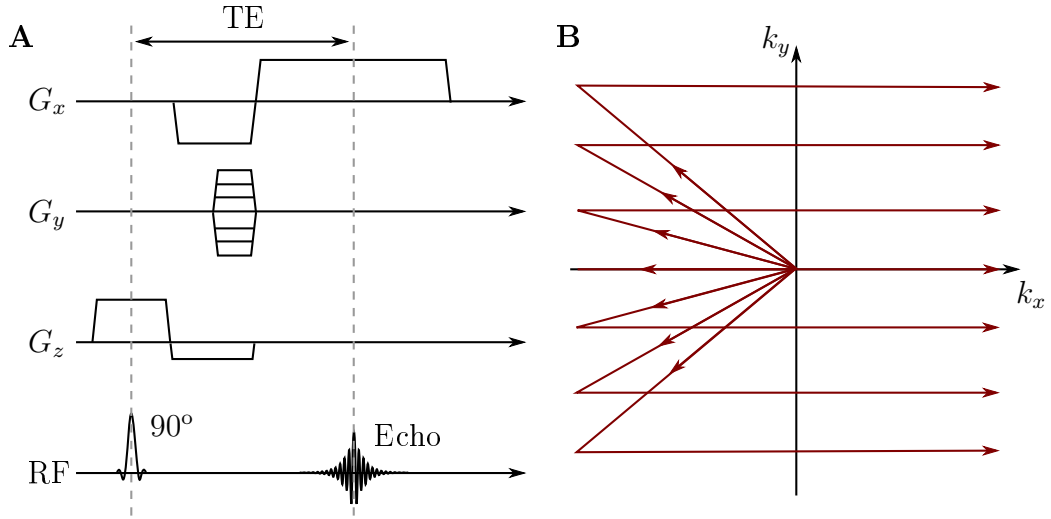
Figure 2.4: **A** shows a standard GE sequence. Selective excitation is used to excite a slice. Phase encoding is carried out on the y-axis prior to data collection during the frequency encoding gradient along the x-axis. The trajectories through k-space are shown in **B** for a variety of different phase encode amplitudes. For illustrative convenience the spoiler gradient has not been included.

slice selection axis (z-axis). A gradient is applied along the phase encode axis (y-axis) along with an initial de-phasing (pre-excursion) gradient lobe along the measurement or read axis (x-axis). The pre-excursion pulse is then reversed and the frequency and phase encoded data is recorded into k-space. TE is the time between excitation and the echo formation. Each run through acquires a single line within k-space. This means that many repeats of the sequence with varying amplitudes of the phase encode lobe are required to characterise the whole of k-space. TR is a variable which defines the repetition time. This is the time period which defines the frequency of the repeated applications of the pulse sequence.

Echo Planar Imaging

Echo Planar Imaging (EPI) is a pulse sequence introduced by Sir Peter Mansfield [22] which allows for the sampling of the whole of k-space rapidly after a single RF excitation. The gradient waveforms used in EPI can be seen in Figure 2.5 and within k-space the gradients correspond to lines as shown in Figure 2.6. After selective excitation, initial de-phasing and pre-excursion gradients are applied
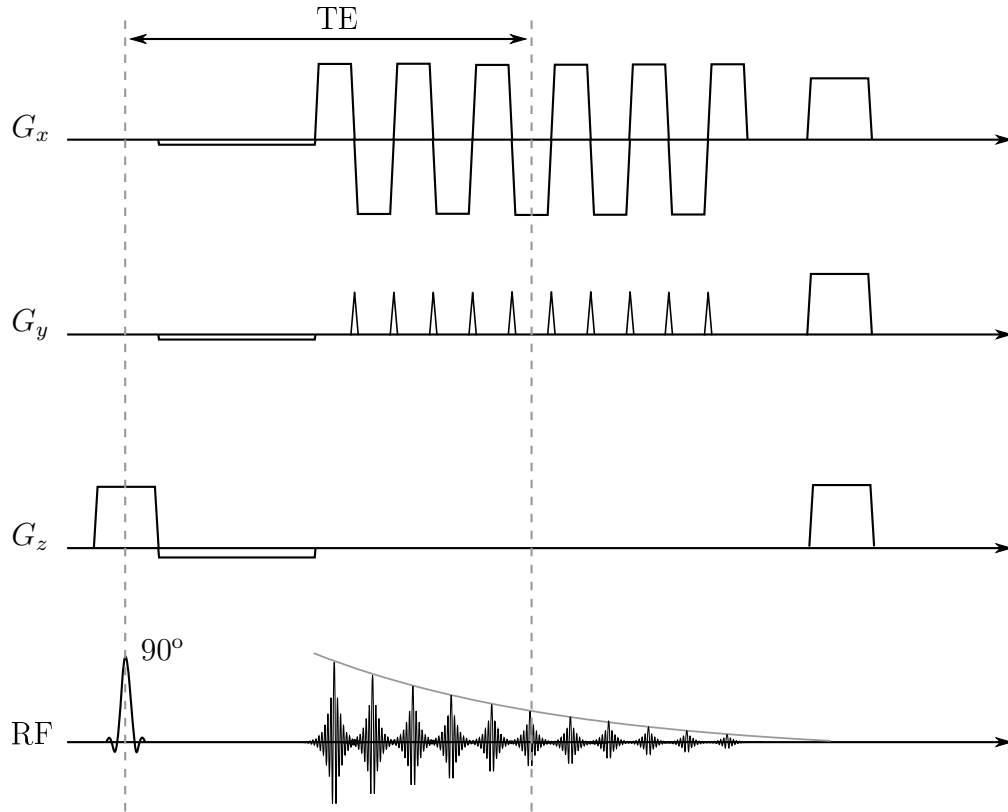
Figure 2.5: A Standard EPI sequence. After slice selection, dephasing and pre-excursion; data are acquired during successive frequency encoding gradients with alternating polarity whilst interspersed with phase encoding blips. Once the whole data set is recorded spoiler gradients are applied along all three gradient axes.

along the y- and x-axes respectively. This takes us to a corner of k-space. A large frequency encoding gradient is then applied along the x-axis sampling from one edge of k-space to the other. Next a phase blip takes us to the start of the next line then the frequency encode gradient is reversed. This process is repeated until the whole of k-space has been filled (Figure 2.5). EPI is one of the fastest pulse sequences available and is therefore advantageous for collecting data rapidly as needed in an fMRI experiment.

2.3.6   Contrast

The contrast within an MR image depends upon a number of different factors. Physiological factors include tissue relaxation times (see Table 2.1 for typical T_1 and T_2 values), proton density (PD) and the local magnetic environment. The

Figure 2.6: The k-space trajectory of a standard EPI sequence

contrast can also be affected by the choice of imaging sequence and associated parameters such as TE, TR and flip angle. The flip angle refers to the angle through 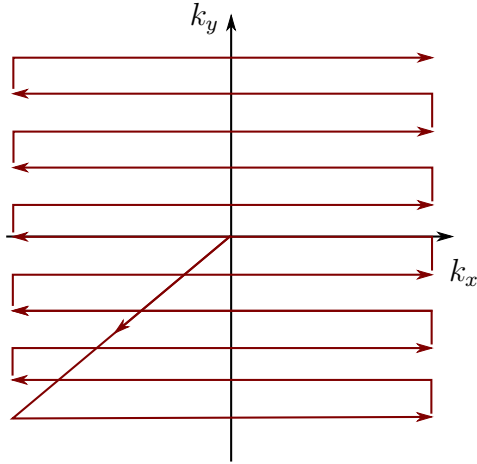which the longitudinal magnetization is rotated by during RF excitation. Although we have only considered RF pulses with flip angles of 90°, in reality other flip angles may be beneficial, depending upon what we are trying to image and what contrast we are hoping to achieve [15]. A short TR will not allow a full recovery of the longitudinal magnetization before the next excitation. This means that the contrast within the image will be affected by the T_1-relaxation times of the tissues. Such an image is called a T_1-weighted image. On the other hand, a long TR will allow a sufficient recovery meaning that the contrast will not be noticeably affected by T_1. By keeping the TR long and altering the TE of a sequence it is possible to produce either a proton-density-weighted (PD) image or a T_2^*-weighted image [15]. For a long TE some transverse magnetization will have been lost to T_2^* processes, thus affecting the contrast between tissues with different T_2^*-relaxation time constants. This produces a T_2^*-weighted image. However, for a short TE, little transverse magnetization will have been lost and therefore the contrast depends more upon the PD than the relaxation times. Hence, this is called a PD-weighted image.

Tissues with different magnetic susceptibilities will have different magnetizations within the main field. This can create magnetic gradients at tissue interfaces and

	Grey Matter	White Matter
T_1	1600 ms	840 ms
T_2	110 ms	80 ms
T_2^*	60 ms	55 ms

Table 2.1: Approximate values for the relaxation time constants of brain tissues at a magnetic field strength of 3T [23].

boundaries. These local inhomogeneities can enhance the T_2^* values and subsequently affect the contrast for T_2^*-weighted images.

2.4 MRI Hardware

An MRI system consists of a number of key components. These include a main magnet, gradient coils and RF coils (see Figure 2.7). A shielded room and a computer based control system are also required.

From the previous sections in this chapter it is easy to see that the main magnet is one of the most important parts of an MRI system because it provides the external B_0-field. While many different types of magnets can be used to provide this static field, the most popular is a superconducting magnet. This is because large and stable magnetic fields can most easily be generated with this type of magnet. In a hospital, a typical MRI system will have a main magnet with a field strength of either 1.5T or 3T. Normally 3T and stronger field strengths are found in research settings. A general principle is that the stronger the B_0-field the greater the Signal-to-Noise Ratio (SNR) (see Equation 2.4). Conversely the stronger the B_0-field the more difficult and expensive it becomes to construct the magnet. In the work presented in this thesis, a 3T Philips Achieva MRI system was used.

In order to make a superconducting magnet, coils typically made of niobium-titanium or niobium-tin alloys are supercooled with cryogens. This lowers the resistance of the coils to zero and an external power source can then be used to raise the magnetic field to the desired strength. Once this has been reached then the magnet is short circuited and the power supply disconnected [15]. Providing the
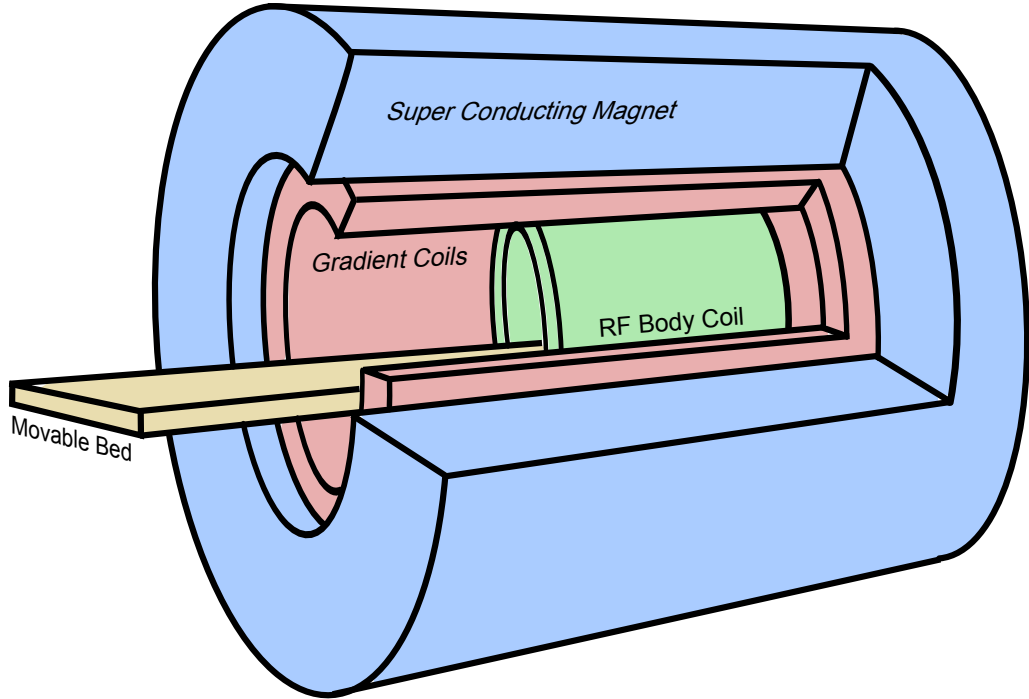
Figure 2.7: Cartoon of some of the key components of an MRI system

magnet remains superconducting, current continues to circulate and the magnet remains at the set field strength.

It is important that the magnet is designed such that the field within the bore is as homogeneous as possible. This is to minimize any signal drop out due to T_2^* effects (see Section 2.2). However, achieving very high field uniformity over a large volume is technically difficult. The most common solution to improving field homogeneity is to shim the magnet. This can be achieved through passive shimming or active shimming. Passive shimming involves placing small pieces of iron within the magnet itself. These pieces of ferromagnetic material produce their own magnetic fields which, if correctly positioned, adjust the overall magnetic field. Active shims are additional coils of wire which are used to generate weak spatially-varying magnetic fields which also interact with the main magnetic field to produce an optimally homogeneous B_0-field [24]. The main, functional, difference between active and passive shimming is that the passive shimming is set by the scanner manufacturer and cannot be changed, whereas the active shims can be adjusted for each subject [20]. Due to the magnetic properties of a subject's tissue and the

surrounding air, unique inhomogeneities can be introduced to the main magnetic field when a subject enters the scanner. Active shimming can be used to counteract this effect.

The gradient coils are used to produce the magnetic field gradients in the x, y and z-directions required to make the MR image as described in Section 2.3. It is important that the fields that these coils produce vary linearly with position. If they are non-linear then significant errors in the spatial localization of the MR signal occur and an accurate image cannot be reconstructed [24, 15]. In order to excite the spins and measure their relaxation, electromagnetic coils called RF coils are used [20]. Care must be taken to design, arrange and tune these coils so that the best possible images can be obtained. For the work described here, 8-channel and 32-channel head coil arrays designed for the Phillips 3T Achieva system were used.

Another important component of any MRI system is the shielded room [24]. Without RF shielding the MRI scanner would pick up any stray RF signals in the area, thus producing artefacts on the image. Doors and windows of this room are designed such that when the room is sealed they prevent RF signals from entering the room. Waveguides are used to pass gas lines and optical fibres through to the scanner from the console room, so that the RF shield is not compromised [24].

The final component of the system is the computer-based control system, which is sited outside the RF shielded room. This controls every aspect of the scanning from the preprocessing to the acquisition and post processing. Once the user has requested the appropriate scan, the control system determines and optimizes the pulse sequence such that the operator's request is carried out. The computer then coordinates the operations of all the hardware components in order excite the hydrogen nuclei and subsequently measure and encode the resultant NMR signal [20]. It then processes the recorded data from k-space to form an image which can be viewed by the operator.

2.5 Functional MRI

MRI is most commonly used to investigate anatomical structure. However, using fast imaging techniques, such as EPI (Section 2.3.5), researchers can also use MRI to map function. One such method is known as functional MRI (fMRI). fMRI is sensitive to changes in the haemodynamics of the brain and since there is a link between vascular and neuronal activities within the brain [25], fMRI provides a measure of the underlying brain function. It is important to note that fMRI does not directly measure the neuronal activity, but is rather an indirect measure of brain activity. Since its conception, fMRI has become one of the most common tools in cognitive neuroscience and it has been used to increase considerably the understanding of human brain function, with over 3000 papers published per year with the key word "fMRI" [26].

For example, fMRI has been used to map the brain's responses to external stimuli, such as visual [27] and tactile [28] stimuli. fMRI has also been used to explore the brain's response to emotional states [29] and to investigate certain pathologies such as epilepsy [30] or persistent vegetative state [31].

In 1936, Linus Pauling and Charles D. Coryell described the magnetic properties of haemoglobin [32]. In particular, they noted a significant difference in the magnetic susceptibilities of oxygenated haemoglobin (Hb) and de-oxygenated haemoglobin (dHb). Hb is diamagnetic and has a similar susceptibility to the surrounding tissue whereas dHb is paramagnetic and has a larger magnetic susceptibility [20]. In 1982, Thulborn *et al.* measured the oxygen dependence of the transverse relaxation time of blood in vitro and showed that increasing dHb produced shortening of T_2^* [33].

In 1990 Ogawa *et. al.* published three papers exploring the effect of dHb on the MR signal [1, 11, 12] showing that the contrast between the blood vessels and rat brain tissue varied as they altered the ratio of Hb and dHb in blood [11]. For increased concentrations of dHB, the vessels appeared darker on the images. They then showed that this contrast was due to the difference in susceptibility between
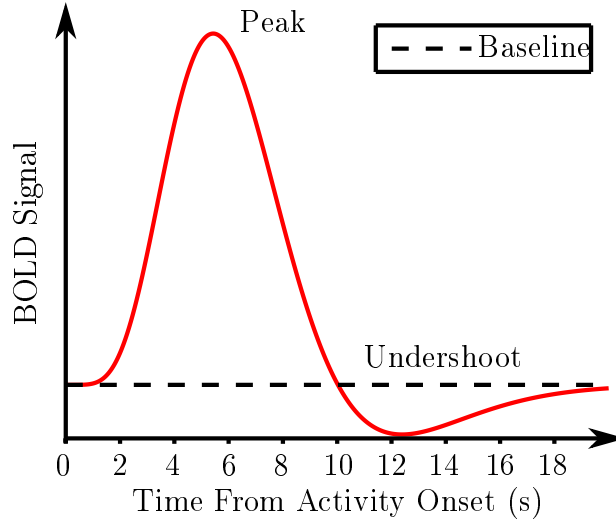
Figure 2.8: Schematic of the BOLD haemodynamic response function to a single short-duration stimulus occurring at time $t = 0$

Hb and dHb [11, 12]. Increased concentrations of dHb affect the homogeneity of the magnetic field in and around the blood vessels. Protons which diffuse through these field gradients experience a T_2^* effect (see Section 2.2). This causes the MR signal to decay more quickly producing a small, localized change in image contrast [20, 11, 12]. The final paper published by Ogawa *et. al.* in 1990 shows how this contrast due to the oxygenation level can be used to indirectly measure physiological changes which affect the level of dHb relative to Hb [1]. This naturally occurring contrast is termed the blood oxygen level-dependent (BOLD) contrast.

Soon after the discovery of the BOLD contrast mechanism, papers began to appear tracking the changes in contrast within the working brain over time [34, 27, 35]. These early studies used visual stimuli to elicit responses. Periods of data with the applied stimulus were compared to periods of baseline showing a clear difference in contrast over the visual cortex between stimulus on and off periods. While nowadays technological advances have improved data collection and more sophisticated methods for analysis are typically employed, the basics of a fMRI experiment remain the same [20]. To characterise the brains response during a fMRI experiment it is necessary to use fast imaging sequences. These tend to be EPI-based, however other fast sequences such as spiral imaging are also sometimes used for fMRI [20].

25

Following a short-duration ($<1\,$s) stimulus at time $t = 0$, local neuronal activity gives rise to a change in the local MR signal. This change over time is known as the BOLD haemodynamic response function (HRF). Figure 2.8 shows a simulated BOLD HRF. After 1-2s the BOLD signal amplitude starts to rise, reading a peak at approximately $5\,$s after stimulus [20]. This appears counter-intuitive as one would expect an increase in neuronal activity to increase the level of dHB and therefore to lead to a signal loss. However, the local blood supply to the active areas of the brain appears to overcompensate for increases in neuronal activity leading to an increase in venous blood oxygenation thus producing an increased T_2^* and therefore an increase in the signal amplitude. After the peak, the HRF falls and undershoots before recovering back to baseline. In some circumstances an initial dip has been observed in the signal over the 1–$2\,$s period immediately after the stimulus application [20, 25].

A link between the haemodynamic response and the neuronal activity is fairly well established, although its precise nature is not fully understood. A simplistic summary is that increases in the neuronal activity increase the local metabolic demand, which is met by the vascular system. This leads to changes in the blood oxygenation (Y), cerebral blood flow (CBF) and cerebral blood volume (CBV) which together produce the BOLD effect. Figure 2.9 illustrates the connection between neuronal activity and BOLD measurements. The cell membrane of a neuron maintains the concentrations of ions inside and outside the cell. This generates a voltage across the cell membrane. There are two main transport mechanisms across the cell membrane; active and passive. Passive transport works by opening and closing ion-specific channels allowing ions to flow freely through the membrane. Active transport uses pumps to force ions, against concentration gradients, into or out of the cell (for more information on the electrical activity of neurons see Chapter 3). It is active transport which creates a demand on the metabolic system. Therefore an increase in neuronal activity leads to an increase in the cerebral metabolic rate of oxygen consumption ($CMRO_2$). Naturally this decreases the level of Y.
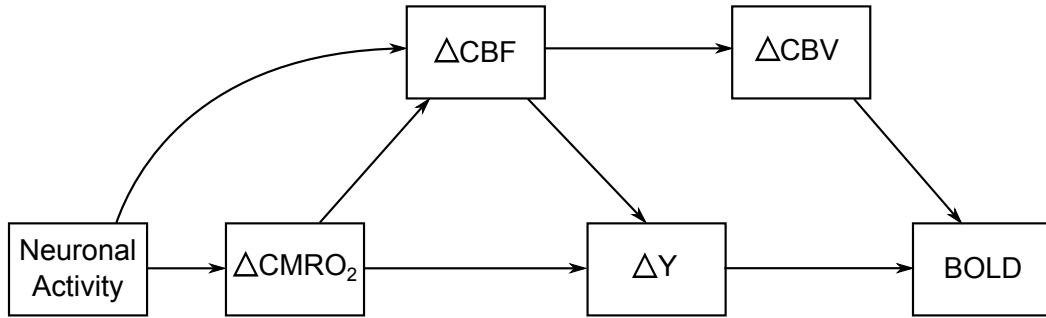
Figure 2.9: Diagram illustrating the relationship between the underlying neuronal activity and the measured BOLD response.

Increases in CBF are thought to be due to decreases in vascular resistance. This is thought to be controlled by the dilation of blood vessels. However it is not entirely clear what influences the diameter of the vessels. Originally it was thought that metabolites controlled this [36], but some more recent studies suggest that synaptic activity (see Chapter 3) may be responsible instead [37, 25].

Increases in CBF cause an increase in Y. This means that changes in Y are proportional to the ratio of the changes in CBF and CMRO$_2$ [25]. In general this ratio is positive because changes in CBF are larger than changes in CMRO$_2$. This leads to an overall increase in Y. The combination of the dilation in blood vessels and the increase in CBF leads to an increase in CBV. It is the combination of the increases in CBV and Y which lead to the increase in the amplitude in the MR signal seen in the BOLD HRF. It is thought that the CBV returns to baseline more slowly than Y, thus leading to the post-stimulus undershoot [25].

An important point to note is that similarly to scalp EEG, the BOLD signals appear to more strongly correlate with postsynaptic potentials rather than action potentials [38, 39, 40].

2.6 MRI Safety

When conducting an MRI experiment on a subject, it is important to consider any safety concerns that may be present. The large magnetic fields associated with the imaging may produce a number of adverse effects for the subject. Here

is a brief summary of the safety issues that are relevant when conducting MRI recordings. A more detailed review of MRI safety can be found at the website MRISafety.com [41].

The high magnetic field strength associated with the static magnetic field creates some safety concerns. The primary risk is that of ferromagnetic attraction [42]. Any ferromagnetic object taken within the vicinity of a scanner will experience a force. If the object is loose then it can become a projectile. This can have painful or even lethal consequences for anyone within the flight path of the object. The static field can also interfere with implants. Certain types of pacemakers may malfunction. Aneurysm clips can be pulled and cause internal haemorrhaging. Any other implants may cause potential hazards, particularly if they are ferromagnetic. Careful screening of anyone who is to be brought within the 5 gauss line of an MRI machine should hopefully prevent any of these hazardous materials from entering the magnet room.

As yet there does not appear to be any long term adverse bioeffects from the static magnet that would cause concern [41, 42]. However, short term effects do exist. Many people have reported experiencing a metallic taste, vertigo or even phosphenes when exposed to the large fields of an MRI scanner. While these effects do not physically harm the subject, it may make them very uncomfortable. These effects are usually minimized by limiting the speed that a subject travels through the static field.

The applied gradients can cause peripheral-nerve-stimulation [43] where the subject experiences tingling or slight tremors in specific regions of their body. At significantly high levels the gradients can cause pain for the subject and at higher levels, the stimulation could potentially interfere with the cardiac system [41, 43]. However, typically the gradients are limited so that there is no significant discomfort for the subject. Also the scanner operator can adjust the pulse sequence so that nerve stimulation is avoided. It is also considered unwise for a subject to cross their arms during an MRI scan since this forms a current loop which increases the possibility of nerve stimulation.

Biological tissues can absorb RF pulses in the form of thermal energy. This effect is characterized by the specific-absorbtion-rate (SAR). SARs above certain values may cause concern for the subject [41], therefore the SAR must be kept below a certain threshold. Also care must be taken so that limbs do not touch. The small contact areas can rapidly heat and cause burns.

The construction of an MRI machine is very similar to a loud speaker, in the sense that there is a static magnet and coils of wire which vibrate when current flows through them. Therefore an MRI scan produces a lot of acoustic noise which can be distressing for the subject. Moreover the noise level is above the recommended threshold for a subject not to wear ear defenders. At higher field strengths it is common for the subject to wear both earplugs and ear defenders. Finally, due to the small bore some subjects experience claustrophobia.

Chapter 3

Electroencephalography

3.1 Introduction

Electroencephalography (EEG) is a method that is used to record the electrical phenomena occurring within the brain. Typically EEG is measured from the scalp, though electrical recordings can also be made invasively using implanted electrodes.

Mass neuronal activity creates time-varying electrical fields which can be measured non-invasively as potential differences across the scalp. Though EEG has been around for many years [44] it remains an invaluable tool for investigating the brain in both clinical and research settings. Clinically, EEG can be used in diagnosing epilepsy, coma, brain death and other encephalopathies [45]. It is also used for extended periods to study sleep disorders [45]. EEG is used extensively in cognitive science, neuroscience, psychology, neurolinguistics and many other areas of research to understand the brain and brain disorders better [45].

This chapter has two major sections. The first part provides a brief overview of the origin and characteristics of the time-varying, electrical signals measured on the scalp. I start with the ionic current flows across the cell membrane and build up to a description of the measurable fields at the surface of the scalp, finally finishing with a short discussion of the rhythmic and transient behaviours of those

fields.

The second section deals with the recording device. Typical EEG hardware and effects on the measurements are briefly discussed.

3.2   Biophysical Origin of EEG

The human brain is a complex processing unit comprising approximately 10^{11} neurons [46]. These neurons communicate with each other by sending and receiving electrical signals. It is these electrical signals which lie at the heart of EEG phenomena.

A neuron is comprised of three principle components, a soma, multiple dendrites and an axon. The soma is the main body of the cell and contains the nucleus and other organelles typical of an animal cell. Dendrites are short branches which extend outwards from the soma. The dendrites are responsible for receiving electrical signals from other neurons via connections called synapses. In the case of a cortical neuron, the dendrites may receive signals from in excess of $10\,000$ other neurons [46]. Finally the axon is a long, thin cable responsible for transmitting electrical signals. Axons may be connected to other neurons by synaptic junctions or to muscle tissue via a neuromuscular junction. Since we are primarily concerned with synaptic activity we will not be considering the neuromuscular junction any further. In some animals the axons can be several metres in length.

Neurons within the brain tend to have two main types of geometries. The first has a spherical distribution of dendrites (stellate cells) while the second has dendrites predominately distributed along one direction (pyramidal cells). Moreover, pyramidal cells tend to be orientated perpendicular to the cortical surface. These two characteristics mean that the scalp potentials are more likely to be due to the net summation of the activity of pyramidal cells rather than of stellate cells. Figure 3.1 shows a schematic diagram of two connected pyramidal neurons.
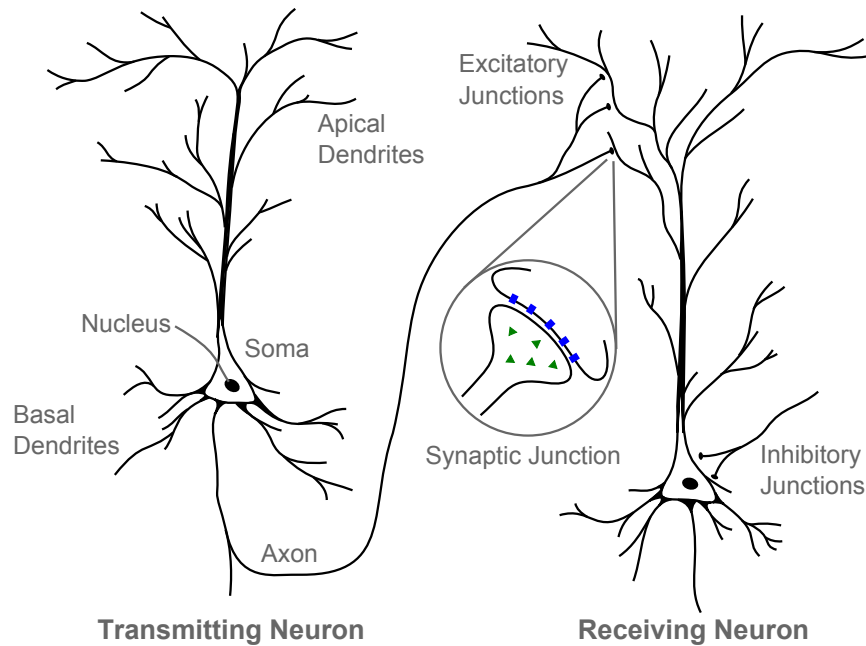
Figure 3.1: Schematic diagram of two connected pyramidal neurons. Pyramidal neurons are characterised by their dendritic structure. A long dendritic stem extends from the apex of the soma with many apical dendrites branching off to form a tuft. Relatively shorter basal dendrites descend from the base of the soma. A single axon descends from the base of the cell, branches and connects via excitatory synaptic junctions to other neurons. A pyramidal neuron receives 30 000 excitatory inputs from synaptic junctions located on the dendrites, whereas it receives 1700 inhibitory inputs from synapses around the soma and axon [47]. See the paper by Spruston [48] for a helpful review of pyramidal neurons.

	Intracellular (mM)	Extracellular (mM)
K^+	397	20
Na^+	50	437
Cl^-	40	556

Table 3.1: Typical ionic concentrations for a giant squid axon. The relative ratios of intracellular to extracellular concentrations are similar to those found in other excitable tissue [49].

3.2.1 Cell Membrane

The cell membrane is comprised of fatty acids known as phospholipids. The phosphoric head is hydrophilic whereas the lipid tail is hydrophobic. This allows these molecules to form a bilayer separating the interior and exterior cellular environments. This bilayer can be electrically modelled as a capacitor where conductive environments are separated by a lipid dielectric. Both modelling work and experimental measurements estimate a typical value of capacitance for the membrane to be around $1\,\mu F\,cm^{-2}$ [49].

The intracellular and extracellular environments contain different concentrations of ions such as sodium (Na^+), potassium (K^+) and chlorine (Cl^-) (see Table 3.1 for typical concentrations for a giant squid axon). The transport of these ions across the membrane is mediated by two distinct mechanisms termed active and passive transport (see Figure 3.2). Passive transport mechanisms consist of ion-specific channels which open and close to either allow or prevent the specific ion from freely diffusing across the membrane. The gating of these channels is generally controlled by either the voltage across the membrane or by the binding of signalling chemicals, such as neurotransmitters. Active transport involves ion pumps which use energy to force ions to flow in a specific direction across the membrane. At rest, these transport mechanisms preserve the concentration differences of each ionic species across the membrane (Table 3.1). This creates a potential difference of approximately -60mV to -100mV [49] across the membrane.

The Nernst potential (E_p) is an electrical measure of the strength of diffusion across the membrane for a particular ionic species (p). It can be thought of as the
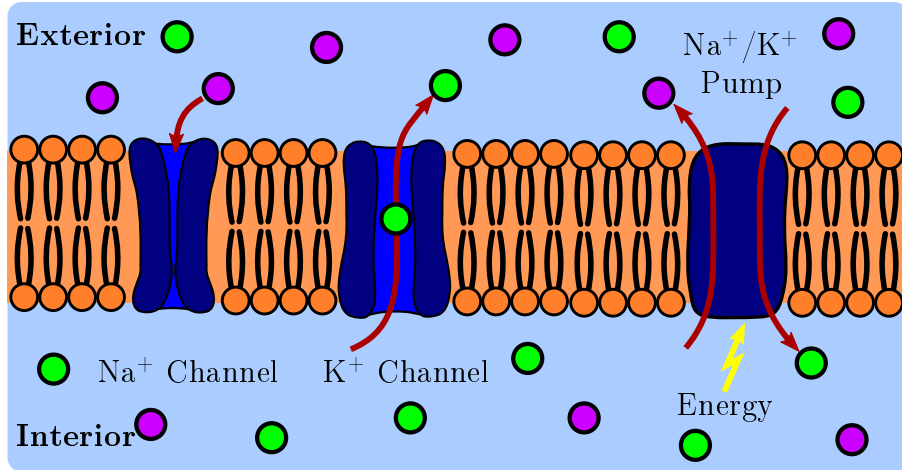
Figure 3.2: A schematic of ion transport mechanisms across an excitable membrane (for simplicity only sodium and potassium ions have been shown). In this case the potassium channel is open allowing potassium ions (shown in green) to diffuse freely across the membrane, whereas the sodium channel is closed preventing the sodium ions (pink) from easily flowing along the concentration gradient. The sodium/potassium pump uses energy to transport both ion species actively against their respective concentration gradients.

potential difference required across the membrane to maintain a given concentration ratio for a particular ion [49]. It is mathematically defined as:

$$E_p = -\frac{RT}{Z_p F} \ln\left(\frac{[C_p]_i}{[C_p]_e}\right) \tag{3.1}$$

where R is the universal gas constant, T is the temperature in kelvin, Z_p is the valence of the ion, F is Faraday's constant and $[C_p]_i$ and $[C_p]_e$ are the intracellular and extracellular ionic concentrations, respectively. Using Equation 3.1, a temperature of 290 K and the ion concentrations for the squid axon in Table 3.1 the Nernst potentials can be calculated to be:

$$E_{\mathrm{K}} = -74.7\mathrm{mV} \quad E_{\mathrm{Na}} = 54.2\mathrm{mV} \quad E_{\mathrm{Cl}} = -65.8\mathrm{mV}$$

Assuming that the transport mechanisms for specific ions are independent of each other a model for the resting potential of a cell membrane can be constructed. This model is known as the Parallel Conductance Model (Figure 3.3). The Nernst
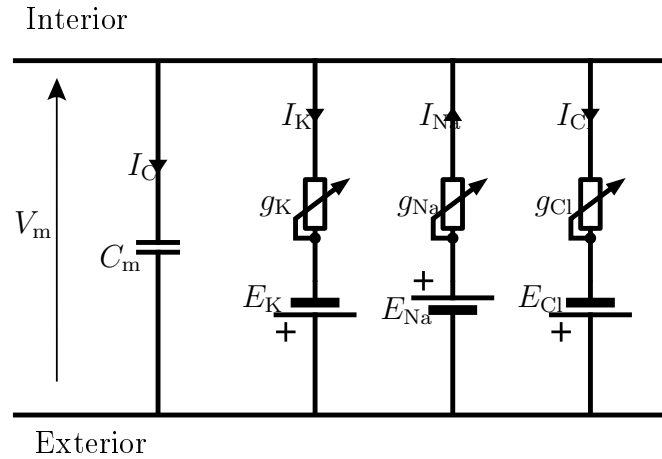
Figure 3.3: The Parallel Conductance Model for a portion of a cell membrane.

potentials represent the ion specific diffusion force and the conductances g_p are coefficients representing the proportionality of the net driving force $(V_m - E_p)$ to the ion flow across the membrane (I_p) [49].

For a giant squid axon, the resting values of the conductances are [49]:

$$g_K = 0.415 \, \mathrm{mS \, cm^{-2}} \quad g_{Na} = 0.010 \, \mathrm{mS \, cm^{-2}} \quad g_{Cl} = 0.582 \, \mathrm{mS \, cm^{-2}}$$

By assuming a steady-state condition with a zero net transmembrane current the parallel conductance model can be used to determine a value $V_m = -68.3 \, \mathrm{mV}$ for the resting membrane potential of a giant squid axon [49].

Due to this steady flow of ions across the membrane, one would expect the concentrations to change such that the Nernst potentials become equal (Donnan equilibrium). However, active transport moves the ions against their diffusion gradients. This mechanism expends energy to maintain the resting ion concentrations. It is the variations in the expenditure of this energy which are thought to contribute to the BOLD effect (see Chapter 2).

3.2.2 Action Potential

At rest, a nerve cell maintains differing ion concentrations either side of the membrane. If the membrane is adequately stimulated, this stored charge is allowed to

generate a transient pulse known as an action potential (see Figure 3.4A).

A membrane can be artificially stimulated by placing fine electrodes inside and outside of the cell. Applying a current between the electrodes alters the transmembrane potential. If the current is altered such that the membrane potential relative to the resting potential is lowered no response is measured. Similarly, if the stimulus current is such that a small increase in the transmembrane potential is observed there is again no response. If however, the stimulus current is increased to a point corresponding to a threshold voltage of approximately $-55\,\mathrm{mV}$, a sudden and rapid membrane response is observed. The membrane potential rises to a peak around $40\,\mathrm{mV}$ then rapidly falls to an after potential which is slightly lower than the resting potential. During this refractory period the membrane then returns back to equilibrium [49].

In 1952 Hodgkin and Huxley used a voltage-clamp to investigate how changes in the ionic flux generate these action potentials [50]. This experiment allowed them to generate a model for the action potential based upon time variations in the sodium and potassium conductances within the parallel conductance model (Figure 3.3). According to their results when a membrane is activated the sodium conductance rapidly increases causing an influx of sodium ions, raising the membrane potential. The potassium conductance increases at a slower rate than the sodium conductance which causes an efflux of potassium ions and lowers the membrane potential to the after potential [49, 50]. As the conductances return to equilibrium the membrane potential also returns to the resting value.

While this model is highly effective it does have some limitations. For example, more than just sodium and potassium channels have been shown to contribute towards action potentials [49].

If a patch of membrane is excited, the membrane potential of adjacent patches increases beyond the threshold voltage triggering an action potential which in turn triggers the next patch and so on. Moreover, patches of excited membrane cannot trigger action potentials in adjacent patches within the refractory period of an action potential's lifetime. This allows the action potential to propagate rapidly
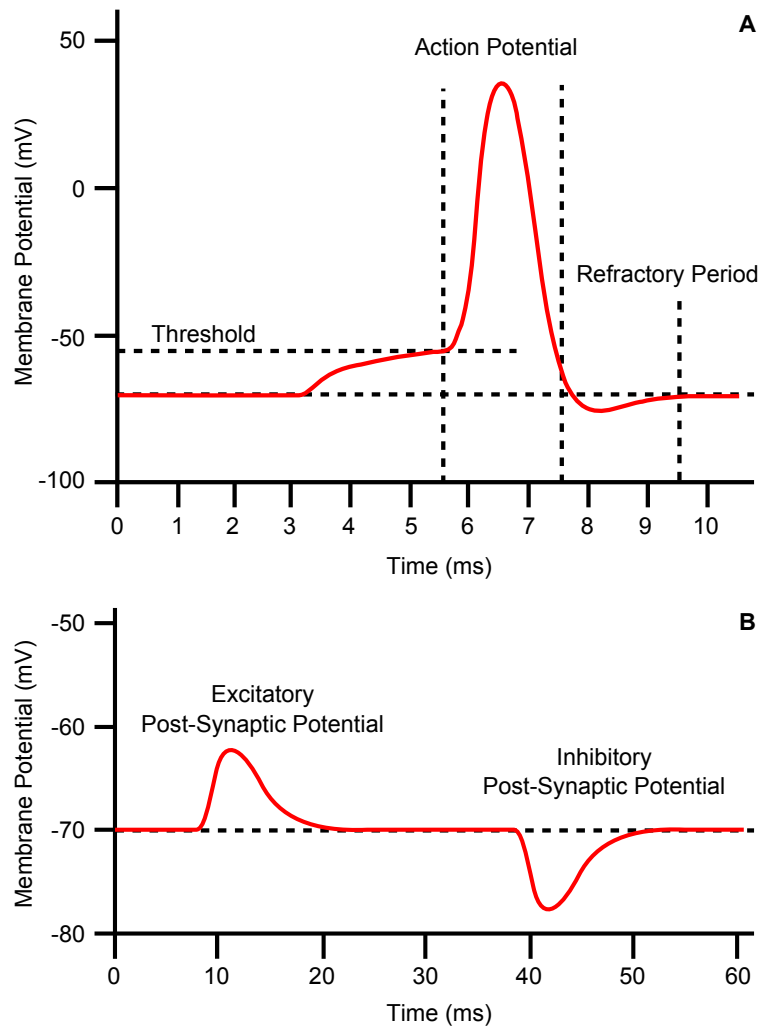
Figure 3.4: A diagram illustrating the two main types of signals found at a patch of excitable membrane. If a membrane is stimulated such that the potential reaches a threshold then an event called an action potential is triggered (**A**). After the spike a refractory period is observed where the ion concentrations either side of the membrane return to equilibrium. The second type of observable signals occur at the synapse and are known as post-synaptic potentials (**B**). These are typically much lower in amplitude but have a much longer duration than action potentials (note the difference in timescales in **A** and **B**). Post-synaptic potentials can either be excitatory, where the membrane is depolarized or inhibitory where the membrane is hyperpolarized.

and unidirectionally away from the point of stimulation.

3.2.3 Post-Synaptic Potentials

Connections between neurons are mediated by synaptic junctions. The axon of a nerve cell is a large cable which terminates with a synaptic terminal. Between the transmitting and receiving cells is a small gap (30–50 nm) called the synaptic cleft [51]. Communication between the two cells is accomplished chemically rather than electrically. When an action potential arrives at a synaptic junction, it triggers the release of neurotransmitters. These neurotransmitters diffuse across the synaptic cleft and bind to the ligand-gated channels of the neighbouring neuron. This opens the ion channels, causing the membrane potential to either increase or decrease depending upon the type of junction. These voltages are known as post-synaptic potentials (see Figure 3.4B).

An event which increases the membrane potential is known as excitatory. This is typically characterised by an opening of both sodium and potassium channels causing the membrane to depolarise [51]. The post-synaptic potential due to a single excitatory synaptic event is typically not capable of reaching the threshold voltage necessary to trigger an action potential. Instead multiple excitatory events must both spatially and temporally sum in order to trigger a action potential in the next neuron.

The other type of post-synaptic potential is inhibitory. This is typically due to the opening of chlorine channels which leads to a hyper-polarization of the membrane [51]. This lowering of the membrane potential serves to hinder the chances of an action potential being triggered.

In general, post-synaptic activity has a significantly larger contribution to the scalp EEG than action potentials [52]. This is for two main reasons. Active synapses generate either a current sink or source depending upon whether they are excitatory or inhibitory [45]. Due to current conservation, these sinks or sources give rise to local sources or sinks away from the synaptic junction [45]. This means

that small current loops are generated. Due to the geometry of the nerve cells the extracellular fields due to the post-synaptic potentials can be modelled as dipolar [45, 53]. This means that the voltage signals decrease with distance according to $^1/_{r^2}$. On the other hand, action potentials, when propagating down an axon, can be thought of as two opposing dipoles separated by a very small distance [51]. This means that when measured from a distance the extracellular voltage can be modelled as quadrupolar with a $^1/_{r^3}$ variation with distance. Therefore the effect of action potentials on electrical measurements at the scalp are very small compared to post-synaptic potentials.

The second reason post-synaptic potentials have a more significant contribution is due to temporal summation. EEG is not sensitive to the activity of single neurons. Instead the synchronous activity of approximately 6×10^7 neurons is required to produce a measurable response at the scalp [45]. Since action potentials are short-lived ($\sim$1 ms) this makes temporal summation more difficult. On the other hand, post-synaptic potentials last ten times longer ($\sim$10 ms). This allows for a greater temporal summation leading to a more significant contribution to the measured scalp potentials.

3.2.4   Electric Fields and Currents within the Head

Within EEG, source localization is about estimating the spatial and temporal dynamics of the macroscopic bioelectric phenomena within the head based upon measurements of the electric potentials observed at the scalp. In this section a brief mathematical basis for relating the current sources due to neuronal activity to the scalp potentials measured by the EEG system is explored. For more thorough treatments of the topic, please see the works of Nunez and Srinivasan [45], Lopez da Silva and Van Rotterdam [53] or Malmivuo and Plonsey [51].

Current Source Field Approximation

It has been shown that the capacitive effects of tissues within the head have a negligible contribution to the description of macro-scale volume conduction when concerned with ordinary bioelectrical phenomena [45, 51, 54]. This means that for the purposes of describing the measured scalp potentials with respect to the membrane currents, the quasi-static approximations of Maxwell's equations can be used [55]. The continuity equation can therefore be written as:

$$\nabla \cdot \mathbf{J} = 0 \tag{3.2}$$

where $\mathbf{J}$ is the macroscopic current density within the head. It has also been shown that at distances from the sites of membrane bioelectrical activity, the current density is linearly related to the electric field $\mathbf{E}$ [56]. Therefore, in regions of the head containing no sources of bioelectrical phenomena, the current density can be approximated as $\mathbf{J} = \sigma \mathbf{E}$, where σ is the uniform bulk conductivity of that region.

Rather than describe the distribution of potential across the geometrically-complex surfaces of cellular membranes it is possible to make use of a conceptual impressed current (also known as a primary current) $\mathbf{J}_S$ to describe the contribution of complex electrical activity of the membrane to the potential measurable at a distance away from the cell. This means that the macroscopic current density can be written as:

$$\mathbf{J} = \sigma \mathbf{E} + \mathbf{J}_S \tag{3.3}$$

Substituting Equation 3.3 into Equation 3.2 and rearranging gives,

$$\nabla \cdot \left[\sigma(\mathbf{r})\nabla\Phi\right] = -s(\mathbf{r}, t) \tag{3.4}$$

Where, $s(\mathbf{r}, t) = -\nabla \cdot \mathbf{J}_S$ is the volume source current with dimensions $\mu A \, mm^{-3}$

and the electric field is replaced with the negative gradient of the scalar potential, $\mathbf{E} = -\nabla\Phi$.

Current Dipole-Moment per Unit Volume

It is clear from comparison that Equation 3.4 is mathematically equivalent to Poisson's equation for electrostatics [45] (Jackson, 1999; Nunez and Srinivasan, 2006). Therefore, the well-established multipole expansions that have been used to express the potential outside of an arbitrary charge distribution can equivalently be used to describe the potential observed outside of a distribution of current sources and sinks. This allows the solution of Equation 3.4 for a distribution of charges centred around the origin for a volume of constant conductivity to be written as:

$$\Phi(\mathbf{r}, t) = \frac{1}{4\pi\sigma}\left[\frac{Q}{|\mathbf{r}|} + \frac{\mathbf{P}(t)\cdot\mathbf{r}}{|\mathbf{r}|^3} + \cdots\right] \tag{3.5}$$

where $\Phi(\mathbf{r}, t)$ is the scalar potential at location $\mathbf{r}$ and time t, Q is the total charge within a volume W and $\mathbf{P}(t)$ is the current dipole moment per unit volume (Figure 3.5). Q and $\mathbf{P}(t)$ are defined as:

$$Q = \iiint_W s(\mathbf{w}, t)\,\mathrm{d}W(\mathbf{w}) \tag{3.6}$$

$$\mathbf{P}(t) = \frac{1}{W}\iiint_W \mathbf{w}s(\mathbf{w}, t)\,\mathrm{d}W(\mathbf{w}) \tag{3.7}$$

where $\mathbf{w}$ is the coordinate that locates the current sources within the volume relative to the centre of the volume. The volume W is chosen to be sufficiently large that local current is conserved within the volume, this means that the number of current sources balances the number of current sinks such that $Q = 0$ [45]. The volume is also chosen to be sufficiently small (millimetre scale) such that the potentials measured at sufficient distance away (centimetre scale) receive a negligible contribution from quadrupole and any higher-order terms from the multipole
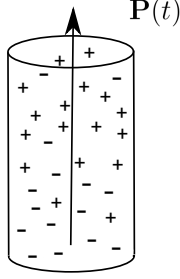
Figure 3.5: A cartoon showing a millimeter scale columnar volume of tissue containing current sources and sinks indicated by the plus and minus signs respectively. The volume of tissue produces a current dipole moment per unit volume $\mathbf{P}(t)$.

expansion (Equation 3.5) [45]. Providing that these two constraints on the size of the volume are true, the dipole contribution towards the scalar potential measured at a distance of $\mathbf{r}$ away from the centre of the volume dominates.

Linking the Dipole-Moment per Unit Volume to Scalp Electrophysiology

By adjusting the definition of the current dipole moment per unit volume to $\mathbf{P}(\mathbf{r}', t)$ such that it is viewed as a continuous function of location, $\mathbf{r}'$ within the brain, it is possible to express the scalp potential at location $\mathbf{r}$ as an integral function of the current dipole moment per unit volume over the whole head (Θ) [45].

$$\langle \Phi_S(\mathbf{r}, t) \rangle = \iiint_\Theta \mathbf{G}(\mathbf{r}, \mathbf{r}') \cdot \mathbf{P}(\mathbf{r}', t) \, \mathrm{d}\Theta(\mathbf{r}') \tag{3.8}$$

where the volume Green's function ($\mathbf{G}(\mathbf{r}, \mathbf{r}')$) contains all the geometric and electrical properties of the head needed to map the source components to the scalp [45]. The Green's function can be thought of as representing the inverse electrical distance between the scalp location $\mathbf{r}$ and the location of the current dipole source $\mathbf{r}'$. Therefore, if the electrical distance between locations $\mathbf{r}$ and $\mathbf{r}'$ is large, the weighting of the contribution of $\mathbf{P}(\mathbf{r}', t)$ within the integral is small.

The goal of the forward problem is to choose an appropriate volume conductor model to provide $\mathbf{G}(\mathbf{r}, \mathbf{r}')$ such that the scalp potentials due to the current dipole

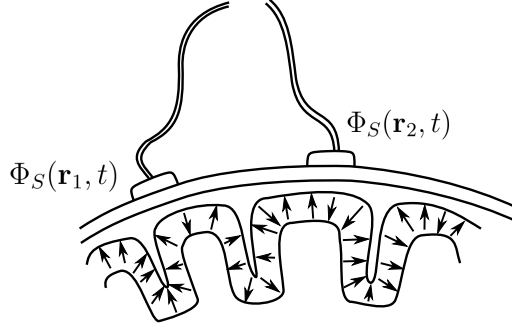$$V(t) = \Phi_S(\mathbf{r}_1, t) - \Phi_S(\mathbf{r}_2, t)$$

$$\Phi_S(\mathbf{r}_2, t)$$

$$\Phi_S(\mathbf{r}_1, t)$$

Figure 3.6: A cartoon showing the measured EEG signal as the difference in potentials at scalp locations $\mathbf{r}_1$ and $\mathbf{r}_2$ which result from a cortical current dipole layer.

sources within the head are appropriately characterised. If one chooses to model the head as an infinite, homogeneous medium, then $\mathbf{G}(\mathbf{r}, \mathbf{r}')$ becomes a very simple function of inverse physical distance between the two locations [45]. However, if one wants to model the head volume conductor more accurately, $\mathbf{G}(\mathbf{r}, \mathbf{r}')$ can become a very complex analytical function. This complexity is because the current path-ways become heavily influenced by the differing conductive and geometrical properties of the various tissues within the head [45].

Given a specified distribution of $\mathbf{P}(\mathbf{r}', t)$ and an appropriately defined head model, the scalp potentials are uniquely determinable. On the other hand the inverse problem is not uniquely solvable: it is not possible, given the scalp potentials and the tissue properties, to determine the source distribution uniquely since multiple distributions can give rise to the same observed scalp potentials.

The measured EEG signal ($V(t)$) is calculated as the potential difference between two scalp electrodes (Figure 3.6).

$$V(t) = \Phi_S(\mathbf{r}_1, t) - \Phi_S(\mathbf{r}_2, t) \tag{3.9}$$

3.3 Measuring Scalp Potentials

To be able to analyse a subject's EEG meaningfully, it is important that the recordings of the scalp potentials are of a high quality. However, because of their low amplitude, these bioelectrical measurements are often affected by a number of sources of interference. Fortunately, much of this interference can be attenuated through careful design of the EEG recording equipment and methodology. Detailed here is a basic discussion of the technological considerations underlying EEG recordings. For a more detailed description please refer to the Chapter "Technological Basis of EEG Recording" by Kamp *et al.* [57].

Electrodes are fixed to a subject's head to record directly the activity at the scalp. For the experiments detailed in this thesis the electrodes were applied using an EEG cap. The positions of the EEG electrodes on the subjects' scalp were based on the international 10–20 system [51], as shown in Figure 3.7.

The electrodes used are generally not in direct contact with the human scalp. In fact, for simultaneous EEG-fMRI it is an important safety consideration that the skin is not in direct contact with the electrode [59] (for a more detailed discussion of safety see Chapter 4). Instead the connection is mediated by an electrolyte gel which ensures a good contact is made between the skin and the electrode. Constant potentials can appear at the interfaces between the electrode and the electrolyte and between the electrolyte and skin [57]. These potentials appear at the amplifier inputs as DC-offsets, which depend upon the temperature, electrode material, the composition of the electrolyte and the local skin condition. This makes it impossible to get actual EEG measurements of the scalp potentials approaching 0 Hz [60]. To minimize these constant offsets, AgAgCl electrodes in conjunction with NaCl electrolyte are typically used and the skin surface is cleaned using alcohol and abraded to remove dead skin. Within this work, impedances of less than $10\,\mathrm{k\Omega}$ were aimed for to provide good EEG data quality [61].

Due to the low amplitude EEG signals, the mains power supply can be a significant source of interference [62]. Figure 3.8 shows how the 50 Hz mains can
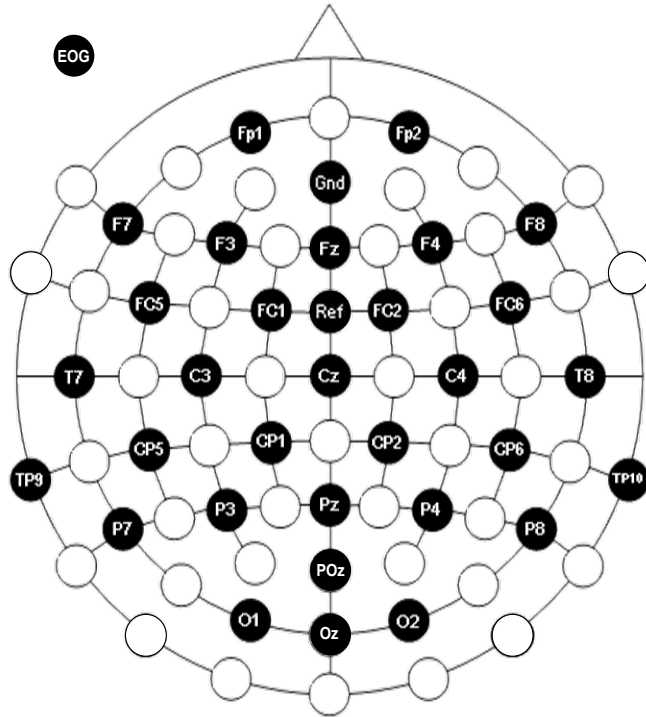
Figure 3.7: The placement of the EEG electrodes used within this Thesis. 31 electrodes are spaced relatively evenly across the scalp with an additional electrode placed under the subject's left eye (EOG). Ground and Reference electrodes are placed at positions AFz and FCz respectively. Diagram adapted from EASY CAP [58].
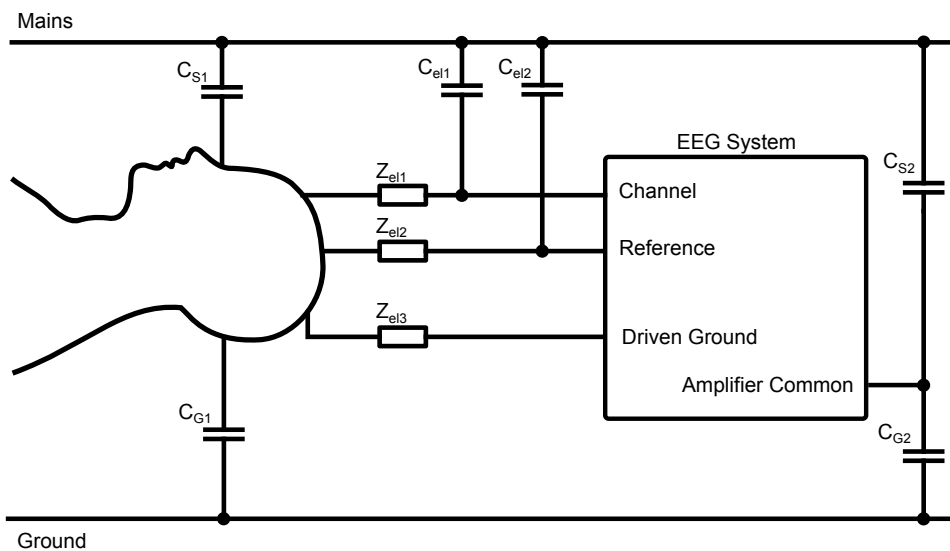

Figure 3.8: A schematic of the EEG measurement system and sources of noise due to capacitive coupling. Based on diagram from [62].

capacitively couple with the subject, the electrode leads and the amplifier common (isolated ground). The capacitive coupling to the electrode leads produces differing currents within the separate leads which, when connected to a subject, can create a significant potential difference which is superposed upon the EEG signals of interest. This source can be attenuated by minimizing the distance between the electrodes and amplifier inputs and ensuring that the impedance values associated with channel and reference connections are as similar as possible [57]. Notch filtering can be used to 'clean up' any mains signals, however this may also attenuate brain signals of interest. Also, use of battery-based systems can be effective in minimizing this interference.

Also, inherent in EEG recordings is the common-mode component, which can be thought of as a background offset that is common to all scalp electrodes. It is primarily due to portions of the currents produced by the capacitive coupling which flow through the ground electrode [62] (Z_{el3} in Figure 3.8) although, static charge also contributes [63]. The common-mode voltages can be suppressed using differential recordings. Here, one of the channels is assigned to be a reference channel and subtracted from all the other EEG channels. This is known as the referential montage for recording EEG signals. This is because every EEG channel voltage is measured relative to a single reference channel. Another popular method known as the bipolar montage also exists. In the bipolar montage, a common reference channel is not used, instead differences between adjacent electrodes are measured. For the work detailed within this thesis, the referential montage was used.

The reference electrode is typically positioned centrally (between the two hemispheres) on the head (as shown in Figure 3.7) or connected to both ears [45]. Figure 3.9 shows an instrumentation amplifier circuit with an active ground to provide additional common-mode suppression. Voltage followers (U_1 and U_2) act as buffers to the differential amplifier (U_3) ensuring a high input impedance. This reduces the voltage drop across the electrode impedance ensuring a larger signal amplitude is measured. U_3 then subtracts the reference signal from the channel

46
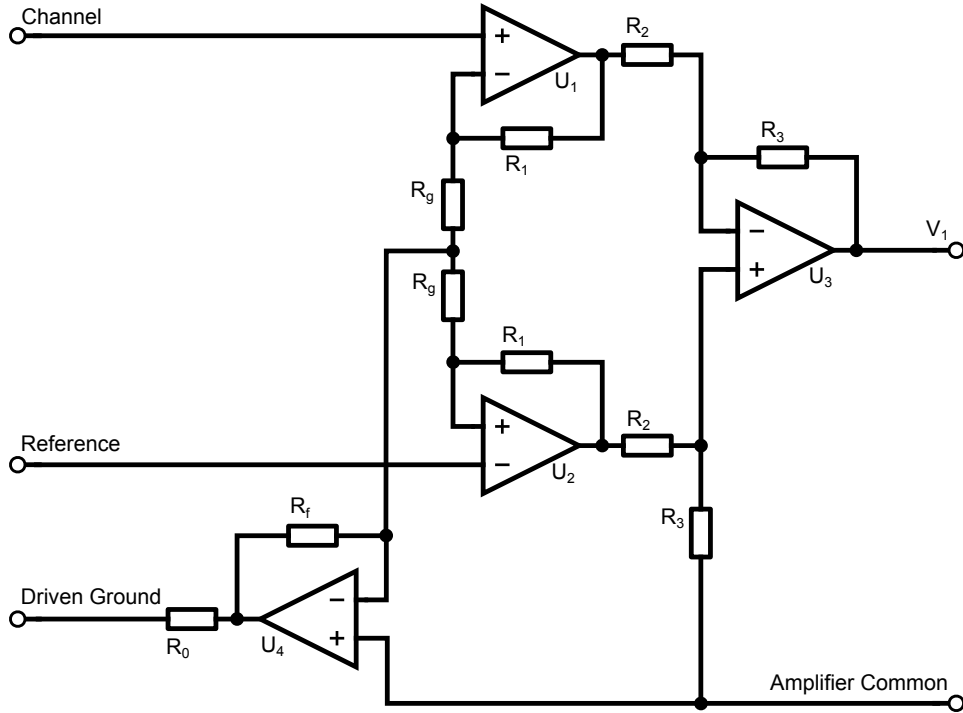
Figure 3.9: A instrumentation amplifier circuit with a driven-right-leg.

signal, amplifying the difference and removing the common component. Providing that care is taken to ensure that the impedances (R_1, R_2 and R_3) match, the common-mode component which gets through the subtraction can be minimized. The MR-compatible EEG amplifiers produced by Brain Products have typical common-mode rejection ratios (CMRRs) of around 90-110dB [64].

In order to improve the CMRR further, a Driven-Right-Leg (DRL) can be used. A DRL is a circuit (U_4 in Figure 3.9) which injects the inverse, average of the channel and reference potentials back into the subject. Since the common-mode component is defined as the average potential of the inputs to the op-amp, by feeding the inverse back into the subject via the EEG ground the common-mode component is minimized [63, 65].

Another source of interference inherent within the electronic amplifier is thermal and flicker noise which additively interfere with the signals [57]. This noise depends primarily upon amplifier design and within the Brain Products MR plus amplifier is typically $< 1\mu V_{pp}$ [64].

The final source of interference is due to changing magnetic fields inducing voltages within the loops formed by the EEG cables. This source can be due to nearby alternating mains currents or high frequency devices [57]. In EEG-fMRI the changing magnetic fields associated with the MRI scanner interact with the EEG producing significant artefacts. It is these artefacts which are of primary concern for the following theoretical and experimental chapters of this thesis.

After the signals have passed through the instrumentation amplifier circuit they are amplified to a suitable level for detection. Before digitization of the signal, it is also passed through a low-pass filter where the cut-off frequency is set such that the Nyquist sampling criterion is satisfied. This is to prevent aliasing of the signal. Once the signals have been reliably recorded they can then be analysed and interpreted by the researcher or clinician.

3.4 Typical Measurements

An important area of EEG analysis is concerned with the spectral content of the measured fields. Synchronized activity of the neuronal sources gives rise to oscillatory patterns. While the generating mechanisms underlying spontaneous oscillatory activity are still very much an active area of research it is possible to divide the signals into separate frequency bands. These characteristic frequencies correlate well with the behavioural context of the subject such as attention or consciousness. Classically, there are five major frequency bands; delta, theta, alpha, beta and gamma. Many other waveform types exist, but only these five will be briefly considered here.

Walter [66] designated the delta band to be frequencies below the alpha band, however now this band is typically defined as 0.5–4 Hz [46]. In the healthy adult, delta activity is primarily related to deep sleep and anesthesia. It is also normal to observe delta in awake children [52]. In the awake adult delta is typically associated with pathologies such as tumours [66]. Possible thalamic and cortical generators of delta have been identified but how these relate to the scalp fields

and subject behaviour are still an area of discussion [52, 67]. The delta activity can easily be confused with physiological artefacts [46].

The theta band covers the range 4–7 Hz and was introduced by Walter and Dovey [68]. Within the healthy adult it appears to be primarily associated with working memory based tasks [67], but also manifests as the brain slips between conscious and drowsy states [46].

The alpha band was one of the first bands to be identified by Berger [44] and has a characteristic frequency range of 8–13 Hz. It is typically modulated by the level of visual attention [67] with the strongest alpha measured in an awake subject with their eyes closed and the largest suppression observed immediately after the subject has opened their eyes [69]. Alpha is usually strongest over the posterior of the head, notably the occipital region [46, 67, 69] and is thought to be primarily generated within the cerebral cortex [67]. The magnitude and frequency of alpha activity can vary significantly within and across subjects [69]. While alpha is most strongly blocked by eye opening it can also be blocked by other sensory stimuli and heightened mental activity [69].

Beta and gamma activities fall into the bands 14–30 Hz and >30 Hz respectively. They are mainly associated with active thinking and attention, a focus on the outside world and solving problems [46], although they are also present during sleep [67]. Beta is also strongly related to motor tasks. Both these high frequency activities are predominantly observed over the frontal and central lobes [46].

There are three main types of EEG recordings [45]: spontaneous EEG, evoked potentials and induced potentials. Spontaneous EEG is data which are recorded in the absence of any stimulus or specific task. Evoked potentials are associated with a specific stimuli such as visual, auditory or tactile. Because these potentials are time-locked and phase-locked to the stimulus they are typically time-averaged over 10–10 000 repeats to remove any spontaneous activity from the data as well as artefacts and noise. Induced potentials, refer to the modulation of oscillatory activity. For example the opening and closing of a subject's eyes modulates the alpha signal. The important difference between evoked potentials and induced

potentials is that induced potentials are not phase-locked. This means they are not amenable to time-average based analyses. Instead the analysis is usually based on averaging the spectral power.

This chapter has summarised the use of EEG to measure the electrical activity within the brain. In the next chapter I will describe how this technique can be combined with fMRI (see Chapter 2) to create a multimodal technique for investigating brain function. In particular I will highlight the advantages and the challenges associated with combining these methods.

Chapter 4

Simultaneous EEG-fMRI

4.1 Introduction

A number of different neuroimaging modalities have been developed for quantifying brain activity. Nowadays there is a drive to combine these modalities with the hope of improving the interpretation of experimental results. This thesis is concerned with the increasingly popular multimodal technique of simultaneous EEG-fMRI.

The complementary natures of the recordings provided by EEG and BOLD-fMRI make the simultaneous acquisition of the two modalities an attractive option for the non-invasive measurement of human brain activity. fMRI captures the haemodynamic responses to neuronal activation with a millimetre spatial precision (see Chapter 2). However, the temporal precision of fMRI is limited by the slow response of the vascular system. Also, because the nature of the neurovascular coupling is currently not well understood, it is impossible to draw conclusions concerning the underlying neuronal activity of the brain from fMRI data alone. On the other hand, scalp EEG measures the voltages at the surface of the head generated by the summed electrical activity of the nervous system to a millisecond precision (see Chapter 3). However, the spatial localisation of the EEG signals within the human head turns out to be an ill-posed, inverse problem which is fur-
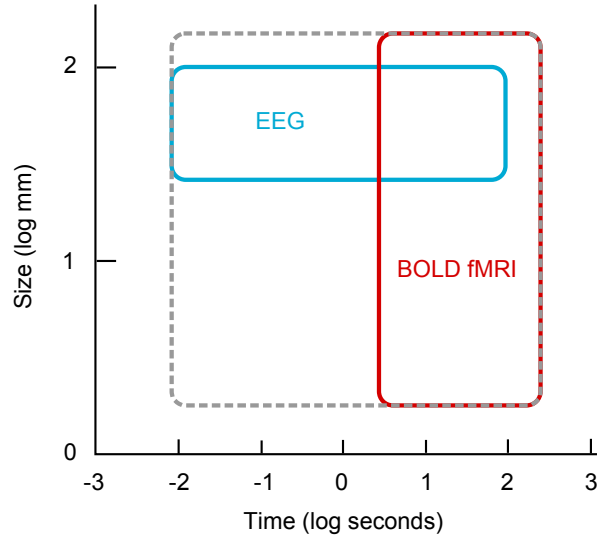
Figure 4.1: The spatiotemporal aspects of both EEG and fMRI. While the combination of the two techniques does not create a hybrid technique that covers the whole area enclosed by the dotted grey outline, the complementarity of the techniques has allowed researchers to make significant advances in the understanding of brain function. This figure was adapted from Snyder and Raichle [70]

ther complicated by the inhomogeneous, anisotropic conductivities of the different tissues within the head. Therefore, simultaneous acquisition of EEG and fMRI data not only offers an attractive insight into the neurovascular coupling, but also offers a brain imaging modality with high-spatial and high-temporal resolutions. Figure 4.1 illustrates the complementary spatiotemporal aspects of the two techniques [70]. Even though the combination of EEG-fMRI may not be able to assess everything within the grey box[1], it is able to explore a larger range of the brain's activity. This has resulted in significant advances within the field of neuroscience.

In the early days, combined EEG-fMRI had a clinical motivation. In particular, it was expected that the combination of the recordings would be able to aid seizure localisation in epileptic patients [71, 72, 73, 74]. Today EEG-fMRI is used in some epilepsy centres around the world in presurgical investigations and Laufs and Thornton [75] predict that in the future it could gain equal status

---

[1]It is possible to improve the spatial resolution of EEG by using intra-cranial recordings, however there is a trade-off as you compromise on having a measurement of the activity of the whole brain.

with other standard presurgical measures that are used today. On top of this, EEG-fMRI has been used in a variety of other ways. For example, simultaneous measurements have been used in the resting state to investigate correlations between the BOLD response and EEG rhythms. In several studies, occipital alpha power has been negatively correlated with BOLD signal in a variety of regions of the brain [70, 76, 77, 78, 79, 80], whereas, Laufs *et al.* [79] showed a positive correlation between beta band activity and the BOLD response in the default mode network. Simultaneous EEG-fMRI has also been used in single-trial-based investigations. Using an auditory oddball paradigm, both Eichele *et al.* [81] and Calhoun *et al.* [82] were able to correlate distinct ERP responses with functional brain structures, though there were some minor discrepancies in the results between the two studies [70].

The data for the combination of EEG and fMRI can be acquired in two different ways. The experiments can either be performed simultaneously or successively. In the successive regime, the experiments are performed on the same subject, but separately for each recording modality. The advantage of this approach is that the two recording technologies do not then interfere with each other. The disadvantages are that it is impossible to say confidently that the subject responded in the same way for each recording modality to capture and this approach cannot be used to study spontaneous, unpredictable variations in responses [83]. In simultaneous acquisition, the experiment is performed once with both modalities recording at the same time. This has the advantage that both modalities measure the effect of the same underlying activity. This makes simultaneous measurements particularly relevant for the investigation of spontaneous, irreproducible functional activity of the brain such as, for example, resting state activity [76, 80, 154, 155, 79, 71, 161] or trial-by-trial fluctuations [81, 163, 164]. Unfortunately the two modalities can interfere with each other producing significant artefacts in both the fMRI and EEG data. The presence of the EEG hardware can cause substantial inhomogeneities in the B_0 and B_1 fields of the MR scanner, consequently degrading the quality of the fMRI data (see Section 4.4). On the other hand the harsh magnetic environment of the scanner induces significant artefacts in EEG recordings, easily swamping

any measurable brain activity (see Section 4.5).

This chapter introduces some of the technical challenges associated with simultaneous EEG-fMRI. The hardware compatibility of the two modalities and safety concerns associated with the combination of EEG-fMRI are briefly covered before looking at how the data of each modality is corrupted by the interaction with the hardware used in recording the other. Methods of reducing or eliminating the artefacts are briefly discussed with the emphasis put on a particular distortion known as the gradient artefact (GA).

4.2   Hardware Compatibility

The bore and immediate vicinity of the MRI scanner must be considered hostile for any measurement devices placed inside. The large, homogeneous, static field can cause ferromagnetic objects to experience a torque or even to become a projectile. It can also magnetise equipment and produce eddy currents within moving conductors, which may affect the performance of devices. The rapid gradient switching (kHz) can generate large electrical signals in conductive loops, in accordance with Faraday's law. Finally the RF pulses can deposit large amounts of energy into highly conductive materials. This can cause significant heating and damage devices.

In all available EEG systems for simultaneous EEG-fMRI, the EEG cap, electrodes and leads, are directly exposed to the large, homogeneous, static field; the gradient switching; and the energy from the RF pulses. While this has some important safety concerns for the subject (see Section 4.3) this can also be a concern for the effective running and performance of the EEG recording device. If the interface to the amplifier is not designed with these hazards in mind, significant damage may be caused to the device [84].

A Brain Products MR-compatible EEG system was used for the work detailed here. Unlike most EEG systems this has been explicitly designed to operate inside the bore of an MRI scanner [84] and has been shown to work up to fields of 7T [85].

Recently, a study has shown that it is possible to use this kit within a static field of 9.4 T [86], although no imaging was reported. The system is modular and is made up of an amplifier unit, battery pack and interface box. Communication between the interface, which sits outside the scanner room, and the amplifier is mediated by fibre-optic cables. This is advantageous as the fibre-optic cables are immune to any interference from the MRI machine. The interface box contains the sensitive electronics, such as the control circuits, and therefore must sit outside the scanner room. This allows the amplifier to be designed to be robust enough to sit inside the scanner bore [84].

4.3   Safety

When conducting any EEG-fMRI experiment, it is important to consider the safety of the subject. As previously discussed in Section 2.6, if appropriate care is not taken the large electromagnetic fields from the MRI environment can present a number of potential dangers to the subject. Moreover, additional hazards may be present due to the inclusion of the EEG system within the field. This section provides a brief overview of the key safety concerns present when acquiring simultaneous EEG-fMRI data.

EEG hardware placed within the magnet room must not contain any ferromagnetic materials. This is not a problem as there are a number of suitable EEG systems available. As stated in the above section, the Brain Products system used in this work has been explicitly designed to operate inside the bore of an MRI scanner [84].

For EEG-fMRI the primary risk is associated with the RF field interaction with the EEG cables and electrodes. Because of their low impedance, the electrodes can produce a high current density in the tissue directly beneath them [84, 87]. This can result in electric shocks, ulcers and burns depending on the frequency of the current [87]. The RF has a reasonable chance of substantially burning the subject if care is not taken to ensure that the impedance of the electrodes is high enough [88, 87]. For example during a Fast-Spin-Echo sequence, it has

been shown that a significant increase in temperature at the electrode site can occur [84]. Lemieux *et al.* [87] describe a method by which the optimal impedance of the electrode can be set by using additional resistors to ensure both patient safety and a reasonable signal to noise ratio (SNR) for the EEG recordings. Cable loops should always be avoided to minimize the RF induction and associated heating.

As a further precaution the subject is monitored throughout the scan and is given a call button to use in the event of an emergency. Provided that appropriate care is taken in the screening, experimental set-up and procedure, there should be no substantial risk to any subjects that undergo simultaneous EEG-fMRI recordings.

4.4 MRI Artefacts

The presence of an EEG cap can lead to observable signal loss in MRI experiments. It has been shown that some types of material used in the construction of the EEG electrodes can lead to appreciable distortions of the B_0-field [89]. If the material used in the wires, electrodes or conductive gels has a significant difference in susceptibility to the tissues of the head, this can lead to inhomogeneities in the B_0-field which in turn affect the local resonance frequency ω_0 (Equation 2.2). However, for commercially available MR-compatible caps with less than 64-channels, such as the one used in the work for this thesis, it turns out that the materials used have little appreciable effect on the B_0-homogeneity; especially when compared to the effects of the different biological tissues within the head [90, 91]. More recently, high density electrode caps (typically 128- or 256-channels) such as those produced by Electrical Geodesics Inc. (EGI), have been used to acquire the simultaneous EEG-fMRI data. These substantially larger electrode nets have been shown to have an appreciable affect on the B_0-field [92].

The primary source of image degradation across all EEG caps appears to be a consequence of the perturbation of the RF excitation field. Differences in the B_1-field lead to local variations in the flip angle. Therefore, there will be local

differences in the strength of the MR signal, affecting the contrast across the image. Induced, surface current densities within the cables can non-uniformly shield areas of the head from the RF pulse [90, 91, 93]. Also, standing waves may be generated when cable lengths are inappropriately chosen, producing large shielding effects [90, 91, 93].

4.5 Origin of EEG Artefacts

Whilst the effects of the EEG system on the MR data quality are manageable, the major problem associated with EEG-fMRI experiments is the EEG data quality. EEG recordings during simultaneous EEG-fMRI experiments are confounded by large artefacts due to the MR imaging sequence, the subject's cardiac cycle and movement of the subject and EEG cables. Often these artefacts are orders of magnitude larger than the EEG signals of interest. Therefore, it is important to understand the origins of these artefacts and correct for them. In this section the causes of the three major artefacts associated with the simultaneous acquisition of EEG-fMRI data are described.

4.5.1 Gradient Artefact

The gradient artefact (GA) is produced by the time-varying magnetic field gradients which form a key element of the applied MR imaging sequence. Conductive loops are formed by the EEG electrode cables and the human scalp. When exposed to a changing magnetic field a voltage is produced in the conductive loops (Faraday's law). This induced voltage depends on the slew rate of the applied MR gradients, the size and position of the effective conductive loop in the applied field gradient, the cable lengths, and the filters at the amplifier interface. The GA is typically orders of magnitude larger than the measured electrical activity of the brain; making true EEG signals difficult to pick out from the noise. Experimental work also suggests that the RF pulse envelope and coil-gating induce artefacts in the EEG recordings (see Figure 4.2 and Chapter 5).
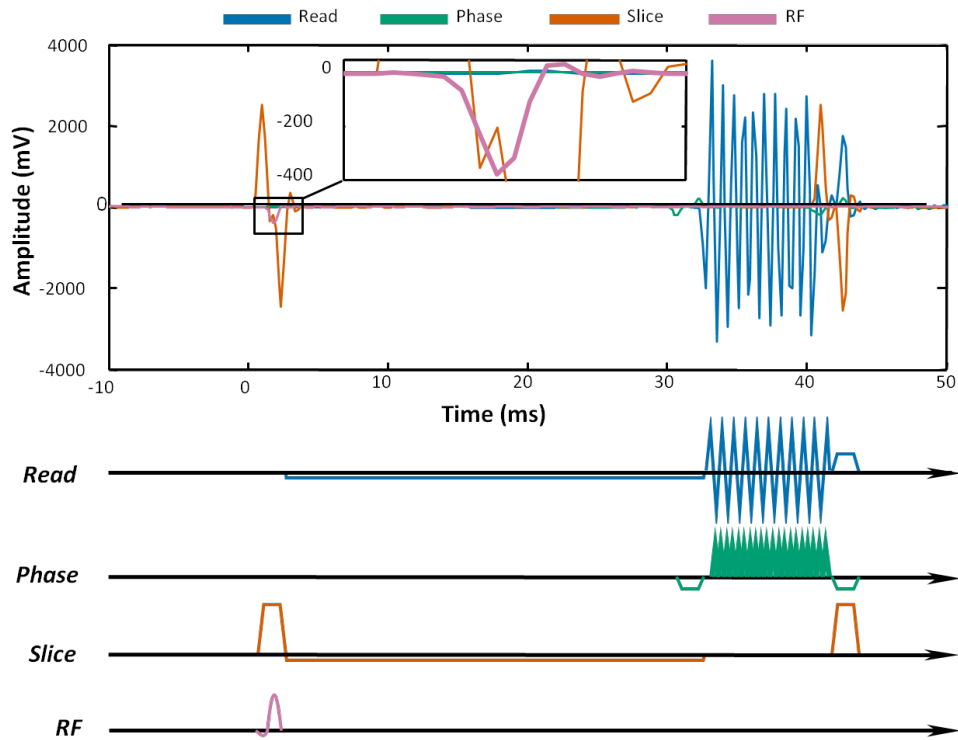
Figure 4.2: Top, recordings of the different GA components of an EPI sequence generated from the EEG data recorded on a phantom (averaged across 31-channels). Inset clearly shows the presence of an RF artefact. Bottom, standard EPI pulse sequence. The GA data were acquired by selectively nulling three out of four of the imaging sequence channels allowing the GA components to be recorded in isolation (see Chapter 5 for more details). Recordings were made on a conducting, spherical agar phantom (20 cm diameter) using a Brain Products 32 channel EEG system (MRplus, $f_s = 5$ kHz, $f_c = 1$ kHz, Syncbox) inside a Philips 3T Acheiva MR scanner during a standard EPI pulse sequence (TR=2s, TE=35ms,voxel size=7x7x7 mm^3, SENSE factor=2).

Theory suggests that the GA can be represented as a linear superposition of individual artefacts caused by the separate components of the imaging sequence [94, 95]. The GA can therefore be approximated by Equation 4.1.

$$s[n] \sim a\frac{\partial G_r}{\partial t} + b\frac{\partial G_p}{\partial t} + c\frac{\partial G_s}{\partial t} + d\frac{\partial G_\gamma}{\partial t} \tag{4.1}$$

Where G_r, G_p and G_s are the magnetic fields due to the Read, Phase and Slice gradients (defined in Chapter 2) respectively and G_γ represents the effects of the RF pulse and coil-gating. The scaling parameters a, b, c and d determine the contribution of each artefact component and vary with respect to position of the conductive paths generated by the subject's head and EEG leads relative to the magnetic field gradients. Figure 4.2 shows recordings of each of the underlying GA components during the acquisition of a single slice of EPI data.

4.5.2 Pulse Artefact

The first studies recording EEG data inside an MRI scanner reported substantial artefacts linked to the subject's cardiac cycle [88, 96]. Originally, this pulse artefact (PA) was thought to be due to a whole-body rocking motion within the static B_0-field inducing currents in the EEG leads [88, 97], much like the ballistocardiogram artefact occasionally observable in traditional EEG recordings [98]. LeVan *et al.* [99] have shown that z-translations rather than rocking motion has more explanatory power regarding the PA. This could be a result of non-rigid-body effects such as cable deformation. While it may be true that a cardiac-related head rotation has a significant contribution to the PA [100, 101, 102, 103], others have proposed alternative or additional causes of the PA.

The pulsatile flow of blood through vessels close to the surface of the scalp causes the shape of the scalp to vary over time. Any electrodes placed within the vicinity of these minor deformations may experience a pulsatile motion. Such movements of the conductive loops within the static field are thought to induce a component of the PA [104, 102, 103].

The third possible source is a result of a Hall effect within blood vessels close to the scalp. According to the Lorentz equation, the flow of charge carriers through a magnetic field will produce an electric field perpendicular to the magnetic field and the direction of the flow of charge [105, 106]. The heart forces the blood, which contains electrolytes, around the body producing an electric field across the blood vessels in which the blood flows perpendicular to the main magnetic field [107]. Although it is thought that this contribution to the PA is relatively small, it is likely that flow-related Hall voltages are recorded at the scalp by the EEG system [97, 104, 103].

Since the PA is dependent upon the interaction of the static magnetic field and the various motions caused by the cardiac cycle, it is always visible in the EEG trace when inside the MR scanner, even when scanning is not taking place. The PA has frequency components within the range of usual EEG data. Since these components fluctuate with the cardiac cycle, the PA cannot strictly be considered periodic, although it is still reasonably predictable. According to Debener *et al.* [102], the amplitude of the PA scales approximately linearly with increasing B_0-field strengths. This was confirmed by Neuner *et al.* [86] up to fields of 9.4 T. Another feature of the PA is that its morphology appears to vary non-linearly between EEG channels [108]. It is unclear why this is the case, it could be related to the equipment, such as deformations of the EEG cables caused by the head-nod leading to non-linear components of the PA. Alternatively, it may be linked to differences in the vascular architecture which may affect the scalp pulsation and Hall effect components. Debener *et al.* [102] have shown that this variability of the PA increased with field strength.

Overall, much progress has been made into understanding the PA, but the exact origins and contributions are still an open question.

4.5.3 Movement Artefact

Any movement of the conductive loops within the static magnetic field may produce artefacts on an EEG recording through Faraday induction. This could be a

result of subject movement within the bore. Any change in the orientation of the conductive path relative to the main field will cause a change in magnetic flux with respect to time producing a current. Another source is the movement of any leads through the inhomogeneous part of the static B_0-field. This particularly concerns leads located close to the ends of the magnet or outside the bore of the magnet.

The most disruptive type of movement to any EEG recordings is "transient, gross head motion" [103] whose frequency of occurrence can be increased due to the subject's discomfort caused by the presence of the EEG electrodes and leads. This can cause artefact voltages which are difficult to characterise and which can be orders of magnitude larger the EEG signals of interest.

Other subject movement artefacts can be caused by more subtle movements such as respiration [103] or swallowing. Technically the PA introduced above is an induced artefact based upon movement of conductive loops, however it is normally treated separately as it is linked to the cardiac cycle and is therefore more predictable. Vibrations due to the MR scanner's gradient switching, cryogen pumps or airflow can also cause artefacts in the EEG recordings [103, 96]. While the cryogen and airflow pumps may be turned off, the gradient switching cannot. However it may be possible to limit the effect of scanner vibration by using a shock-absorbing mattress or by suspending the scanner bed. However, suspension of the scanner bed is likely to be expensive, technically challenging and impractical for most applications.

4.6   Correcting EEG Artefacts

Due to the disruptive nature of the EEG artefacts introduced in the previous section it is important to have robust and effective methods of minimizing or eliminating them so as to recover the EEG data of interest. Introduced here are a selection of methods for dealing with these artefacts.

4.6.1 Gradient Artefact

Over the years a number of methods have been produced to combat the GA. Careful set-up of the experimental equipment and procedure has been shown to reduce the size of the GA. For example, the largest components of the artefact are high in frequency and are usually attenuated by the low-pass filters present in the EEG hardware. Mullinger *et al.* [109] have shown that careful positioning of the subject within the scanner can reduce the GA, reducing the chance of amplifier saturation. Specifically, positioning the subject so that the axial subject position is such that the nasion is shifted $4\,\text{cm}$ towards the feet from isocentre reduces the magnitude of the GA. Also, modification of the EEG lead arrangement has been shown to have an effect on the GA [110]. While these steps significantly reduce the GA, large artefacts, which swamp the neuronal activity of interest, still remain. These can be dealt with in a number of different ways.

Interleaved Acquisition

Initially, simultaneous EEG-fMRI studies relied on recording the EEG data between MR image acquisitions [96]. Although this does not avoid the movement or pulse artefacts, it does mean that the GA is not present. Allen *et. al.* [2] also identified aperiodic fMRI, where the image acquisition is triggered by the observation of an event on the EEG signal which is possible due to the temporal delay in the fMRI response compared to the EEG response. However, this method has its disadvantages. Important EEG data may be missed due to masking by the much larger gradient-induced signals. This procedure also increases the length of the study as a result of the refractory period [2]. Also, artefacts could be introduced to the fMRI data because of differences in the spin history between successive acquisitions. It is therefore often advantageous to remove the artefact from the signal as opposed to circumventing its production by interleaved acquisition.

A more modern approach has been termed the stepping-stone technique [111]. This involves very careful timing of the EEG sampling with respect to the cus-

tomised MRI pulse sequence which contains short quiet periods. By only sampling the EEG at points within the pulse sequence where the GA is expected to be at baseline, the GA can be significantly attenuated. While effective, this method has not proved popular. This is primarily because the pulse sequences need to be carefully re-programmed and strict constraints regarding the timing and shapes of the gradient pulses limit its utility.

Filtering

In most signal processing applications filtering is a natural method for removing unwanted noise or artefacts. While, basic low-pass filtering is generally used as a way of eliminating the high frequency components of the GA and preventing amplifier saturation, lower frequency components overlap with the EEG spectra of neuronal activity. Therefore, low-pass filtering alone is not really a tenable solution to the GA issue [2, 95]. Adaptive noise cancellation techniques have also been proposed, and used in combination with other methods as a means of cleaning up the residuals post-correction [2, 95]. However, I am not aware of any experimental EEG-fMRI data which has been corrected entirely using standard adaptive filtering techniques.

Recording the artefact

Another method for reducing artefacts is to try and replicate the EEG's conductive loop and directly record the artefact. This signal can then simply be subtracted from the EEG trace in order to recover the scalp potentials. For example, Laudon *et al.* [112] used external wire loops placed on top of electrocardiography (ECG) electrodes to record the gradient artefact. The loops are designed and positioned such that they replicate the loop created by the ECG electrodes and the body. Thus the field should induce the same artefact on both loops therefore allowing the artefact to be subtracted from the raw ECG. They used a pork chop as a phantom and found that they were able to provide an effective system for reducing the gradient artefact to 20% of its original value [112]. However this is not enough of an

artefact reduction for recovering an EEG signal [2]. Masterton *et al.* [113] also used wire loops sewn into the EEG cap to measure the pulse and movement artefacts. However they did not employ this technique for gradient artefact removal. The main problem with using overlaid wire loops is that at the scalp there is not a single conductive path in which an emf can be induced, meaning that the artefact cannot be accurately characterised using a wire loop [94].

Using a customised cap, Chowdhury *et al.* [114] were able to successfully record and subtract a number of the EEG artefacts from the recorded data. The cap involved replicating the conductive paths with additional electrodes in the same positions as the standard EEG electrodes, but connected instead to a conductive layer designed to mimic the conductive properties of the scalp. This layer was isolated from the head meaning that the artefacts were replicated without recording the brain signals. While this method looks promising it does require specialized hardware which is currently still within the prototyping stages.

Impulse Response Function

Felblinger *et. al.* [95] describe a method for generating a model of the GA from the impulse response relating the x, y, z-gradient pulses from the MRI scanner to the GA in the EEG recordings. Their study involved recording ECG rather than EEG signals, taking advantage of the short quiet periods of an ECG signal. This enabled them to utilize the property that a convolution in the time domain corresponds to a multiplication in the frequency domain and then to use the Fast Fourier Transform (FFT) to determine the impulse responses for each of the gradients [95]. These impulse responses were then convolved with the pulse profiles outputted by the MRI scanner to estimate and remove the GA in real-time. Obviously EEG recordings do not have a natural quiet period, so Felblinger *et. al.* [95] proposed using a signal averaging algorithm to attenuate the electrophysiological data so that the artefact could be evaluated. Allen *et. al.* [2] raised concerns over this algorithm because the SNR is much lower for an EEG than for an ECG. To the best of my knowledge this method is not currently used by EEG-fMRI groups.

Least Mean Squares Fitting

Sijbers *et. al.* [104] report an interesting method for GA correction. In their paper, they investigated EEG-fMRI data recorded from rats at 7T. They choose intervals based on the MRI scanner sequence timings. They then compute the power spectra and median filter each frequency bin across like intervals to form templates of the GA. The model is then subtracted from the original data with respect to an average scaling factor. This scaling factor is optimized by minimizing the mean-squared-error [104]. They report an improvement in the signal to noise ratio (SNR) by a factor of 4–5. While this method maybe effective for rats, the size of the conductive loops in humans are orders of magnitude larger. Therefore this improvement in the SNR might not be sufficient for recovering the neuronal activity from human experiments [2].

Average Artefact Subtraction (AAS)

The most widely used and accepted method for GA removal is Average Artefact Subtraction (AAS) proposed by Allen *et al.* [2]. This method assumes periodicity in the induced GA and involves generating a template of the artefact by averaging multiple epochs of slice/volume acquisitions of artefact-corrupted EEG data together (see Figure 4.3). The theory is that averaging attenuates the random scalp potentials and retains the periodic GA waveform. This template can then be subtracted from periods of the original artefact-corrupted EEG data to recover the brain signals. We can describe the recorded EEG signal and GA using the following equation:

$$x[n] = s[n] + \varepsilon[n] \tag{4.2}$$

where $s[n]$ is the GA in signal sample n and $\varepsilon[n]$ is a stochastic variable representing the EEG signal and other sources of signal variation. After baseline correction we assume that the mean of ε is $\mu_\varepsilon = 0$. Defining the segment length, M, to be either the slice or volume TR divided by the sampling period, N segments of
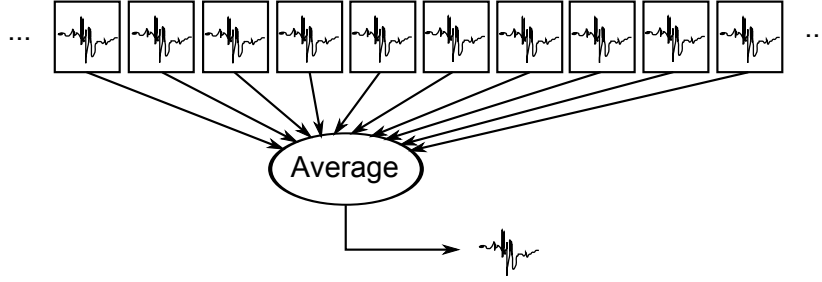
Figure 4.3: The AAS template for the GA is formed by averaging multiple repeats of the artefact waveform together

aligned GA can be averaged to form an artefact template:

$$y[n] = \frac{1}{N} \sum_{l=0}^{N-1} x[n - lM]$$

$$= \frac{1}{N} \sum_{l=0}^{N-1} s[n - lM] + \frac{1}{N} \sum_{l=0}^{N-1} \varepsilon[n - lM] \qquad (4.3)$$

Since, $s[n - lM] = s[n] \; \forall l \in \mathbb{Z}$, $y[n]$ can be rewritten as:

$$y[n] = s[n] + \mathbf{X}_{\varepsilon}[n] \qquad (4.4)$$

where the mean value of the random variable $\mathbf{X}_{\varepsilon}[n]$ is zero and the variance is defined as:

$$\sigma_X^2 = \mathrm{E}\left\{\mathbf{X}_{\varepsilon}^2\right\}$$

$$= \mathrm{E}\left\{\frac{1}{N^2} \sum_i \sum_j \boldsymbol{\varepsilon}[iM]\boldsymbol{\varepsilon}[jM]\right\}$$

$$= \frac{1}{N^2} \sum_i \sum_j C_{\varepsilon\varepsilon}\left[|i - j|M\right] \qquad (4.5)$$

where $C_{\varepsilon\varepsilon}[n_1, n_2]$ is the autocovariance of $\boldsymbol{\varepsilon}[n]$. While adjacent samples of $\boldsymbol{\varepsilon}[n]$ may be strongly correlated, provided that M is sufficiently large and the experiment is

appropriately designed, it is possible to assume a very weak correlation between periods of M samples, i.e. $C_{\varepsilon\varepsilon}[|i-j|M] \approx 0, \forall i \neq j$. This means that,

$$C_{\varepsilon\varepsilon}[|i-j|M] = \begin{cases} \sigma_\varepsilon^2 & \text{if } i = j \\ 0 & \text{if } i \neq j \end{cases} \tag{4.6}$$

and the expression for σ_X^2 can be rewritten as:

$$\sigma_X^2 = \frac{\sigma_\varepsilon^2}{N} \tag{4.7}$$

While this assumption is not valid for all possible values of M, setting M so that $\text{TR}_{\text{slice}} = MT_s$, where T_s is the sampling period, does appear experimentally workable. Once the template is formed, the underlying EEG, $\varepsilon[n]$, can be recovered from $x[n]$ by subtraction.

$$\begin{aligned} \hat{\varepsilon}[n] &= x[n] - y[n] \\ &= x[n] - \frac{1}{N}\sum_{l=0}^{N-1} x[n-lM] \\ &= \varepsilon[n] - \mathbf{X}_\varepsilon[n] \end{aligned} \tag{4.8}$$

where for a large enough value of N, $\hat{\varepsilon}[n] \approx \varepsilon[n]$. The frequency response of AAS (Equation 4.8) can be characterized as:

$$H[\mathrm{i}\omega] = 1 - \frac{1}{N}\sum_{l=0}^{N-1} e^{-\mathrm{i}\omega lM} \tag{4.9}$$

Plotting this reveals that AAS is equivalent to notch filtering harmonics defined by the window length M (see Figure 4.4).

Practical Considerations for AAS   A number of practical suggestions have been made for optimising the application of AAS. One limitation of AAS is that the
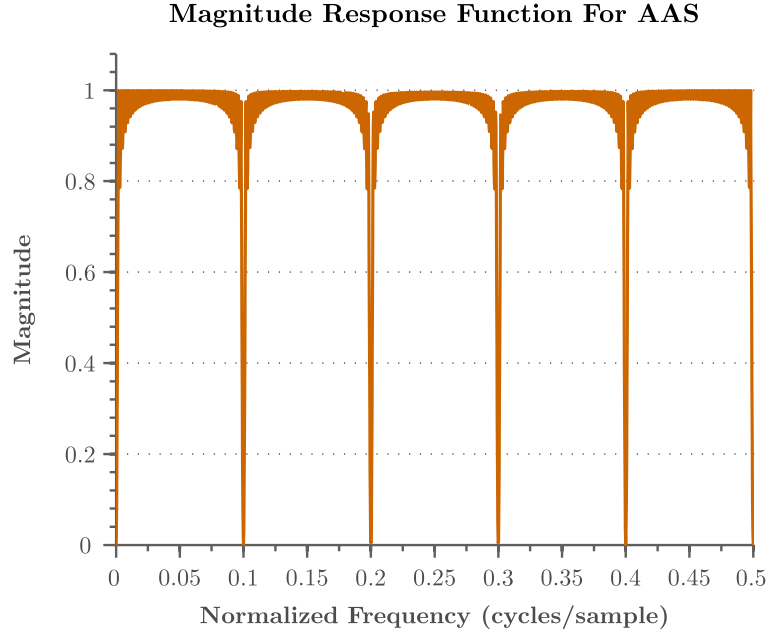
Magnitude Response Function For AAS

Figure 4.4: The magnitude response function for AAS. The template was formed by averaging $N = 50$ epochs. While an epoch length of $M = 10$ is unrealistic for EEG-fMRI recordings, it was chosen here to simplify the diagram.

gradient sequence must be periodic in order to allow formation of a template [2]. This can limit the choice of sequence/sequence parameters. For example, 3D-EPI, where slice-direction phase-encoding varies across time, can be problematic for template formation. Also amplifier saturation must be avoided. This can be done by using a low-pass filter with a suitable cut-off frequency [2], by careful positioning of the subject [109] or by increasing the voxel size, which decreases the gradient slew rates. However, the latter approach is not always sensible as it limits the spatial resolution of the fMRI data.

The formation of an effective template is also limited by the number of segments of GA data averaged together. To attenuate brain signals sufficiently, a minimum of 60 averages is generally required [115]. This corresponds to a scaling of the standard deviation by approximately 0.13 $\left(^1\!/\!\sqrt{N}\right)$.

A large improvement in the performance of AAS can be made by synchronising the clocks of the EEG system and MR scanner [116]. The Brain Products Syncbox takes the 10 MHz MR scanner clock as an input and phase locks the 5 kHz EEG sampling clock to it. This ensures that the sampling of the EEG waveforms is

synchronised with the application of the MR pulse sequence. To ensure effective synchronisation, the slice/volume TR must be a multiple of the EEG sampling period (0.2 ms for the Brain Products system) [116]. For a suitable choice of TR and number of slices, it is helpful to have a knowledge of the MR scanner's time base and rounding precision [116].

For the Philips system it is also necessary to disable some parameters such as dynamic stabilization [116]. Dynamic stabilization uses additional RF pulses to measure and correct for any drift in the Larmor frequency due to local changes in the static magnetic field, for example, due to the heating of passive shims. These additional pulses then affect the slice TR so that it may no longer be an integer multiple of the EEG sampling period.

When designing the experimental paradigm it is important that the timings of any stimulus is not a multiple or a factor of the period of the segments (M). This ensures that any periodic neuronal data is not coherently combined in the formation of the template and thus subsequently subtracted out.

Limitations   In general, AAS works well for correction of the GA. However, when the measured signal is not periodic, the AAS template is no longer able to represent the induced artefact accurately. For example, if a subject changes position then the shape and amplitude of the GA varies. This alters the template so that it does not resemble the artefact before or after the movement thus preventing the algorithm from effectively removing the entire GA (see Figure 4.5).

Also, it is generally difficult to access any brain activity in the spectral bands at frequencies higher than 80 Hz. Small variations in the artefact, usually associated with movement of subject/equipment, cause residuals to be left behind. These tend to be in the gamma band (see Chapter 5 for a more detailed analysis of the effect of movement on the artefact template).

Extensions to AAS   A number of methods have been proposed to deal with the problem of subject movement. For example, it is possible to reduce the residuals
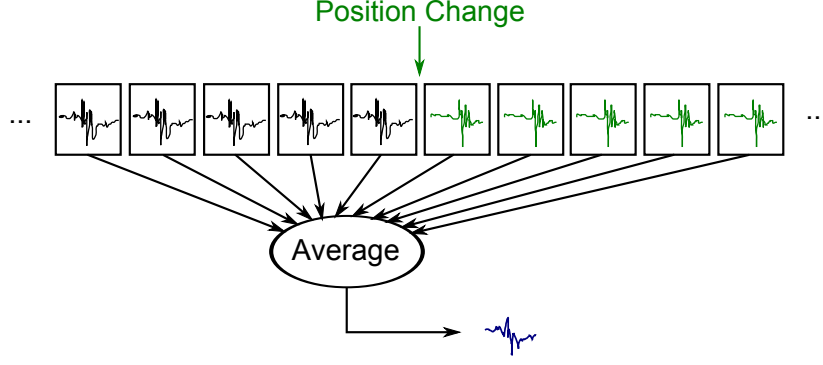
Figure 4.5: The effect that a change in subject position during the experiment has upon the AAS template

by forming a template using a weighted average with weights, w_l [117]. Typically the weights are chosen to exponentially decay such that the intervals nearest the target interval have the strongest weighting. However, this can have implications for the number of intervals required to effectively remove the neuronal data from the template. Rewriting Equation 4.3 as:

$$y[n] = \frac{s[n]}{Z} \sum_{l=0}^{N-1} w_l + \frac{1}{Z} \sum_{l=0}^{N-1} w_l \varepsilon[n - lM]$$

$$= s[n] + \mathbf{X}_\varepsilon \tag{4.10}$$

where $Z = \sum_{l=0}^{N-1} w_l$. The mean and variance of $\mathbf{X}_\varepsilon$ can be calculated as:

$$\mu_X = \frac{1}{Z} \sum_{l=0}^{N-1} w_l \mathrm{E}\{\varepsilon[n - lM]\} = 0 \tag{4.11}$$

$$\sigma_X^2 = \frac{1}{Z^2} \mathrm{E}\left\{ \left(\sum_{l=0}^{N-1} w_l \varepsilon[n - lM] \right)^2 \right\}$$

$$= \frac{\sigma_\varepsilon^2}{Z^2} \sum_{l=0}^{N-1} w_l^2 \tag{4.12}$$

If the weights are normalized, i.e. $Z = 1$

70

$$\implies \sigma_X = ||\vec{w}||\sigma_\varepsilon \qquad (4.13)$$

where $1 \geq ||\vec{w}|| \geq \frac{1}{\sqrt{N}}$. This means that in order to sufficiently attenuate the neuronal signals, more averages may be required. Moreover, a weighted AAS still leaves behind significant, residual GA in samples immediate to the point of subject movement.

A sliding window is often used to form the artefact template [2]. While this does not require more averages (like the weighted average) to form the template, it does suffer the same disadvantage that significant residual GA is left behind near the incident of movement.

Moosmann *et al.* [118] proposed a method for overcoming this problem. They use information provided by an fMRI realignment algorithm to identify where, within the EEG recordings, their subject moved. These points are then used to determine appropriate GA occurrences to average together to form several templates for subtraction. However, problems with this method arise when either multiple movements occur close together, which means that not enough slices are used to create the template or when the subject's position changes slowly and continuously over time. In this case it is difficult to form a discrete number of templates which track the change in the GA.

Freyer *et al.* [119] present a method where the template is formed from only segments which are statistically similar to the section to be corrected. They use a weighted average where the weights decay exponentially with decreasing similarity. This has the advantage that segments with a lower similarity have a less significant contribution to the template formation. However, as described above the weighted average can potentially, inadequately remove the neuronal activity from the template. Also this method will struggle to correct short periods of data where the GA bears little resemblance to any other period within the data set.

Niazy *et al.* [120] proposed an algorithm called FASTR (fMRI Artefact Slice Template Removal). It uses AAS to produce a template and then uses principal com-

ponent analysis (PCA) on the residuals to adjust the estimate for the EEG data. While this method may currently be one of the best approaches for removing the GA it still suffers problems when dealing with significant head movements.

4.6.2 Pulse Artefact

Unlike the GA, the PA is more challenging to characterise since fluctuations in the cardiac cycle and non-linear differences in morphology across channels have an impact on the correction methods. However, adequate removal of the artefact is sometimes achievable. In this section a number of PA removal methods are introduced briefly and discussed.

Averaging

Müri *et al.* [97] present a method for removing the pulse artefact from recordings of *visually-evoked potentials* (VEP) based on averaging. Two sets of recordings are taken inside the scanner, one with the visual stimulus and one without. Both recordings were triggered using an ECG which was used to define epochs which were averaged together. Since the averaged signal with the visual stimulus represented the VEPs plus the PA and the average signal without the stimulus contained just the PA it was possible to recover the VEPs by subtraction. Müri *et al.* [97] expressed concerns that their method would not be suitable for some applications of EEG since the variability of the artefact may produce residuals that obscure any neuronal based EEG signals. It is also questionable whether this method would perform at higher field strengths since the magnitude of the artefact and consequently the magnitude of any residuals increases with the static magnetic field strength [102].

Allen *et al.* [121] also present a similar method based upon averaging. They record the subject's ECG and EEG inside the MR scanner and by identifying the QRS complexes on the ECG recordings, waveforms representing the PA can be segmented in the EEG recordings. A sliding window artefact template is produced

for each channel by averaging the previous 10-second's worth of segmented wave-forms together. This model is then subtracted from each identified artefact in the EEG recordings. Similarly to AAS for GA correction, the optimal basis set extension by Niazy *et al.* [120] has been used successfully to correct for the PA. While this is likely to be the most popular method for PA correction currently, it is unclear how many principal components are required for optimal performance. This means that if care is not taken the method can be susceptible to bias, and over- and under-fitting. Also PCA makes assumptions about the spatial morphologies which may not be true, particularly at higher field strengths.

Fixing the subjects head

Anami *et al.* [100] employed a Vac-Lok system to stabilise the motion of the head and thus to prevent micro-movements from occurring. A Vac-Lok system is a cushion that can be used to fix a subject's position. When inflated it moulds to fit a subject's anatomy and then when the air is removed, it becomes rigid. Their results show a significant reduction in the PA at 1.5T, in some instances to a level where the artefact cannot be identified above the noise. As a result of their system the artefact was reduced enough to be able to read the EEG straight from the data. This verified the theory that micro-movements of the head contribute a significant amount towards the EEG artefact. Although their paper described a significant reduction in the PA, there was not a complete removal of the artefact. This was likely because the Vac-Lok system does not deal effectively with the pulsation nor Hall effect components which also contribute to the overall PA. This approach also may not be comfortable for the subject nor practical to use a head-fixating system for longer scan sessions [121]. Moreover, at higher field strengths, fixation will not likely be good enough as the PA components are much larger.

Recording the artefact

Masterton *et al.* [113] reason that the most substantial component of the PA is due to the deformation or movement of the conductive loops. They try to record this

deformation using carbon-fibre wire loops to replicate the conductive EEG loops so they can adaptively fit and remove the PA using a Recursive-Least-Squares filter. This is advantageous because they are able to also remove effects of subject or cable movement inside the magnetic field. However, this approach is unable to account for components of the pulse artefact due to the Hall effect.

A similar method proposed by Chowdhury *et al.* [114] is able to compensate the rotation and pulsation components using a custom multilayer cap. This method however, is also unable to correct for any components due to the Hall effect and requires specialized hardware which is still in development.

Xia *et al.* [122] also propose the use of a reference layer based system for correcting the PA. In their method they use a standard dense array MR-compatible EEG cap (Electrical Geodesics Inc.) with an insulated damp tissue layer. They perform a preparatory experiment to determine a set of EEG channels which best estimate the PA recorded on the remaining electrodes which are then connected to the scalp. Their results show a significantly greater reduction than those by template averaging based methods, however a cap needs to be constructed from scratch and a preparatory experiment needs to be conducted for every experiment. This is very time consuming and impractical for many EEG-fMRI studies [123].

Luo *et al.* [123] present a reference layer subtraction system which requires only minor modifications of existing dense array EEG caps (Electrical Geodesics Inc.). In their set-up a selection of electrodes are insulated from the scalp and connected to a conduction layer. The recordings from the electrodes are then linearly fitted and subtracted from the scalp connected channels. The results show a good improvement to the EEG quality. An advantage of this method over other reference layer based techniques is that it is relatively straightforward to adapt the existing technology and adds little extra time to the procedure. While this method favours the dense array EEG caps, comparable results on 64-channel Brain Products caps were also found. Disadvantages with this method as with all the methods in this section are that it does not characterise the Hall effect component of the PA. However, a subsequent application of AAS may offer additional improvements.

Also this method assumes that the PA is linearly related across the scalp, but this assumption may not be valid. It would be interesting to see whether additional non-linear components within the model would produce better results.

Independent Component Analysis

Independent Component Analysis (ICA) has been used to remove the PA however with mixed results. Groups have reported success at 1.5 T [101, 124, 81, 125, 126], but at higher field strengths the quality of the results decreased [127]. An assumption of the ICA method is that the linearly mixed signals are spatially stationary. However, the spatial variability in time of the PA increases with field strength [102]. This means that for higher field strengths ICA methods are generally not robust enough to deal completely with the PA. However, using ICA in combination with other methods such as AAS does appear to be an advantageous approach to removing the PA [103, 127].

Optical Tracking

LeVan *et al.* [99] used an optical tracking system, with a marker placed on the subject's forehead, to determine head movements that contribute to the PA. Temporal derivatives of these movements were then regressed from instances of the PA. A surprising result is that the z-translation was able to account for the majority of the artefact, contradicting what simulations suggest [128]. However this discrepancy is likely to be accounted for by non-rigid body motion such as cable movements. Their results suggest an excellent removal of the PA. This method does not account for the scalp expansion and Hall effect components of the PA. When used in combination with AAS, which can correct the components of the PA due to scalp expansions and Hall effects, they report an almost complete removal of the PA. This method does unfortunately require specialized hardware again, and the motion tracking can be susceptible to spurious results due to movements of the forehead, such as frowning.

4.6.3 Movement Artefact

Generally the movement artefact is the most challenging to deal with using post-processing techniques. Unlike the GA and in many respects, the PA, the movement artefact is not predictable and therefore is difficult to characterise. This often results in the discarding of data. The most effective way of dealing with this artefact is to restrict movement of the head and the EEG cables [103].

Using conductive loops Masterton *et al.* [113] were able, fairly successfully, to record the motion artefact and remove it from the EEG trace. However the filter is not able to effectively track and remove excessive motion of the head. More recently, Chowdhury *et al.* [114] used a multilayer cap to record and subtract the effects of the movement artefact.

Many of the technical challenges associated with simultaneous EEG-fMRI have been covered in this chapter. While much headway has been made there are still limitations of current GA correction mechanisms, particularly when subject movement occurs, affecting the quality of the EEG data and the accessible bandwidth of EEG signals. In the following chapters two new methods for correcting/removing the GA from recordings affected by subject movement are presented.

Part II

Experiments

Chapter 5

Gradient Model Fit (GMF)

5.1 Introduction

Simultaneous acquisition of EEG and fMRI data offers an increased insight into brain function due to the complementary temporal and spatial properties of the two modalities (see Figure 4.1). However, as previously discussed (see Chapter 4), this multi-modal approach is often confounded by large EEG artefacts caused by either motion within the static field of the MR scanner (pulse and movement related artefacts) or by the time-varying electromagnetic fields used in fMRI (gradient artefact [GA]). Typically the GA is corrected by a template-subtraction-based technique known as average artefact subtraction (AAS) [2]. However, as mentioned in Chapter 4, the performance of AAS is severely compromised by subject movement. In order to deal with this problem, a number of improvements to AAS have been suggested [2, 117, 118, 119]. However, as previously discussed, these methods have their respective disadvantages and large residual GA resulting from the compromising effect of subject movement is often still a problem.

A new approach to correcting the GA called the Gradient Model Fit (GMF) is introduced in this chapter. The GMF method takes advantage of the reasoned idea that the GA can be represented as a linear superposition of individual artefacts caused by the separate components of the MRI sequence [95, 94] (see Chapter 4

and Figure 4.2). In implementing the approach, the artefacts due to these separate components are isolated from each other, recorded and processed to form a set of models. These models are then combined to form a general linear model of the GA from each slice acquisition. Using a customized, regularized least-squares method the gradient models are then fitted and subtracted from EEG data recorded simultaneously with fMRI to correct the GA. A particular benefit of the GMF method is that it can accommodate variation in the GA due to head movements.

In the first section of this chapter a theoretical exploration of how movement can affect the performance of AAS is described. The theory underlying the GMF method is then covered. Two different approaches for forming the models used in GMF are introduced. The first, which from now will be referred to as GMF, requires the data for forming the models to be recorded during the same acquisition as the experimental data. The second, which is termed high-temporal-resolution GMF (HTRGMF), allows the data for the models to be acquired during a separate acquisition to that of the experimental data. In the following sections both the HTRGMF and GMF methods are used to correct the GA in the presence of subject movement and the performance is compared to conventional AAS.

5.2   Theory

As previously mentioned (see Chapter 4), it has been suggested that the GA can be represented as a linear superposition of individual artefacts caused by the separate components of the imaging sequence [95, 94]. Therefore the GA can be described by using a linear equation (see Equation 4.1). This linear equation for the GA ($s(t)$) on a particular EEG channel can be written in the following way:

$$s(t) = \vec{\mathbf{G}}(t) \cdot \vec{\boldsymbol{\alpha}}(t) \tag{5.1}$$

where,

$$\vec{\mathbf{G}}(t) \cdot \vec{\boldsymbol{\alpha}}(t) = \begin{pmatrix} \dot{G}_r(t) \\ \dot{G}_p(t) \\ \dot{G}_s(t) \\ \dot{G}_\gamma(t) \end{pmatrix}^{\mathrm{T}} \begin{pmatrix} a(t) \\ b(t) \\ c(t) \\ d(t) \end{pmatrix}$$

where $\vec{\boldsymbol{\alpha}}(t)$ and its constituents depend upon the paths of the EEG leads and the shape of the volume conductor and $\vec{\mathbf{G}}(t)$ is a vector containing the time derivatives of the field gradients and RF pulse applied by the MRI scanner. Using a simple model it is possible to show that Equation 5.1 makes sense theoretically. Bencsik *et al.* [129] have shown that the magnetic field produced in the centre of a set of gradient coils is linearly dependent upon position. Using their expressions, the magnetic field due to the gradients applied along the three orthogonal axes can be written as:

$$\vec{\mathbf{B}}(t) = B_0\hat{\mathbf{z}} + G_\mathrm{x}(t)\left(z\hat{\mathbf{x}} + x\hat{\mathbf{z}}\right) + G_\mathrm{y}(t)\left(z\hat{\mathbf{y}} + y\hat{\mathbf{z}}\right) + G_\mathrm{z}(t)\left(-\frac{x}{2}\hat{\mathbf{x}} - \frac{y}{2}\hat{\mathbf{y}} + z\hat{\mathbf{z}}\right)$$

$$= B_0\hat{\mathbf{z}} + G_\mathrm{x}(t)\vec{\mathbf{g}}_\mathrm{x} + G_\mathrm{y}(t)\vec{\mathbf{g}}_\mathrm{y} + G_\mathrm{z}(t)\vec{\mathbf{g}}_\mathrm{z} \tag{5.2}$$

where $G_\mathrm{x}(t)$, $G_\mathrm{y}(t)$ and $G_\mathrm{z}(t)$ are the time-varying gradient waveforms applied by the x-, y- and z-gradient coils respectively and B_0 is the strength of the static magnetic field. x, y and z are values representing position within a Cartesian coordinate system and $\hat{\mathbf{x}}$, $\hat{\mathbf{y}}$ and $\hat{\mathbf{z}}$ are unit vectors defining the axes of the coordinate system. To simplify the expression for $\vec{\mathbf{B}}(t)$, it has been written in terms of the vectors $\vec{\mathbf{g}}_\mathrm{x}$, $\vec{\mathbf{g}}_\mathrm{y}$ and $\vec{\mathbf{g}}_\mathrm{z}$ which represent the position dependent scaling and direction of the fields due to the three different gradient coils.

The conductive path created by the EEG leads and the subject's scalp can be modelled as a simple wire loop enclosing a surface with area, $\vec{\mathbf{S}}$. Therefore, from Faraday's law, the voltage (V) induced in this conductive loop can be expressed as:

$$V = -\frac{\mathrm{d}}{\mathrm{d}t} \int \vec{\mathbf{B}}(t) \cdot \mathrm{d}\vec{\mathbf{S}} \tag{5.3}$$

where $\mathrm{d}\vec{\mathbf{S}}$ has magnitude $\mathrm{d}S$ and is normal to the differential area in the direction of positive flux. Using Equation 5.2, Equation 5.3 can be rewritten as:

$$V = -B_0 \int \hat{\mathbf{z}} \cdot \frac{\mathrm{d}}{\mathrm{d}t}\left(\mathrm{d}\vec{\mathbf{S}}\right) - \sum_{\mathrm{ind=x,y,z}} \frac{\mathrm{d}}{\mathrm{d}t}\left(G_{\mathrm{ind}}(t) \int \vec{\mathbf{g}}_{\mathrm{ind}} \cdot \mathrm{d}\vec{\mathbf{S}}\right) \tag{5.4}$$

$$= -\underbrace{\sum_{\mathrm{ind=x,y,z}} \dot{G}_{\mathrm{ind}}(t) \int \vec{\mathbf{g}}_{\mathrm{ind}} \cdot \mathrm{d}\vec{\mathbf{S}}}_{\text{Gradient Artefact}} - \underbrace{\int \left(B_0\hat{\mathbf{z}} + \sum_{\mathrm{ind=x,y,z}} G_{\mathrm{ind}}(t)\vec{\mathbf{g}}_{\mathrm{ind}}\right) \cdot \frac{\mathrm{d}}{\mathrm{d}t}\left(\mathrm{d}\vec{\mathbf{S}}\right)}_{\text{Movement Artefact}} \tag{5.5}$$

where $\dot{G}_{\mathrm{ind}}(t)$ represents the time-derivative of the applied gradients and $\frac{\mathrm{d}}{\mathrm{d}t}\left(\mathrm{d}\vec{\mathbf{S}}\right)$ represents the movement of the effective wire loop. Since the first terms in Equation 5.5 are dependent upon the time-varying gradients these voltages represent the induced GA, on the other hand the latter terms in Equation 5.5 are dependent upon the motion within the magnetic fields and therefore represent the movement artefacts[1]. As the movement artefact is notoriously difficult to correct (see Chapter 4) we are only interested in correcting the GA during periods where the subject is stationary. Therefore, the latter terms in Equation 5.5 will be ignored here. By changing the basis from the x-, y- and z-axes to the directions along which the read (r), phase (p) and slice (s) gradients of an MRI pulse sequence are applied and by including an additional term to represent the artefact due RF pulses[2] (γ), the GA terms in Equation 5.5 can be written as the linear expression given in Equation 5.1.

---

[1] It is important to note that $B_0\hat{\mathbf{z}} >> G_{\mathrm{ind}}(t)\vec{\mathbf{g}}_{\mathrm{ind}}$ and therefore it is thought that the movement artefact is predominately a result of motion within the B_0-field.

[2] Although it has not been explored theoretically, preliminary experiments suggested that the GA component due to an RF pulse contributes linearly to the overall GA.

5.2.1 Effect of Movement on GA

In this section the effect that different types of movement have on the GA waveform and subsequently on the performance of AAS are discussed.

Following on from the discussion in Chapter 4, movement of the EEG cap and leads in the MR scanner can affect the waveform of the induced GA. There are a number of different types of movement that can affect the shape of the GA. Considered here are the effects of both abrupt changes in the head and lead positions (termed abrupt movements) and small, random, zero-mean, changes in the head position (termed micro-movements). Abrupt movements have a significant effect on the AAS template and can result in large, residual GA being left behind after correction. Whereas micro-movements have no effect on the AAS template, but instead, due to amplitude modulation, broaden the spectral components of the recorded EEG. This broadening causes AAS to leave behind sidebands after correction which are particularly prominent and therefore obscure the neuronal activity above approximately $80\,\mathrm{Hz}$.

Abrupt Movements

Abrupt movements can profoundly affect the AAS template. Suppose during acquisition of volume N_1 the subject makes a small change in position. This changes each element in the parameter $\vec{\alpha}$ in Equation 5.1 causing a change in the relative contribution of each artefact waveform to the overall GA. Hence the shape of the GA changes over time.

$$
x[n] = \begin{cases} s_1[n] + \varepsilon[n] & \text{if } n < mN_1 + n_1 \\ s_2[n] + \varepsilon[n] & \text{if } n \geq mN_1 + n_1 \end{cases} \tag{5.6}
$$

where $x[n]$ is the recorded EEG signal, $\varepsilon[n]$ is a stochastic variable representing the EEG signal and other sources of signal variation and $s_1[n]$ and $s_2[n]$ are the GAs before and after a position change at sample n_1 within volume N_1. In the frequency

domain, we can expect $x[n]$ to contain a linear combination of GA frequency components centred at the harmonics of the reciprocal of the slice/volume TR and any extra components due to the neuronal data and other artefacts.

To see what effect this has on the average artefact ($y[n]$), Equation 4.3 (Chapter 4) can be adapted as follows (for simplicity, X_ε and n_1 are set to zero):

$$y[n] = \frac{1}{N} \left[\sum_{k=0}^{N_1-1} s_1[n] + \sum_{k=N_1}^{N-1} s_2[n] \right] \tag{5.7}$$

Modelling work [94] and subsequent experiments have shown that for small position changes the relative weightings scale linearly. Using this we can define the change in $\vec{\alpha}$ before and after N_1 as:

$$\Delta\vec{\alpha} = \vec{\alpha}_2 - \vec{\alpha}_1 = J_{\vec{\alpha}}(\vec{r}) \cdot \vec{r} \tag{5.8}$$

where $J_{\vec{\alpha}}(\vec{r})$ is the Jacobian matrix of α

$$\mathbf{J}_{\vec{\alpha}}(\vec{r}) = \begin{bmatrix} \dfrac{\partial\alpha_m}{\partial x} & \dfrac{\partial\alpha_m}{\partial y} & \dfrac{\partial\alpha_m}{\partial z} & \dfrac{\partial\alpha_m}{\partial\theta} & \dfrac{\partial\alpha_m}{\partial\phi} & \dfrac{\partial\alpha_m}{\partial\varphi} \\ \dfrac{\partial\alpha_p}{\partial x} & \dfrac{\partial\alpha_p}{\partial y} & \dfrac{\partial\alpha_p}{\partial z} & \dfrac{\partial\alpha_p}{\partial\theta} & \dfrac{\partial\alpha_p}{\partial\phi} & \dfrac{\partial\alpha_p}{\partial\varphi} \\ \dfrac{\partial\alpha_s}{\partial x} & \dfrac{\partial\alpha_s}{\partial y} & \dfrac{\partial\alpha_s}{\partial z} & \dfrac{\partial\alpha_s}{\partial\theta} & \dfrac{\partial\alpha_s}{\partial\phi} & \dfrac{\partial\alpha_s}{\partial\varphi} \\ \dfrac{\partial\alpha_\gamma}{\partial x} & \dfrac{\partial\alpha_\gamma}{\partial y} & \dfrac{\partial\alpha_\gamma}{\partial z} & \dfrac{\partial\alpha_\gamma}{\partial\theta} & \dfrac{\partial\alpha_\gamma}{\partial\phi} & \dfrac{\partial\alpha_\gamma}{\partial\varphi} \end{bmatrix} \tag{5.9}$$

and $\vec{r}$ is a six component vector describing the rigid body translations and rotations of the subject's head relative to the initial position.

$$\vec{r} = \begin{bmatrix} x & y & z & \theta & \phi & \varphi \end{bmatrix}^{\mathrm{T}} \tag{5.10}$$

Substituting for $\vec{\alpha}_1$ in Equation 5.7:

$$y[n] = \frac{1}{N} \left[\sum_{k=0}^{N_1-1} \vec{G}[n]\left(\vec{\alpha}_2 - J_{\vec{\alpha}}(\vec{r}) \cdot \vec{r}\right) + \sum_{k=N_1}^{N-1} \vec{G}[n]\vec{\alpha}_2 \right]$$

83

and rearranging so that the AAS template is written in terms of the GA after the small position change, $s_2[n]$:

$$y[n] = \vec{G}[n] \left[\vec{\alpha}_2 - \frac{N_1}{N} J_{\vec{\alpha}}(\vec{r}) \cdot \vec{r} \right]$$
$$= s_2[n] - \frac{N_1}{N} \Delta s[n] \qquad (5.11)$$

By substituting $s_2[n] = s_1[n] + \Delta s[n]$ the expression can also be written in terms of $s_1[n]$.

$$y[n] = s_1[n] + \left(1 - \frac{N_1}{N} \right) \Delta s[n] \qquad (5.12)$$

Therefore, the template is now a combination of the GA waveforms dependent upon the size of the movement and the temporal incidence and does not solely reflect the GA before or after the position change. As a result, AAS will leave residual artefacts that are proportional to $\Delta s[n]$ both before and after the abrupt movement. While this exercise does not explore more than a single position change, or slow movements, the effect of such movements on the performance of AAS should be similar.

Micro-Movements

To reduce the effects of motion, subjects are always requested to keep still throughout the duration of the experiment. However, even in the most cooperative subjects, tiny, involuntary micro-movements are still observed [130]. These, micro-movements cause tiny random variations in the amplitude of the gradient artefact components. Conceptually this can be likened to a random amplitude modulation which will broaden the spectral components of the GA. To understand the effect that small random micro-movements of the subject's head have on the recorded GA for a single gradient ($G_r[n]$) the following model can be used:

$$x[n] = (a + \mathbf{A}[n])G_r[n] \tag{5.13}$$

where $x[n]$ is the recorded EEG signal for a single channel (see Equation 4.2) and $\mathbf{A}[n]$ is a zero mean, random process. For simplicity, the stochastic variable $\varepsilon[n]$ has been neglected from the model. In order to determine the frequency domain effects the autocorrelation function, $R_x[k]$, was calculated [131]:

$$R_x[k] = a^2 R_G[k] + R_A[k]R_G[k] \tag{5.14}$$

Since $G_r[n]$ is real and periodic, $R_G[k]$ is real, periodic and even [131] and can therefore be represented as a combination of cosines with fundamental frequency, $\omega_f = \frac{1}{\text{slice TR}}$.

$$R_G[k] = \sum_m G_{r,m} \cos(m\omega_f k) \tag{5.15}$$

It is reasonable to assume that the process $\mathbf{A}[n]$ would be wide-sense-stationary and would linearly depend upon the previous value. Therefore, the simplest model is perhaps a first order autoregressive process [132].

$$\mathbf{A}[n] = \sum_{m=0}^{\infty} \rho^m \mathbf{U}[n - k] \tag{5.16}$$

where $\mathbf{U}[n]$ is white Gaussian noise with variance σ_U^2, $\rho < 1$ and the autocorrelation is then,

$$R_A[k] = \frac{\sigma_U^2}{1 - \rho^2}e^{|k| \ln \rho} \tag{5.17}$$

Taking the Fourier transform of the autocorrelation $R_x[k]$ yields the power spectrum of $x[n]$ [131]. It is straightforward to see that the Fourier transform of Equation 5.15 is a sum of delta functions centred at harmonics of ω_f. The product of the autocorrelation functions (Equations 5.15 and 5.17) is a summation

of damped cosine functions. This implies that the spectrum is a summation of Lorentzians also centred at frequencies which are multiples of ω_f:

$$P_{As}(\omega) = \frac{2\pi\sigma_U^2}{1 - \rho^2} \sum_m s_m \left[\frac{\ln\rho}{(\ln\rho)^2 + (\omega - m\omega_f)^2} + \frac{\ln\rho}{(\ln\rho)^2 + (\omega + m\omega_f)^2} \right] \quad (5.18)$$

This implies that the effect of $\mathbf{A}[n]$ is to broaden each harmonic of $s[n]$. It is important to note that the amplitudes of these Lorentzians are dependent upon the magnitude of the frequency component around which they are centred. Since AAS acts like a set of notch filters centred on the harmonic frequencies (see Figure 4.4 in Chapter 4), the residual spectrum shows that the central peak is attenuated but, due to this spectral broadening, components either side of the harmonic remain.

Consequently AAS alone is not effective at removing the GA from an EEG-fMRI experiment which is corrupted by changes in the subject's position.

5.2.2 The GMF method

The Gradient Model Fit (GMF) method works by modelling each of the underlying GA components and regressing them out of the EEG recordings. The components of the GA are temporally isolated by selectively enabling/disabling the read, phase, slice gradients and RF channels during a standard EPI sequence (see Figure 5.1). For effective GA removal it is important that the sampled points of the template and the GA corrupted data match [116]. But the mismatch in the MR clock frequencies (10 MHz) and the EEG sample rate (5 kHz) can lead to shifts in the sampling of the artefact waveforms which are fractions of the EEG sample spacing between separate recordings. Two methods for forming the models for GA correction, which ensure that the models and the experimental data are time-locked, are proposed here.
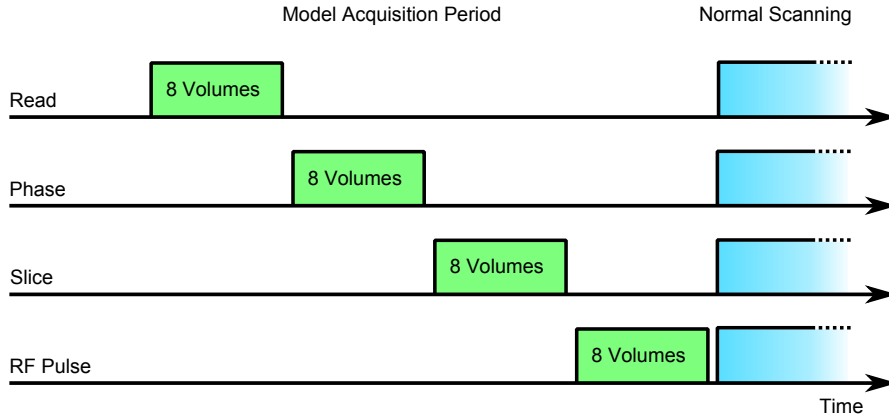
Figure 5.1: A diagram of the custom pulse sequence used to acquire the data for forming the models for the GMF method. Channels of the MRI sequence are nulled in turn to effectively isolate the induced artefact components on the EEG recordings prior to a standard EEG-fMRI experiment.

Single Recording Models (GMF)

This first method involves recording the model data prior to the experiment but during the same acquisition (as shown in Figure 5.1). The slices are then averaged together across time for each component to generate the set of models. Provided the clocks from both the EEG and MRI scanner are synchronised the sampling positions of the model data and experimental data should then perfectly match, allowing the models to be fitted and subtracted from experimental data with relative ease. However, this approach involves recording the models in every experiment, thus increasing the total scan time. Also, this approach is heavily reliant on robust synchronisation. Any brief lapse in synchronisation during the experimental acquisition would render that data set uncorrectable with this method.

High Temporal Resolution (HTR) Models (HTRGMF)

The second method involves increasing the effective sample rate of the GA models by interleaving measurements. Koshkinen and Vartiainen [133] proposed a very similar method to what is proposed here for increasing the sampling rate of the AAS template for systems without the ability to synchronise clocks. However, clock synchronisation is taken advantage of here and instead modifications to the

timings of the MRI pulse sequence are used to slide the sampling positions along the waveform in a controlled manner. This allows us to interleave the data points, which effectively up-samples the data from the 5 kHz sample rate of the EEG system.

To introduce the time shift into the sampling of successive slices of GA, the volume TR (V_{TR}) and the number of slices per volume (N_{SL}) were altered such that the recordings were the same across volume acquisitions, but between slice acquisitions within each volume there is a known time shift. The requirement that artefacts recorded over successive volumes aligned was necessary to allow averaging over volumes to improve the signal-to-noise ratio (SNR) of the model and to attenuate underlying neuronal activity. Therefore, the first condition for choosing the values is that V_{TR} needs to be an integer multiple of the EEG sampling period, 200 µs. The second condition is that the slice TR (S_{TR}) should not be an integer multiple of 200 µs. The third and final condition is that S_{TR} should be an integer multiple of the MR scanner clock period, 0.1 µs. More generally V_{TR} can be expressed as:

$$V_{\mathrm{TR}} = (pN_{\mathrm{SL}} + 1) \times 200\,\mathrm{µs} \tag{5.19}$$

where,

$$p \geq \frac{S_{\mathrm{TR}}}{200\,\mathrm{µs}} \tag{5.20}$$

The resolution of the effective increased sampling rate should be an integer multiple of the period of the MR scanner clock,

$$\frac{200\,\mathrm{µs}}{N_{\mathrm{SL}}} = n \times 0.1\,\mathrm{µs} \tag{5.21}$$

This means that N_{SL} must be an integer factor of 2000. For our experiments we chose $N_{\mathrm{SL}} = 20$ giving a new sampling resolution of 10 µs and we wanted a $V_{\mathrm{TR}} \sim 2\,\mathrm{s}$. Using Equations 5.19 and 5.20, we determined $p = 500$ giving $V_{\mathrm{TR}} = 2000.2\,\mathrm{ms}$. Once the data are recorded the slices are interleaved and then

averaged together across volumes and channels. The oversampling of the GA components allows them to be resampled to match the GA-corrupted EEG data from later recordings with minimal interpolation distortion.

Model Fitting

To fit the obtained models of the components of the GA to the artefact-corrupted data, the following cost function needs to be minimized with respect to $\boldsymbol{\alpha}$.

$$J = \left\| \mathbf{G}\boldsymbol{\alpha} - \mathbf{x} \right\|_2^2 + \beta \left\| \frac{\mathrm{d}}{\mathrm{d}t}(\mathbf{G}\boldsymbol{\alpha} - \mathbf{x}) \right\|_2^2 \tag{5.22}$$

where it is assumed that within each of the EEG slice segments $\boldsymbol{\alpha}$ is time invariant, i.e. there is no subject movement within a slice acquisition. The solution is a simple least squares optimization with a regularization term controlled by the parameter β. This regularization term has the advantage of penalizing large high frequency spikes in the residuals which are likely to be caused by noise sources rather than neuronal activity. This term is needed because the segments of GA-corrupted EEG, $\mathbf{x}$, have a varying baseline, due to the underlying neuronal activity, other sources of artefacts and additive noise, which can lead to a poor fit if not accounted for. Minimizing J and solving for $\boldsymbol{\alpha}$ yields:

$$\boldsymbol{\alpha} = \left(\mathbf{G}^{\mathrm{T}}\mathbf{G} + \beta \dot{\mathbf{G}}^{\mathrm{T}}\dot{\mathbf{G}} \right)^{-1} \left(\mathbf{G}^{\mathrm{T}}\mathbf{x} + \beta \dot{\mathbf{G}}^{\mathrm{T}}\dot{\mathbf{x}} \right) \tag{5.23}$$

where $\mathbf{G}$ and $\mathbf{x}$ are the matrix containing the models and vector containing the EEG segment respectively and $\dot{\mathbf{G}}$ and $\dot{\mathbf{x}}$ are the respective time derivatives. $\mathbf{G}$ also contains a model of constant amplitude in order to compensate for any baseline changes. By setting $\beta = 0$, the solution can easily be written in terms of the Moore-Penrose pseudoinverse, $\mathbf{G}^{\dagger}$. Using Equation 5.23, the models can be regressed out of each slice of GA corrupted data for each EEG channel.

5.3 Methods

EEG recordings were made on a conducting agar phantom and three human volunteers in a Philips Achieva 3T MR scanner (Best, Netherlands) using a 32-channel EEG system (Brain Products GmbH, Gilching, Germany) with an MRplus amplifier, using a sampling rate of 5 kHz and a frequency range of 0.016–250 Hz with a 30 dB roll-off at high frequencies. A standard 32-channel MR compatible EEG cap (EasyCap, Herrsching, Germany) with electrodes positioned according to Figure 3.7 was used. The cap had an additional channel for electrooculography (EOG) which was attached between the left pre-auricular point and nasion on the subjects. To ensure accurate characterisation of the GA waveform the MRI and EEG clocks were synchronised using the Brain Products SyncBox. All of the recordings on humans were made with the approval of the local ethics committee and informed consent.

For all of the following recordings, a customized EPI sequence was employed which allowed the required models to be acquired at the beginning of the data acquisition by nulling three of the four waveforms (read, phase, slice or RF) in turn to isolate the GA components, as shown in the schematic in Figure 5.1. Most of the imaging parameters remained the same for all of the data acquisitions described in this chapter (20 slices, TE = 35 ms, 36×36 matrix, 3 mm isotropic resolution, and SENSE factor of 2). For the acquisition of all of the models subjects were instructed to keep as still as possible. The acquisition of each set of models took approximately 1 min.

1. **HTRGMF Models:** 2 sets of models were recorded for each of the subjects and for the phantom. These recordings consisted solely of the data for forming the models. For these recordings the TR was set to 2000.2 ms with a total of 32 volumes acquired (8 volumes of each of the four waveforms). The choice of TR and number of slices ensured that the EEG sampling of the GA waveform slid within volumes by 10 µs over successive slice acquisitions.

2. **Short Recordings:** A total of 82 volumes of EPI data were acquired in

these recordings with one recording on the phantom and two recordings made on two subjects and four on the other subject. Data were acquired with a TR of 2000 ms. The first 32 volumes were used to acquire the models for the GMF analysis method, with the remaining 50 volumes used to acquire standard EPI data which could be corrected using both the GMF and HTRGMF models. The total duration of data acquisition was therefore approximately 3 min. To test the effectiveness of the new correction methods compared to AAS in the best scenario of no movement of the EEG hardware during data acquisition, two data sets were acquired on the phantom with no movement. Then, to test the efficacy of the different artefact correction methods for recordings containing movements, the position of the phantom and the subjects' heads were abruptly changed at various points during the recording. The phantom was manually moved and the subjects were instructed to change their head position, with new positions held until the next instruction. These movements occurred during volumes 47, 62 and 77 of the data acquisition

3. **Long Recordings:** These recordings used the same parameters as the short recordings with 160 volumes of standard EPI data acquired in these scans resulting in a total scan duration of approximately 6 minutes. A single data set was acquired on the phantom with the phantom moved during volumes 38, 71, 109 and 142. Two data sets were acquired on each subject. To simulate changes in the position of a subject's head during a typical EEG-fMRI study with a longer duration, subjects were instructed to move both feet via plantar/dorsal ankle flexion for 5 s at 25 s intervals after the models had been acquired (total of 10 movement intervals).

5.3.1 Analysis

All data analysis was carried out in Brain Vision Analzyer2 (Version 2.0.3.6367, Brain Products, Gilching, Germany) and MATLAB (Version 2010b, MathWorks, Massachusetts, USA). EEG data and the timing information regarding the onset

of each slice were exported to MATLAB where the models were created and GA correction using these models carried out using in-house software developed for this work. Figure 5.2 outlines the pipeline of the analysis that was used to create the models for the GMF and HTRGMF methods.

GMF

To form the models for subsequent artefact correction from the individual GA waveforms acquired at the beginning of the experimental run, the first 32 volumes of recorded data were segmented using the slice markers to create slice segments (8×20 slices for each of the four models). All 160 slices for each model were then averaged together to form the four models for each individual EEG channel. These were then baseline corrected by subtracting the temporal mean over the entire slice and a weighted average across EEG channels calculated using the peak absolute value (including the sign) of each channel as the weights . This process formed the final single model of the GA from each of the MR components (slice, read, phase and RF) which was used to fit to the rest of the EPI data collected during the same acquisition.

HTRGMF

For forming these models the data were again segmented based on slice markers. The high temporal resolution models were then created by interleaving data from the slice acquisitions. The choice of TR and number of slices ensured that the EEG sampling of the GA waveform slid within volumes by $10\,\mu\text{s}$ over successive slice acquisitions within each volume. The 20 slices acquired within the volume were then interleaved to form a model with an effective sampling rate of $20 \times 5000\,\text{Hz}$. Any components not periodic with the slice frequency were aliased by the interleaving to high frequency noise. These high resolution models were then averaged over the 8 volumes which were acquired for each of the MR components and baseline corrected using the temporal mean to form HTR models for each EEG channel. A weighted average over channels was then calculated using the
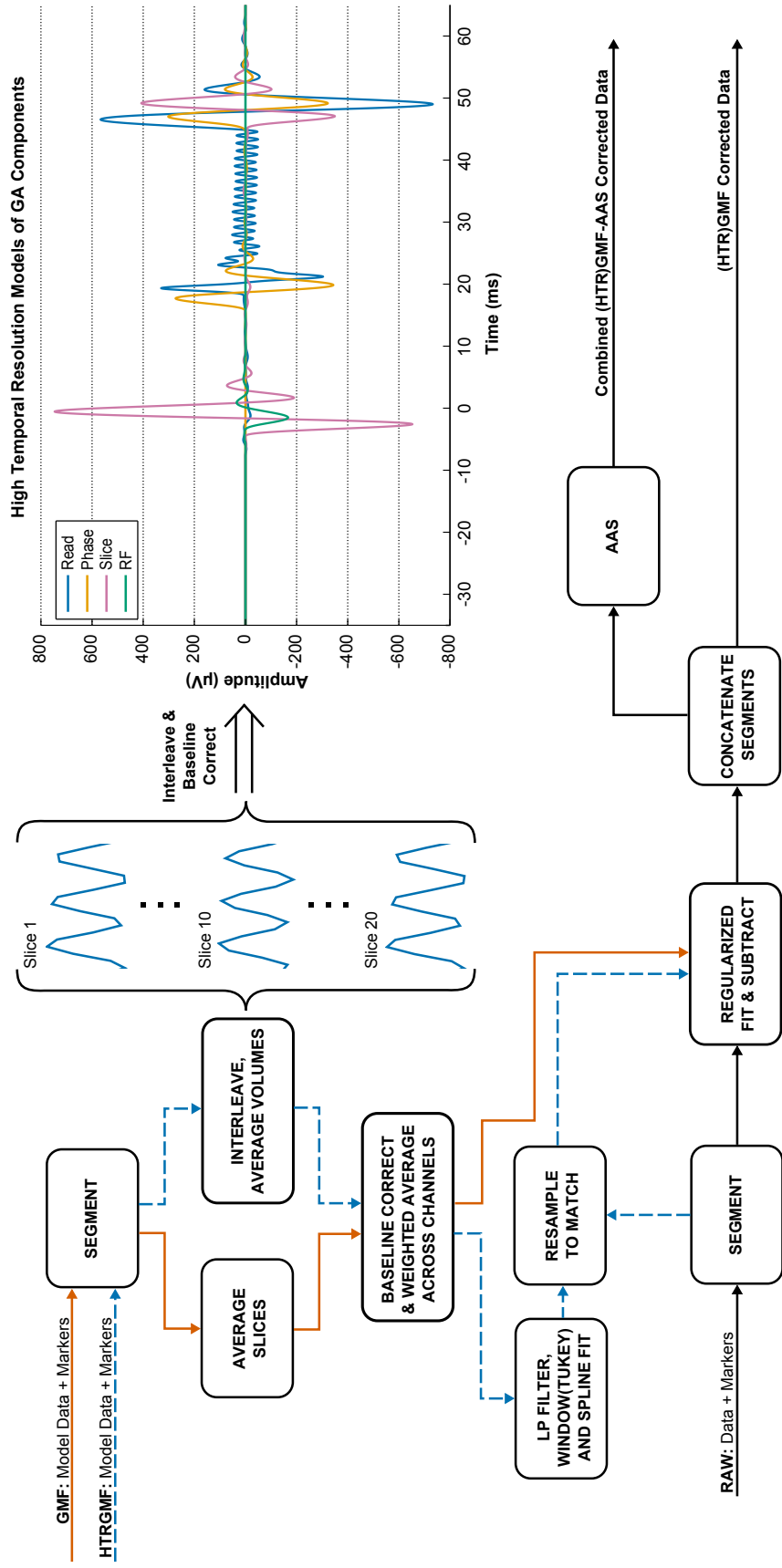
92

Figure 5.2: Schematic showing the pipeline of analysis for both the GMF and HTRGMF and AAS applied after either of these methods. Insert shows the HTRGMF models formed from one dataset collected on the phantom.

same methods described for the GMF models, resulting in a single HTR model for each GA component. The models were low-pass filtered at 1.5 kHz to remove the high frequency noise generated during the interleaving process and windowed using Tukey windows to remove any mismatch between the baseline at the start and end of the models. Using cubic splines the models were iteratively resampled to match the timings of the artefacts in individual data sets.

Model Fitting

The target data to be corrected were segmented according to the slice markers outputted from the MRI scanner. Data were segmented such that adjacent segments of slice data overlapped by 10 samples. The recorded models of the components of the GA (from GMF or HTRGMF) along with an additional model of constant amplitude to model baseline offsets were then fitted to the GA in each EEG channel and slice of the EPI data. This was done using the regularised least squares fit described in Equation 5.23 with the regularisation parameter, β, set to 100. The scaled models were then subtracted from the relevant segment of GA corrupted EEG data with the process repeated for all GA occurrences in the data-set. Individual slice data were then concatenated together by determining the weighted-averaged difference between the segments for the overlap period. The weightings were such that the samples closest to the join were favoured in the averaging.

AAS

For comparison of the new GMF correction methods with existing GA correction methods, each data set was also corrected using AAS in BrainVision Analyzer2. The artefact template used for correction spanned one TR period and was formed by averaging over the entire acquisition (50 and 160 volumes for the short and long data-sets respectively). Use of this long averaging period ensured maximum sensitivity to changes in the GA due to motion. In addition because of the relatively short length of the data acquisitions used in this study the number of

volumes which were averaged over were similar to those used for longer data sets where sliding window templates are often employed (typically using 60 volumes) which is required to ensure that neuronal signals of interest are not removed from the data [115]. The AAS template was then subtracted from each occurrence of the GA. To assess whether further improvement may be attained AAS was also applied to the data after correction using the (HTR)GMF methods. Data were not down-sampled or subjected to further low-pass filtering after any of the correction methods so as to allow residual GA signals to be assessed across the entire frequency band. Both the uncorrected and corrected EEG data, using each of the methods described, were exported to Matlab for assessment of the relative performance of the correction methods.

Comparison of Methods

The EEG signals pre- and post-correction using the different methods were Fourier transformed using a fast Fourier transform. GAs occurred at each slice harmonic where the fundamental slice frequency was 10 Hz (number of slices/TR = 20/2). As predicted from the theoretical model (see Equation 5.18) broadening of high frequency components of the GA was observed (Figure 5.3, blue line) due to the movements that occurred during data acquisition. Therefore the integral of the signal, using the trapezium rule, in the Fourier domain in a window of ± 0.2 Hz around each slice harmonic was found. The average of signal over channels for each of the harmonics was then calculated for each data set and correction method as well as the raw data. The ratio of the EEG spectrum of data recorded after correction (using each of the correction methods) to before correction was then calculated. An average and standard deviation over all repeats of the same data acquisition (phantom or subject) was then taken for each correction method and the average ratios converted to attenuation ($20 \log_{10}$[corrected/uncorrected]). To evaluate significant differences in the performance of correction methods, paired Wilcoxon signed rank tests between the attenuation calculated when using AAS only and the attenuation when using each of the other correction methods were
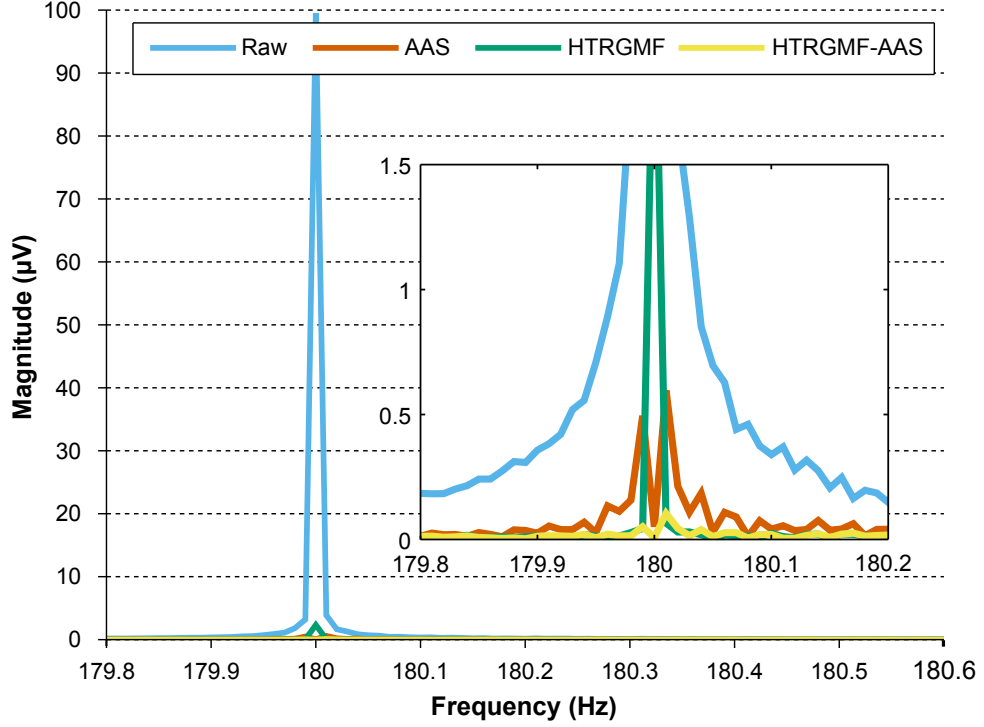
Figure 5.3: 18th harmonic component $(180\,\text{Hz})$ from a short data set for a representative subject and channel (electrode P3). The frequency profile of the raw data and data after each of the correction methods is shown.

carried out at each harmonic, with the tests including each subject dataset in the long or short recordings.

MRI data were corrected in SPM8 in order to extract movement parameters $(x, y, z, \theta, \phi, \psi)$. Positional shifts and Euler rotation were calculated using the following equations:

$$\text{Positional Shift} = \sqrt{x^2 + y^2 + z^2} \tag{5.24}$$

$$\text{Euler rotation} = \arccos\left(\frac{\text{trace}\{\mathbf{R}_\theta \mathbf{R}_\phi \mathbf{R}_\psi\} - 1}{2}\right) \tag{5.25}$$

where $\mathbf{R}_\theta$, $\mathbf{R}_\phi$, $\mathbf{R}_\psi$ are the rotation matrices for the rotation parameters.

96

5.4 Results

Two short data sets from one of the subjects were excluded from the analysis. This was because the instructed movements were too abrupt. This induced large, impulse-like movement artefacts whose transient responses to the low-pass EEG filters created additional, long-lasting, confounding artefacts. In the short recordings on the subjects the overall movements did not exceed 10 mm translation and 12° rotation; whereas for the long recordings on the subjects, overall movements did not exceed 2 mm translation and 1° rotation. For the recordings made on the phantom the overall movements were less than 12 mm translation and 4° rotation in all recordings.

Both GMF and HTRGMF models were successfully formed from the eight volumes of GA data acquired for each MR component (slice, read, phase and RF) on both the phantom and subjects. Example models derived from data collected on the phantom for the HTRGMF methods are shown in the insert of Figure 5.2. The assumption made that the GA produced by a MR pulse sequence is a linear superposition of the GA generated by the different components contained in the sequence can be seen to be correct from Figure 5.4; where the models are fitted to GA-corrupted EEG both before and after a movement. Overall both the GMF methods corrected the GA well with the fitting of the models tracking the variation in the GA caused by changes in position successfully (Figure 5.4, green and orange lines), whereas, the standard AAS correction left behind large, high-frequency components after correction when motion occurred during the data recording (blue lines in Figure 5.4). However, some residual artefact still remained after correction using either GMF method. These residuals were particularly noticeable during the read-out period of the MR pulse sequence. In addition the GMF methods added some low-frequency oscillations to the waveforms which appeared after the crusher gradients had played out. However, these remaining artefacts were greatly attenuated by applying AAS after GMF correction as shown in Figure 5.5, yellow line.

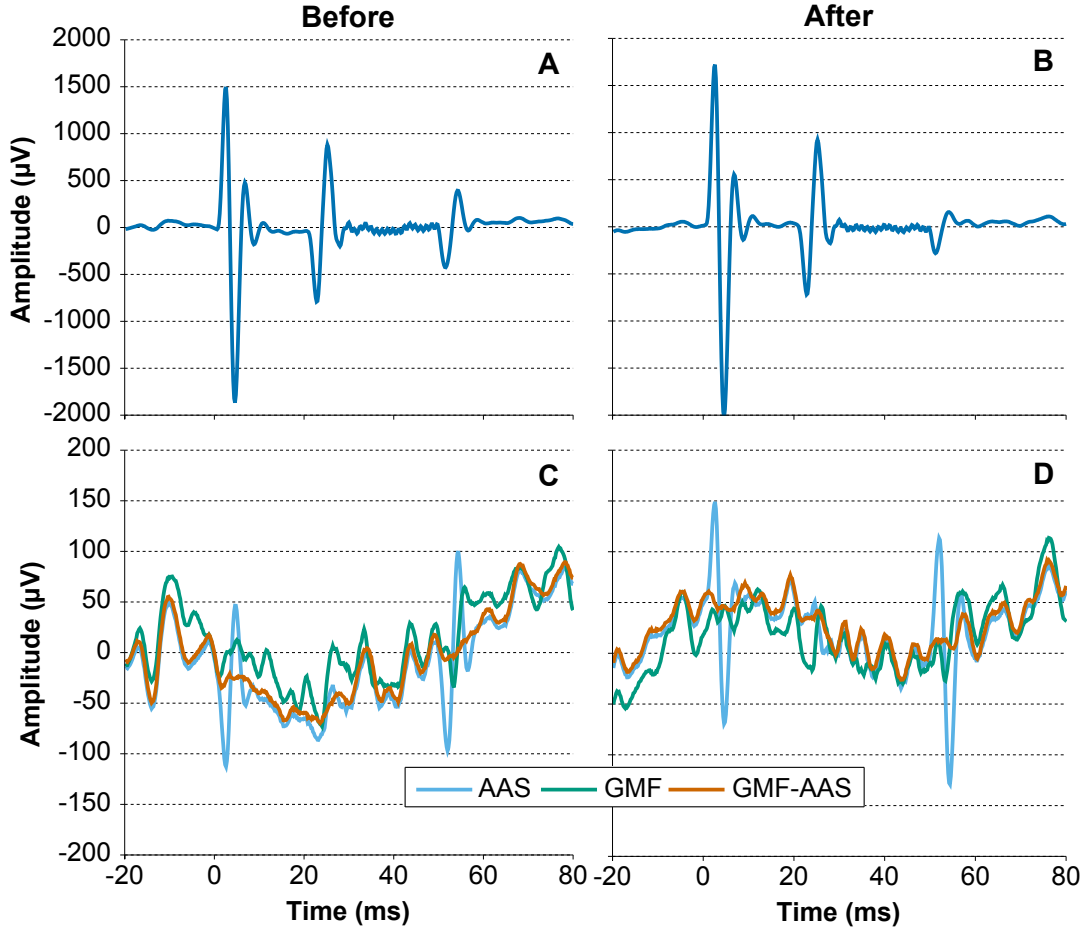Figure 5.6 compares the fit parameters for each of the GA models for consecutive

Figure 5.4: Slice GA from channel POz before (**A**) and after (**B**) a subject movement and the residual GA for these slices after artefact correction using AAS, GMF and combined AAS-GMF. The GMF fit parameters before/after the subject movement are: $a = 0.3025/0.2416$, $b = 1.3850/1.3454$, $c = -2.1558/-2.3966$ and $d = -0.5502/-0.4756$ (refer to Equation 5.1).
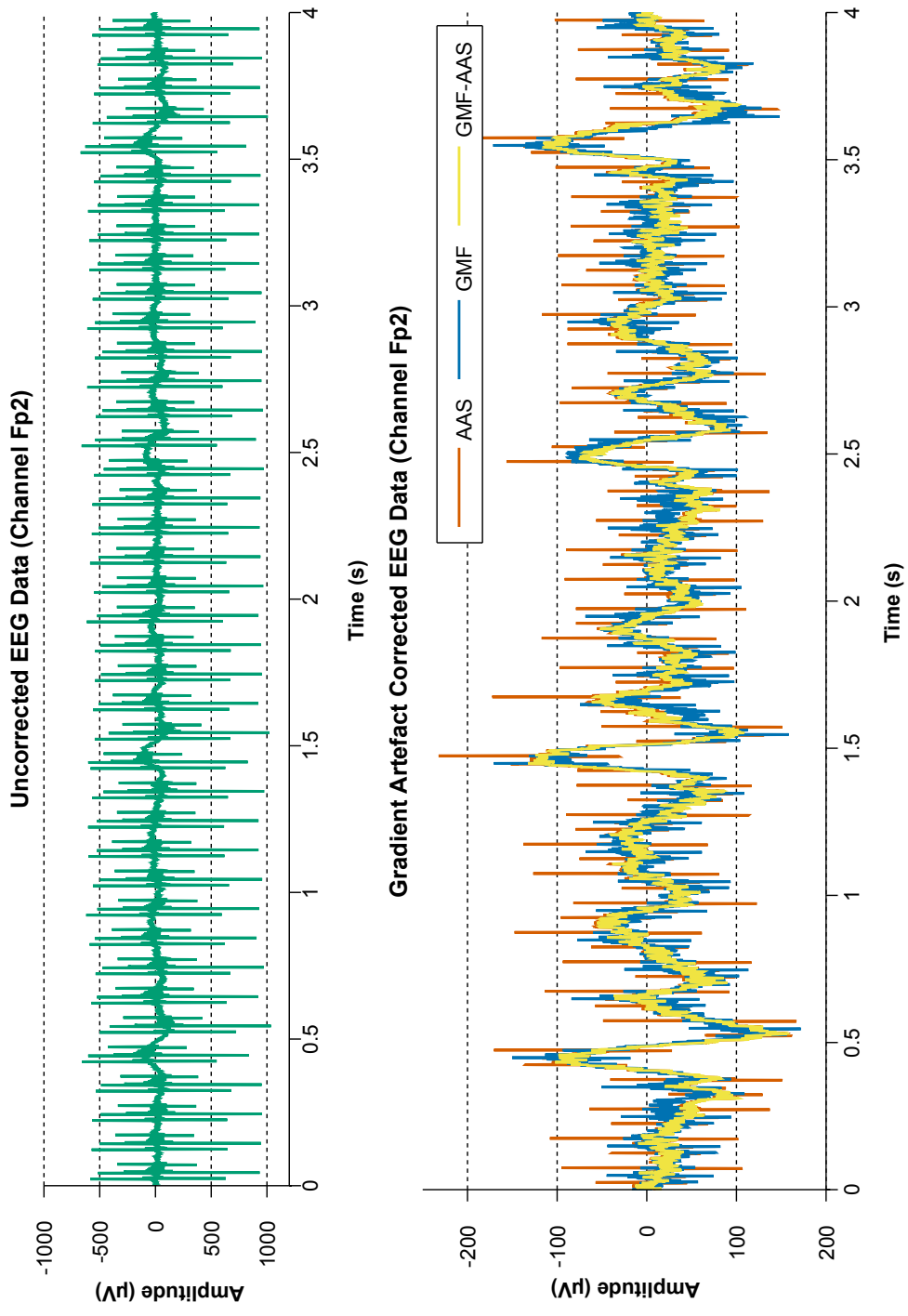
Figure 5.5: A 4 s segment of EEG data corrected in three different ways. The data set was drawn from a short recording collected from a representative subject who was asked to move at various points during the recording. The segment was selected from a quiet period between movements. The pulse artefact can clearly be seen within the chosen period.
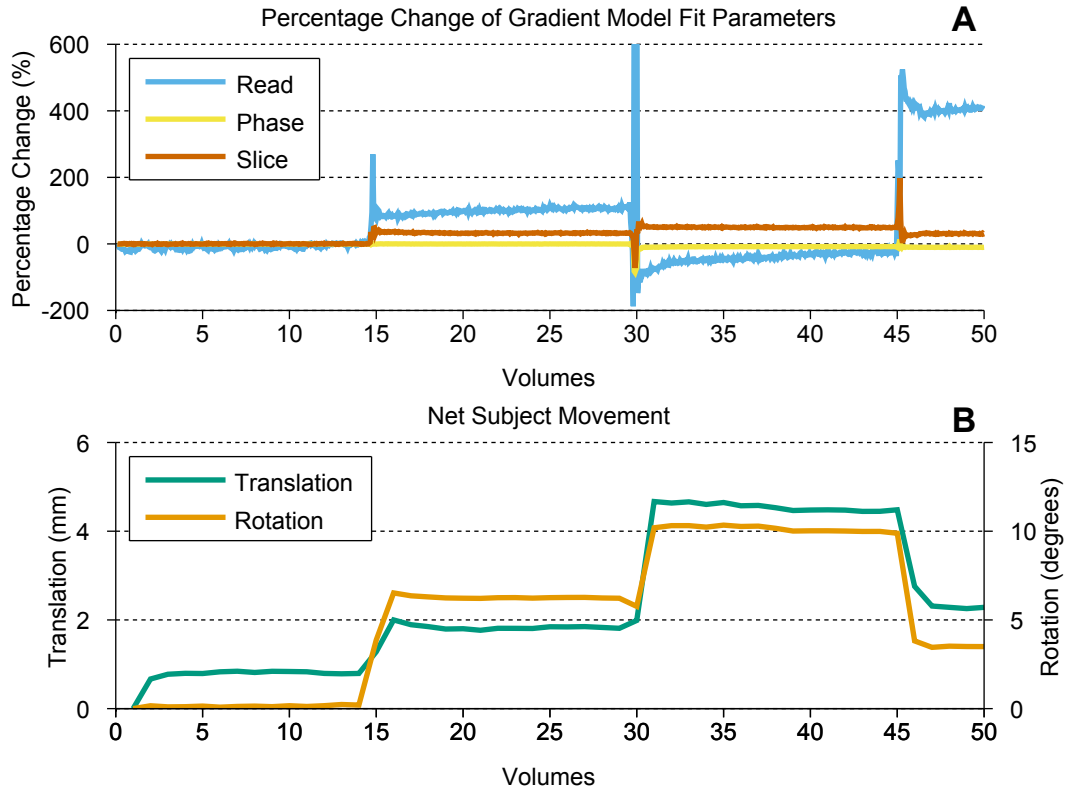
Figure 5.6: Comparison of the change in the model fit parameters for the GMF method applied to a short data set. Fit parameters are shown for data recorded at electrode Fp1 (**A**) with the net translation (see Equation 5.24) and rotation (Equation 5.25) of the head (**B**) computed from the SPM movement parameters. The percentage changes in **A** were calculated relative to the fit parameters estimated for the first slice of GA data ($a = -0.0492$, $b = 1.1309$ and $c = -0.2007$). For simplicity the RF model was not included in this figure.

slice acquisitions to the magnitude of the contemporaneous movements and rotations, for a short data-set recorded on a representative subject. Figure 5.6 clearly illustrates a strong correlation between the fit parameters and movements of the subject.

Figure 5.3 shows the frequency profile of the EEG data for the 18th harmonic (180 Hz) both before and after artefact correction using each method. Before correction, the data exhibited large amplitude signals at harmonics of the fundamental slice frequency (10 Hz) with noticeable broadening of these frequency responses. The broadening was found to be greater for higher frequency harmon-

ics ($>80\,$Hz) where the central peak was larger. The residuals due to AAS showed that the central peak had been attenuated, but that a significant component of artefact was left behind in the side-bands. Whereas for the (HTR)GMF methods of artefact correction residuals often left a central attenuated peak with little or no broadening of the artefact signal remaining. Therefore the combination of (HTR)GMF with AAS yielded the best results, where the greatest attenuation of all harmonic information was achieved as reflected in Figures 5.7–5.10.

Both GMF and HTRGMF methods produced better artefact attenuation than AAS when applied to the phantom data, with GMF outperforming HTRGMF (Figures 5.7 and 5.8). Further attenuation was achieved with combined GMF-AAS and HTRGMF-AAS where no significant difference was observed between either combined method. For the subject data (HTR)GMF did not perform as well as AAS, but combined (HTR)GMF-AAS yielded significant improvements over AAS as shown in Figures 5.9 and 5.10.

For the stationary recordings, the performance of (HTR)GMF compared to AAS was poor, but the performance of (HTR)GMF-AAS was comparable if not slightly better than AAS.
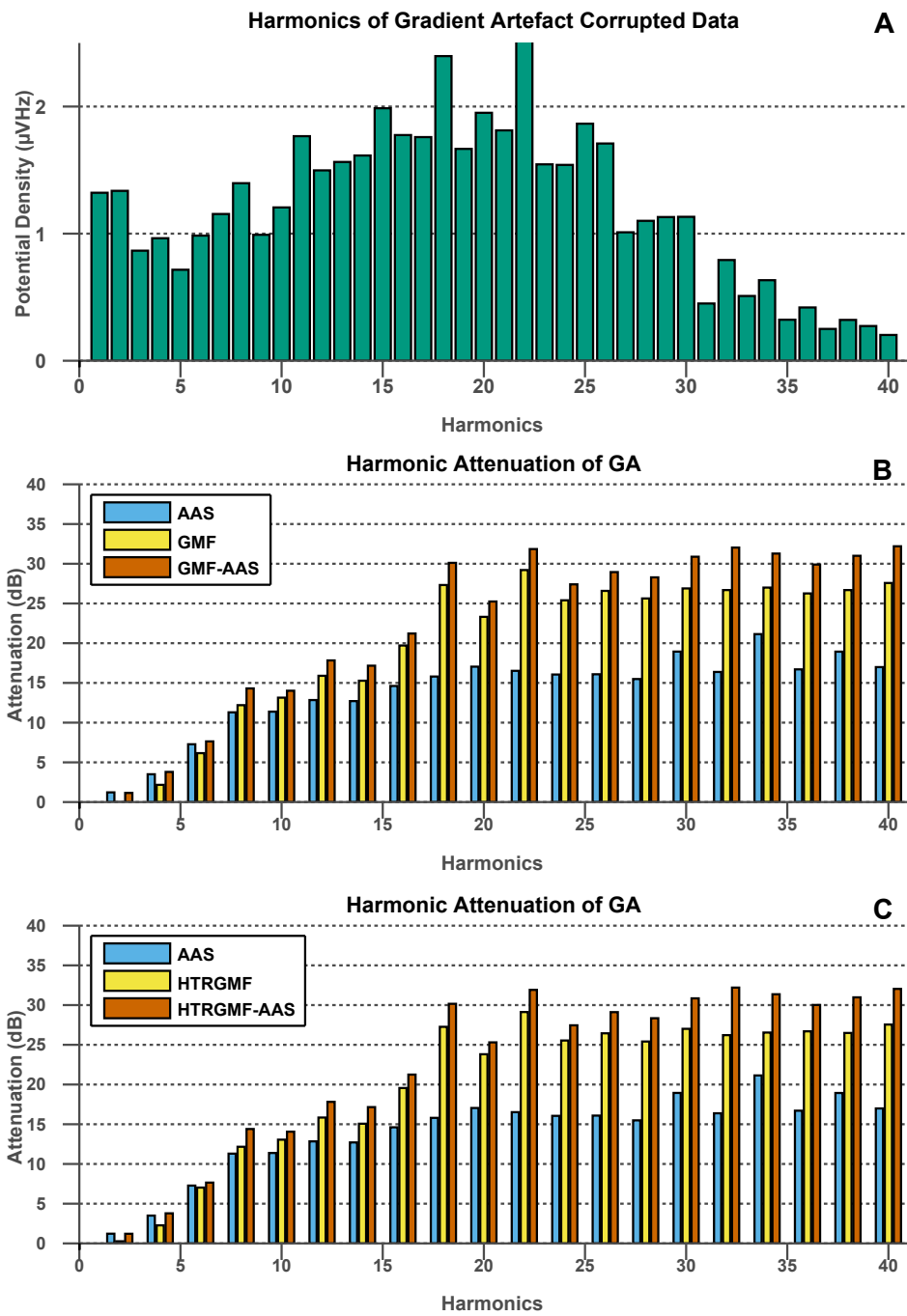
Figure 5.7: Plots of raw harmonic density (A) and attenuation values of even harmonics for AAS and combinations with GMF correction (B) and AAS and combinations with HTRGMF (C) for the short data set acquired on the phantom.
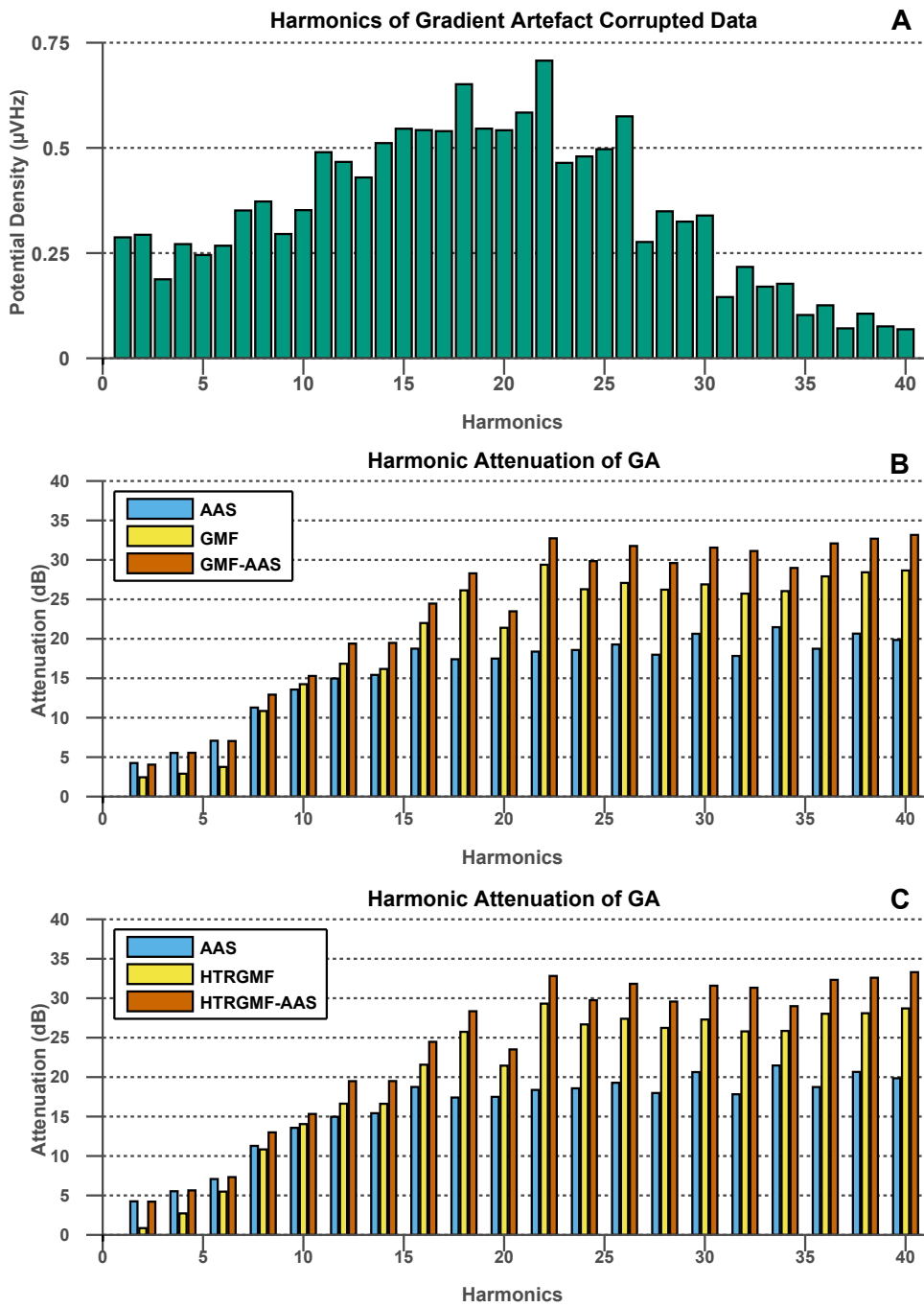
Figure 5.8: Plots of raw harmonic density (A) and attenuation values of even harmonics for AAS and combinations with GMF correction (B) and AAS and combinations with HTRGMF (C) for the long data set acquired on the phantom.
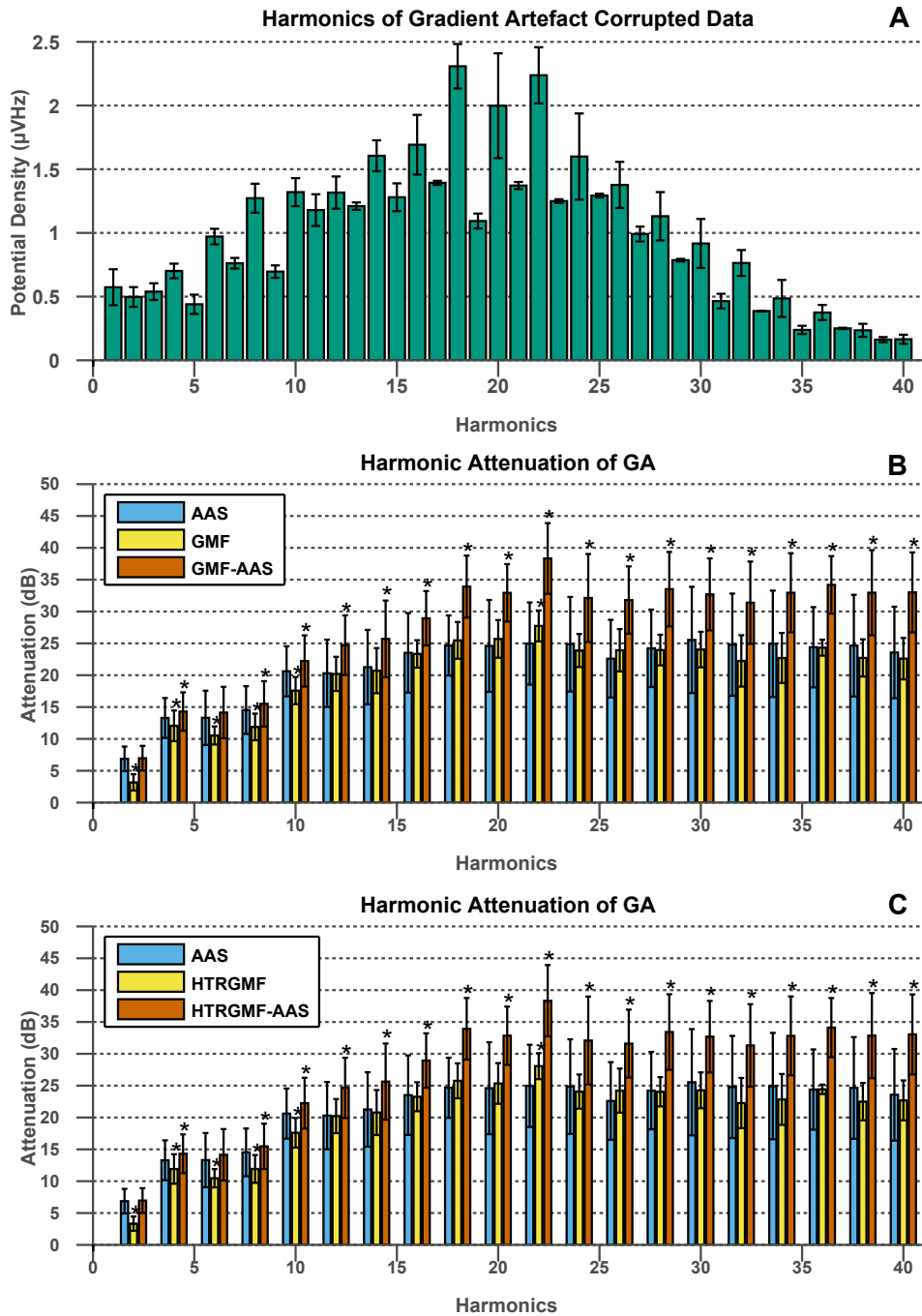
Figure 5.9: Plots of raw harmonic density (A) and attenuation values of even harmonics for AAS and combinations with GMF correction (B) and AAS and combinations with HTRGMF (C) for the short data sets averaged over the subjects, repeats and channels. Errorbars represent the standard deviation across EEG channels. Significance stars denote significant difference (p<0.05) between the method and AAS for that particular harmonic (Wilcoxen signed rank test).
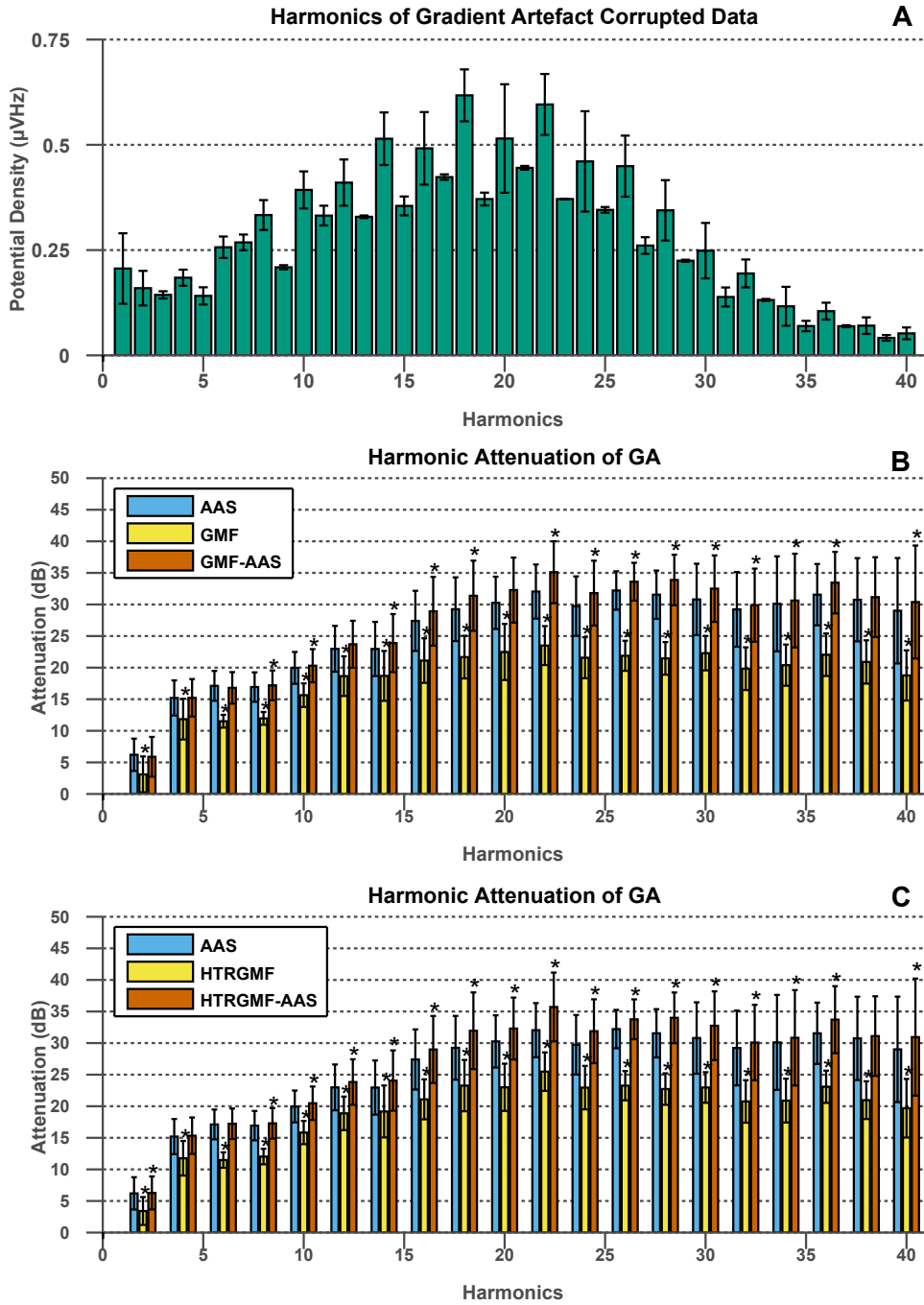
Figure 5.10: Plots of raw harmonic density (A) and attenuation values of even harmonics for AAS and combinations with GMF correction (B) and AAS and combinations with HTRGMF (C) for the long data sets averaged over subjects, repeats and channels. Errorbars represent the standard deviation across EEG channels. Significance stars denote significant difference (p<0.05) between the method and AAS for that particular harmonic (Wilcoxen signed rank test).

5.5 Discussion

In this study, a novel, GA-correction method which is able to attenuate artefacts in recordings made where subjects may move head position was developed and its performance was evaluated for multiple recordings from a phantom and healthy subjects. The results agree with the theory [95, 94] and show that the GA can be characterised well by a linear superposition of underlying GA components due to the read, phase and slice gradients and the RF pulse. Further, the results show a significant improvement in GA correction can be achieved by using either GMF-AAS or HTRGMF-AAS compared with stand-alone AAS for data corrupted by changes in the subject's head position (see Figures 5.7–5.10).

Comparison of the GA before and after a single head movement shows that the form of the GA is very sensitive to any changes in position (Figure 5.4) where for example a net movement of $\sim 2\,\mathrm{mm}$ and $\sim 4°$ caused changes in the relative weightings of the underlying components by as much as $400\,\%$ on a single channel (Figure 5.6). As expected from theory (see Chapter 4 and the theory section of this chapter) and the work of others [118, 119] head movements severely impair the performance of AAS. This variation in shape of the GA prevents AAS from forming a representative template of the GA resulting in large residuals being left behind. However, unlike AAS, GMF and HTRGMF are able to track these changes in the GA demonstrating the theoretical assumption that the GA is predominantly a linear superposition of artefacts due to the separate components of the MRI sequence [95, 94].

The additional oscillations introduced by (HTR)GMF post crusher gradients (see Figure 5.5) may be caused by subtle differences in the scanner vibrations produced when individual gradients are applied during model formation and multiple gradients are applied during normal EPI. These differences in vibration of the phantom/subject could yield differences in the artefacts thus causing components to be introduced by the models during fitting. Fortunately, combined (HTR)GMF-AAS appears to clean up these residual and additional artefacts.

From the theoretical work, it seems reasonable that the broadening of GA harmonics observed in the spectral domain is due to subject movement. The narrowing of the frequency components by (HTR)GMF suggest that the model fitting is able to remove the variability in the GA across multiple slices. AAS is then able to offer further improvement by attenuating the central peak due to the repetitive residuals unaccounted for by (HTR)GMF. This makes the (HTR)GMF technique particularly relevant when investigating the high frequency bands of the EEG (gamma-band), which are typically difficult to access using current GA correction methods.

For the larger positional changes in the short datasets AAS performed worse relative to (HTR)GMF-AAS than for the smaller changes in the long datasets. This is intuitive, as larger position changes result in larger differences in the artefacts used to form the average template. However, similar attenuation values were observed when comparing the performance of (HTR)GMF-AAS for both the short and long datasets.

The data were acquired using the Brain Products Sync Box to synchronize the MR scanner and EEG clocks and the slice TR was selected to be an integer multiple of the sampling period for all datasets except the HTRGMF models. This ensured that the artefact waveforms were sampled at the same times over all slices. It is generally important for any template based correction method (such as AAS) that the sampling of the GA is consistent across the chosen template periods [116]. GMF-AAS is not an exception to this and could be severely affected in cases of unstable or no synchronization. This means that the data for forming the models needs to be acquired during the same acquisition as the experimental data. However, the HTRGMF method allows for separate recordings of the models and the experimental data. Moreover, the HTRGMF method can accommodate for any temporary loss of synchronization during the experimental period and in principle no synchronization at all. All that is required is that the HTRGMF models are resampled after any instance of synchronization error. However, since AAS requires synchronization, HTRGMF-AAS may prove to be problematic, but

further work would be required to evaluate this.

EEG data immediate to instances of subject movement cannot be used. This is primarily due to the dominance of the movement artefact. However, in Figure 5.6 there are large spikes in the percentage change of the fit parameters surrounding instances of subject movement. These are likely due to problems in fitting the components both in the presence of the motion and the movement artefact. The (HTR)GMF method assumes that the GA is stable over the period of a single slice acquisition. This assumption is not necessarily true during subject motion causing difficulties in the fitting of the GA models. Also, the large variations in the EEG signal corresponding to the movement artefact may also affect the performance of the fitting algorithm.

While there are no significant differences in performance of GMF-AAS and HTRGMF-AAS there are differences in the practice of the two methods. GMF-AAS requires models to be recorded at the beginning of every acquisition, increasing the total scan time. On the other hand, HTRGMF-AAS requires a minimum of one extra, short-time scan to collect the model data, but does not require any increase in duration to the acquistions of the experimental data. However, HTRGMF-AAS is more computationally complex to implement and can take a longer time to correct the GA than GMF-AAS.

The major limitation of the (HTR)GMF methods is that a model is required for each component of the imaging sequence. As a result, the components need to be isolated from one another which requires a customised MR pulse sequence which selectively nulls the gradient components sequentially. Therefore, unlike AAS, the data for forming the models cannot be collected at the same time as the experimental data, which obviously increases the total scan time. Moreover, the customised MR pulse sequence may be challenging to implement and requires a significant level of technical expertise.

5.6 Conclusion

In conclusion, the results indicate that the GA can predominantly be represented as a linear superposition of underlying artefact components. By producing models for these components, the variation in the GA due to changes in subject position can be adaptively accounted for and removed. Overall a hybrid approach of (HTR)GMF-AAS seems best. Since there was little difference between GMF-AAS and HTRGMF-AAS the choice of method is left to the experimenter who may want to consider factors such as scan time or synchronization issues. The (HTR)GMF-AAS methods are particularly advantageous to simultaneous EEG-fMRI studies where studying the EEG response in the gamma frequency band are of interest as well as for subject groups, such as children or patients, where significant movement during recordings is likely to occur.

In the next chapter an alternative method for correcting the GA in the presence of subject movement is presented which does not require a customised pulse sequence.

Chapter 6

Difference Model Subtraction (DMS)

6.1 Introduction

Many of the technical challenges associated with simultaneous EEG-fMRI have been introduced in Chapters 4 and 5. In particular, these chapters introduced the gradient artefact (GA). The GA refers to the signals produced on EEG recordings by the imaging sequence applied by the MRI scanner. As previously discussed, although the GA is typically the largest and most disruptive of all the EEG-fMRI artefacts, since the timings of the imaging sequence are well defined, the GA is usually the most straightforward artefact to remove. By far, the most widely used correction method is AAS (see Section 4.6.1 and Allen *et al.* [2]). In order for AAS to be effective a number of conditions need to be satisfied: the first is that the artefact waveform must be strictly periodic; the second is that the fundamental period of the waveform must be a multiple of the EEG sampling period. These conditions ensure that when the GA is digitized by the EEG system, the sample positions of successive periods of the digitized GA align and can therefore be easily averaged to form the template.

Unfortunately, the assumption of periodicity is violated when the subject changes

position during the experiment. As mentioned in Chapters 4 and 5, subject movement changes the shape of the GA waveform such that the template formed in AAS no longer represents accurately the GA which is to be removed (see Section 5.2.1). Changes in subject position consequently result in large residual GA components being left behind in the data after AAS.

On the basis of theory [95, 94] and the experimental work detailed in Chapter 5 we can assume that the GA can be represented by a linear combination of the artefacts produced by the temporal derivatives of the waveforms applied on the three orthogonal gradient channels along with the artefact resulting from application of RF. A further assumption that can be made is that the relative weightings of these components vary linearly with respect to small, changes in position of the head. If this additional assumption is true then it should be possible to produce a basis set of models which can collectively characterise the change in the GA waveform for small variations in subject position. This basis set could then be used, after AAS, to regress out the residuals left behind because of subject movement. This is the basis of the difference model subtraction (DMS) extension to the AAS method presented here.

The overall aim of the work here was therefore to develop a method for removing any residual GA left behind by AAS for EEG-fMRI data corrupted by subject movement, without the need for customized MRI sequences. For the first part of this work, recordings were made on a spherical agar phantom designed to mimic the conductive properties of the human head. Small adjustments to the phantom's position were made between scans to mimic the types of movements which may typically occur during an EEG-fMRI experiment. The changes in magnitude of the different components of the GA resulting from these movements were investigated. The objective of this part of the work was to explore the effects of subject movement on the GA and to show that the amplitude of the GA varies linearly with small changes in subject position. After establishing linearity, this principle was used to construct models that characterise the change in GA for a basis set of typical head movements. These models were then fitted and subtracted

from AAS-corrected data to remove any residual artefact caused by the changes in subject position.

6.2 Theory

In Chapter 5, an expression was derived for the AAS template ($y[n]$ formed by averaging over N volume acquisitions when a position change occurs during acquisition of volume N_1 [Equation 5.11]). This can be rewritten simply as:

$$y[n] = s_2[n] - \frac{N_1}{N}\vec{G}[n]\mathbf{J}_{\vec{\alpha}}(\vec{r}) \cdot (\vec{r}_2 - \vec{r}_1) \tag{6.1}$$

where $s_2[n]$ is the GA measured at the final subject head position, $\vec{G}[n]$ is a matrix containing the components of the GA and $\mathbf{J}_{\vec{\alpha}}(\vec{r})$ is the Jacobian matrix of the parameter vector, $\vec{\alpha}$ (see Equation 5.1). The initial and final head positions and orientations are characterised by $\vec{r}_1$ and $\vec{r}_2$ respectively. It is reasonable to assume that the most likely changes in head position will be due to translation along the bore (i.e. in the z-direction), along with nodding (i.e. a rotation by angle θ around the x-axis [left-right direction]) and shaking (i.e. a rotation by an angle ϕ around the z-axis [inferior-superior direction]) of the head. This is because other types of movement are unnatural motions that are difficult to produce within an MRI head coil [94]. Therefore the residuals after AAS for a segment of GA occurring after volume N_1 can be written as:

$$s_2[n] - y[n] = \frac{N_1}{N} \begin{bmatrix} G_r[n] \\ G_p[n] \\ G_s[n] \\ G_\gamma[n] \end{bmatrix}^{\mathrm{T}} \begin{bmatrix} \frac{\partial \alpha_r}{\partial z} & \frac{\partial \alpha_r}{\partial \theta} & \frac{\partial \alpha_r}{\partial \phi} \\ \frac{\partial \alpha_p}{\partial z} & \frac{\partial \alpha_p}{\partial \theta} & \frac{\partial \alpha_p}{\partial \phi} \\ \frac{\partial \alpha_s}{\partial z} & \frac{\partial \alpha_s}{\partial \theta} & \frac{\partial \alpha_s}{\partial \phi} \\ \frac{\partial \alpha_\gamma}{\partial z} & \frac{\partial \alpha_\gamma}{\partial \theta} & \frac{\partial \alpha_\gamma}{\partial \phi} \end{bmatrix} \cdot \begin{bmatrix} z_2 - z_1 \\ \theta_2 - \theta_1 \\ \phi_2 - \phi_1 \end{bmatrix}$$

$$= \frac{N_1}{N} \begin{bmatrix} G_r[n]\frac{\partial \alpha_r}{\partial z} + G_p[n]\frac{\partial \alpha_p}{\partial z} + G_s[n]\frac{\partial \alpha_s}{\partial z} + G_\gamma[n]\frac{\partial \alpha_\gamma}{\partial z} \\ G_r[n]\frac{\partial \alpha_r}{\partial \theta} + G_p[n]\frac{\partial \alpha_p}{\partial \theta} + G_s[n]\frac{\partial \alpha_s}{\partial \theta} + G_\gamma[n]\frac{\partial \alpha_\gamma}{\partial \theta} \\ G_r[n]\frac{\partial \alpha_r}{\partial \phi} + G_p[n]\frac{\partial \alpha_p}{\partial \phi} + G_s[n]\frac{\partial \alpha_s}{\partial \phi} + G_\gamma[n]\frac{\partial \alpha_\gamma}{\partial \phi} \end{bmatrix}^{\mathrm{T}} \cdot \begin{bmatrix} z_2 - z_1 \\ \theta_2 - \theta_1 \\ \phi_2 - \phi_1 \end{bmatrix}$$

$$= \frac{N_1}{N} \begin{bmatrix} \Delta_z G[n] \\ \Delta_\theta G[n] \\ \Delta_\phi G[n] \end{bmatrix}^{\mathrm{T}} \cdot \begin{bmatrix} z_2 - z_1 \\ \theta_2 - \theta_1 \\ \phi_2 - \phi_1 \end{bmatrix} \tag{6.2}$$

where the indices r, p, s and γ refer to the read, phase, slice and RF channels of the applied pulse sequence respectively[1]. To estimate the elements $\Delta_i G[n]$ recordings of the GA can theoretically be made before and after position changes which solely consist of either translations along the z-axis or rotations around the x- or z-axes. Suppose that two recordings are made at two different positions along the z-axis. The difference between the two may be expressed as:

$$\Delta_z s[n] = s_{zb}[n] - s_{za}[n] = \vec{G}[n]\left(\vec{\alpha}(z_b) - \vec{\alpha}(z_a)\right) \tag{6.3}$$

Taking a first order Taylor polynomial expansion of $\vec{\alpha}(z_b)$ produces:

---

[1]If the axis describing the slice orientation is the same as the MR scanner's axis, then the read, phase and slice gradients are equivalent to gradients applied along the x-, y- and z-axes respectively.

$$\vec{\alpha}(z_b) = \vec{\alpha}(z_a) + \left(\frac{\partial \alpha_r}{\partial z} + \frac{\partial \alpha_p}{\partial z} + \frac{\partial \alpha_s}{\partial z} + \frac{\partial \alpha_\gamma}{\partial z} \right) (z_b - z_a) \tag{6.4}$$

Using this Equation 6.3 can be rewritten as:

$$\Delta_z s[n] = \vec{G}[n] \left(\frac{\partial \alpha_r}{\partial z} + \frac{\partial \alpha_p}{\partial z} + \frac{\partial \alpha_s}{\partial z} + \frac{\partial \alpha_\gamma}{\partial z} \right) (z_b - z_a) \tag{6.5}$$

$$= \Delta_z G[n] \Delta z \tag{6.6}$$

Similar expressions can be obtained for the difference in GA with respect to rotations around the z- and x-axes. Substituting these difference equations into Equation 6.2 yields an approximation for the residual GA.

$$s_2[n] - \hat{s}[n] = \begin{bmatrix} \Delta_z s[n] \\ \Delta_\theta s[n] \\ \Delta_\phi s[n] \end{bmatrix}^{\mathrm{T}} \cdot \begin{bmatrix} \dfrac{N_1}{N} \dfrac{z_2 - z_1}{\Delta z} \\[2ex] \dfrac{N_1}{N} \dfrac{\theta_2 - \theta_1}{\Delta \theta} \\[2ex] \dfrac{N_1}{N} \dfrac{\phi_2 - \phi_1}{\Delta \phi} \end{bmatrix} = \begin{bmatrix} \Delta_z s[n] \\ \Delta_\theta s[n] \\ \Delta_\phi s[n] \end{bmatrix}^{\mathrm{T}} \cdot \vec{\boldsymbol{\beta}} \tag{6.7}$$

where $\vec{\boldsymbol{\beta}}$ is a fitting parameter which can be estimated using the regularized least squares approach from the (HTR)GMF method (see Chapter 5). Also note that fitting for the residuals before the movement will simply produce a different estimate of $\vec{\boldsymbol{\beta}}$.

6.2.1   Spatial Variation

In their paper, Yan *et al.* [94] presented physical models for the spatial variation of the EEG artefact produced by a longitudinal MRI gradient (along the z-axis) and a transverse (along the x-axis) MRI gradient (an expression for a gradient applied along the y-axis was unavailable) for a spherical conductor with leads running along "lines of longitude" to converge at the "north pole" of the phantom with
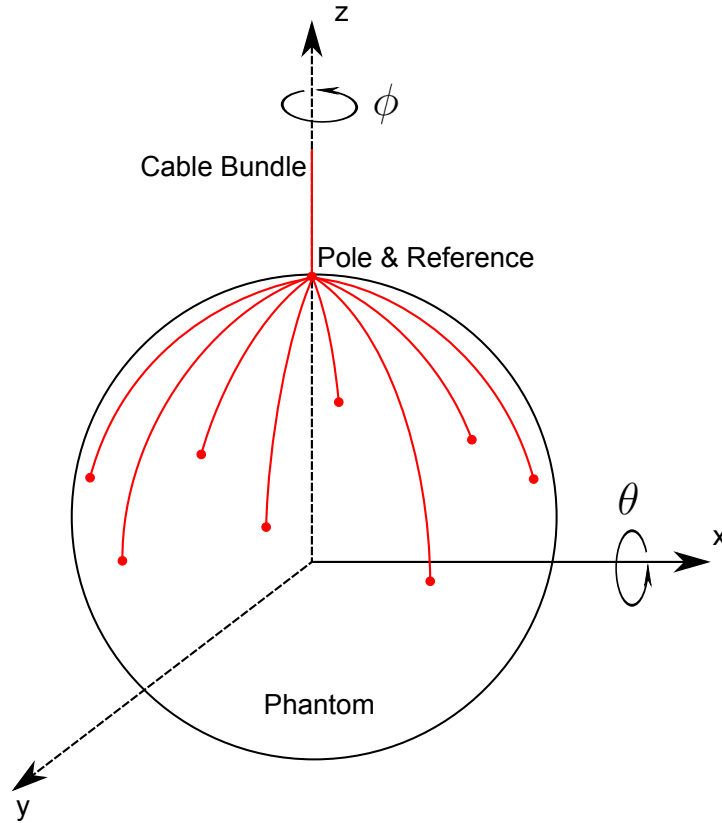
Figure 6.1: Schematic of spherical conductor (phantom) with electrodes and cables shown in red. Cables run from the electrode locations along lines of longitude across the surface of the phantom converging on the pole.

the reference electrode also located at the pole as depicted in Figure 6.1. These models are used here to produce expressions for the change in the artefact with respect to small changes in position and orientation due to a head nod, shake or z-translation.

Longitudinal Gradient

The model for the artefact voltages $V_z(\theta, \phi)$ produced on the surface of a conducting sphere (of radius r with electrodes at positions (θ, ϕ)) by a time-varying longitudinal gradient, G_z [94] is reproduced in Equation 6.8. The coordinates (x, y, z) define the position of the centre of the sphere relative to the iso-centre of the scanner. η characterises the angle of rotation about the x-axis, with positive η corresponding to a downward nod, while ζ characterises a rotation about the

z-axis, with positive ζ corresponding to a turn of the head to the left.

$$V_z = \frac{1}{4}\frac{dG_z}{dt}r^2\left[\theta\left(x\sin(\zeta+\phi)+\cos(\zeta+\phi)\sin\eta\left(2z-y\cot\eta\right)\right)\right.$$
$$\left.+2r\cos(\zeta+\phi)\sin\eta\left(\cos\eta\sin\theta-\sin(\zeta+\phi)\sin\eta(\cos\theta-1)\right)\right]$$

(6.8)

An expression for the change in induced artefact with respect to a change in the longitudinal position of the sphere, z, can be determined by taking the derivative of Equation 6.8 with respect to z and making the assumption that $\zeta = 0$ and that η is small:

$$\frac{dV_z}{dz} = \frac{1}{2}\frac{dG_z}{dt}r^2\theta\cos\phi\sin\eta$$
$$\implies \frac{dV_z}{dz} \propto \theta\cos\phi$$

(6.9)

Differentiating Equation 6.8 with respect to η and assuming $x = y = z = 0$, $\zeta = 0$ and that changes in η are small produces an expression for the change in the voltage induced by an applied longitudinal gradient with respect to a nod of the head.

$$\frac{dV_z}{d\eta} = \frac{1}{2}\frac{dG_z}{dt}r^3\sin\theta\cos\phi$$
$$\implies \frac{dV_z}{d\eta} \propto \sin\theta\cos\phi$$

(6.10)

Finally the change in induced voltage with respect to a rotation of the head towards the left or right is determined by differentiating Equation 6.8 with respect to ζ and assuming $x = y = z = 0$, η is small such that $\sin\eta \ll 1$ and that $\zeta = 0$.

116

$$\frac{dV_z}{d\zeta} = -\frac{1}{2}\frac{dG_z}{dt}r^3 \sin\phi \sin\theta \sin\eta \cos\eta$$

$$\implies \frac{dV_z}{d\zeta} \propto \sin\theta \sin\phi \tag{6.11}$$

Equations 6.9–6.11 suggest that the GA due to a longitudinal gradient will vary linearly with respect to small changes in position. Also, because of the $\sin\eta$ terms in Equations 6.9 and 6.11, the effect of a rotation about the x-axis on the GA due to a longitudinally applied gradient field is expected to be much greater than the effects of z-translation or rotation around the z-axis. By substituting values corresponding to the positions of the EEG electrodes (see Figure 3.7) into r, θ and ϕ, flat-maps of the expected change in GA can be plotted (see Figure 6.9).

Transverse x-Gradient

The expression for a voltage induced by a gradient applied along the x-direction is reproduced from Yan *et al.* in Equation 6.12.

$$V_x = \frac{1}{6}\frac{dG_x}{dt}r^2 \left[2r\left(\left(1 - \cos\theta\right)\sin\eta\cos 2(\zeta + \phi) - \sin(\zeta + \phi)\cos\eta\sin\theta \right) \right.$$

$$\left. + 3\theta\left(x\cos(\zeta + \phi)\sin\eta - z\sin(\zeta + \phi) \right) \right] \tag{6.12}$$

Expressions for the changes, due to positional variations, in the magnitude of the induced GA for an x-gradient on a channel whose electrode is positioned at location (θ, ϕ), can be derived by using a similar approach to that employed for the longitudinal gradient.

$$\frac{dV_x}{dz} \propto \theta \sin \phi \tag{6.13}$$

$$\frac{dV_x}{d\eta} \propto \left(\cos \theta - 1 \right) \cos 2\phi \tag{6.14}$$

$$\frac{dV_x}{d\zeta} \propto \cos \phi \sin \theta \tag{6.15}$$

Equations 6.13–6.15 suggest that the GA due to a transverse gradient applied in the x-direction will also vary linearly with respect to small changes in position. By substituting values corresponding to the positions of the EEG electrodes (see Figure 3.7) into r, θ and ϕ, flat-maps of the predicted change in GA can be plotted (see Figure 6.10).

6.3 Preliminary Experiment

Preliminary experiments were conducted using a spherical agar phantom. The objectives were to compare measurements with the theoretical expressions for the spatial variation of the change in GA components due to particular movements and to confirm the linear variation in the GA for small changes in position.

6.3.1 Methods

As in the experiments described in Chapter 5, a spherical, conducting, agar phantom (95.5 % distilled water, 4 % agar, 0.5 % NaCl) with a 20 cm diameter was made. However, this phantom contained a variety of agar shapes which were doped with Endorem. This iron-oxide-based contrast agent alters the transverse relaxation time of the protons in the water causing a difference in the image contrast of these sections in the images (see Figure 6.2). Adding structure to the phantom meant that it was easier to co-register images of the phantom acquired at different positions, thus making it possible to characterise accurately the movement of the phantom.
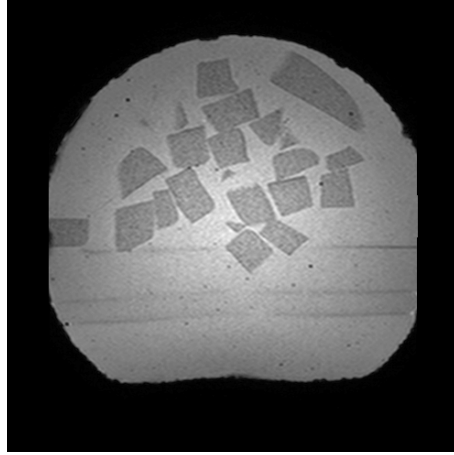
Figure 6.2: MRI of phantom with Endorem doped shapes produced using a T_2^* weighted GE sequence

MRI data were acquired on a Philips Achieva 3T MR scanner. A 3D, T_2^*-weighted GE-sequence was used to acquire structural data at each position, with parameters: TE = 10 ms, TR = 14 ms, flip angle of 15° and $200 \times 200 \times 180$ matrix size with resolution of $0.89 \times 0.89 \times 1 \, \mathrm{mm}^3$. These images were used in the analysis to determine by how much the phantom had moved. To assess the effect that a change in position had on the artefacts generated by the individual gradients the modified EPI-sequence described by Mullinger *et al.* [109] was used (7 volumes and 5 slices per volume). The modification involved adding sequential, trapezoidal pre-pulses on each gradient axis prior to each slice acquisition (see Figure 6.3). Each pre-pulse consisted of a 10 ms ramp up at a rate of $2 \, \mathrm{T\, m^{-1}\, s^{-1}}$ followed by a 10 ms plateau and 10 ms ramp down at the same rate. These pre-pulses produce bipolar square pulses in the EEG recordings, and the variation of the amplitudes between different phantom positions could then be used to assess the change in GA with position. EEG recordings were made using a 32-channel MR-compatible BrainProducts system with clock synchronization. The sampling rate was 5 kHz, high- and low-pass filter cut-offs were 0.016 Hz and 1 kHz respectively with a 30 dB/octave roll-off. The ribbon cable connecting the EEG cap to the amplifiers was fixed to a cantilevered beam in order to minimize cable movements and to isolate the cable from any vibrations of the scanner bed.

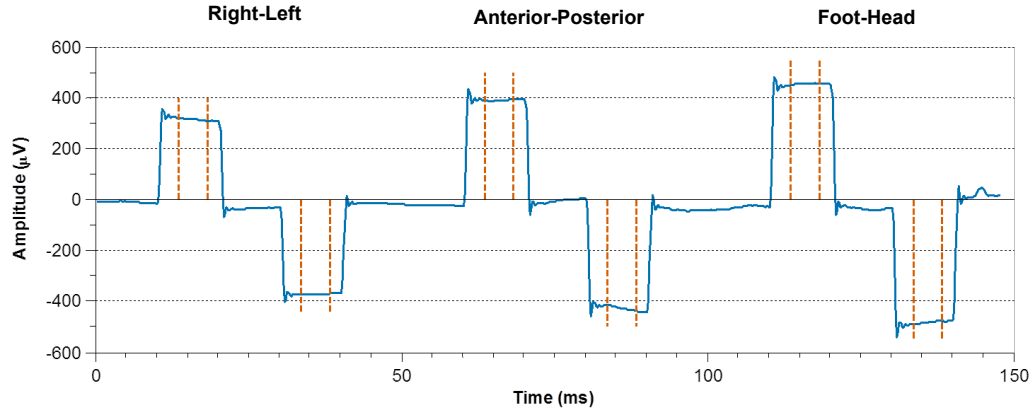Four different sets of recordings were made:

Figure 6.3: The bipolar square pulses induced on electrode Fp1 by the custom pre-pulses [109]. The dotted red lines shown define the segmented regions for assessing the magnitude of the induced gradient artefacts. The gradients which cause these induced square waveforms are sequentially applied in the right-left, anterior-posterior and foot-head directions

1. **Accuracy of co-registration of scans.** To gain a measure of the accuracy of co-registration, two identical images, with no change in the phantom's position, were acquired using the GE sequence. This gave a measure of the error in co-registration of images.

2. **Characterizing the effect of z-displacement.** The aim here was to study the variation of the GAs with respect to the z-position of the EEG cap and phantom. RF excitation and detection were carried out using the whole body coil and the Philips 8-channel SENSE head coil, respectively. To speed up the image acquisition process a SENSE factor of 2 was used. The phantom was initially positioned so that Fp1 and Fp2 were at the scanner's isocentre [109]. This position was defined to be 0mm along the z-axis. Using the scanner bed and a plastic ruler attached to the head coil, the position of the phantom along the z-axis was varied. At each location, the FFE and custom EPI scans were performed. Recordings were acquired on two separate occasions. In session A, movements of approximately ± 5 mm and ± 10 mm relative to the original position were made. During session B, the phantom was moved along the z-axis by approximately ± 2 mm, ± 4 mm, ± 6 mm, ± 8 mm and ± 10 mm, again with the original position defined as

zero.

3. **Investigating the effect of a rotation about the x-axis.** Here, RF excitation and detection were carried out using the whole body coil. The phantom was mounted within a custom-built gimbal, which allowed us to rotate the phantom around the x- and z-axes (see Figure 6.4). The gimbal was designed so that it attached to the MRI scanner's bed and fitted within the bore of the magnet. Adjustment screws allowed manual adjustment of the orientation of the phantom and a scale provided a precision of $\pm 0.5°$ in the rotations. The EEG cable bundle was fed through the gaps in the gimbal and attached to the ribbon cable. To explore the variation of the GA with small rotations about the x-axis, the phantom was initially positioned with Fp1 and Fp2 at the scanner's isocentre. This position was defined as $0°$. Again, recordings were acquired on two separate occasions. For session A, the phantom was rotated by approximately $\pm 5°$ and $\pm 10°$ about the x-axis. During session B the phantom was rotated by approximately $\pm 2°$, $\pm 4°$, $\pm 6°$, $\pm 8°$ and $\pm 10°$. The FFE and custom EPI sequences were run for each phantom position.

4. **Exploring the effect of rotation about the z-axis.** The methods employed were the same as those described in 3, except that, in this instance the rotations were made around the z-axis.

6.3.2   Analysis

The GE images were co-registered using SPM8. This provided a precise measure of the displacement of the phantom based on x, y and z-translations and rotations. This provided a measure of position change to which the differences in the GAs induced by the pre-pulses in the EEG recordings could be compared. The co-registration of the two images in recording set 1 were compared to give a measure of the errors involved in co-registration.
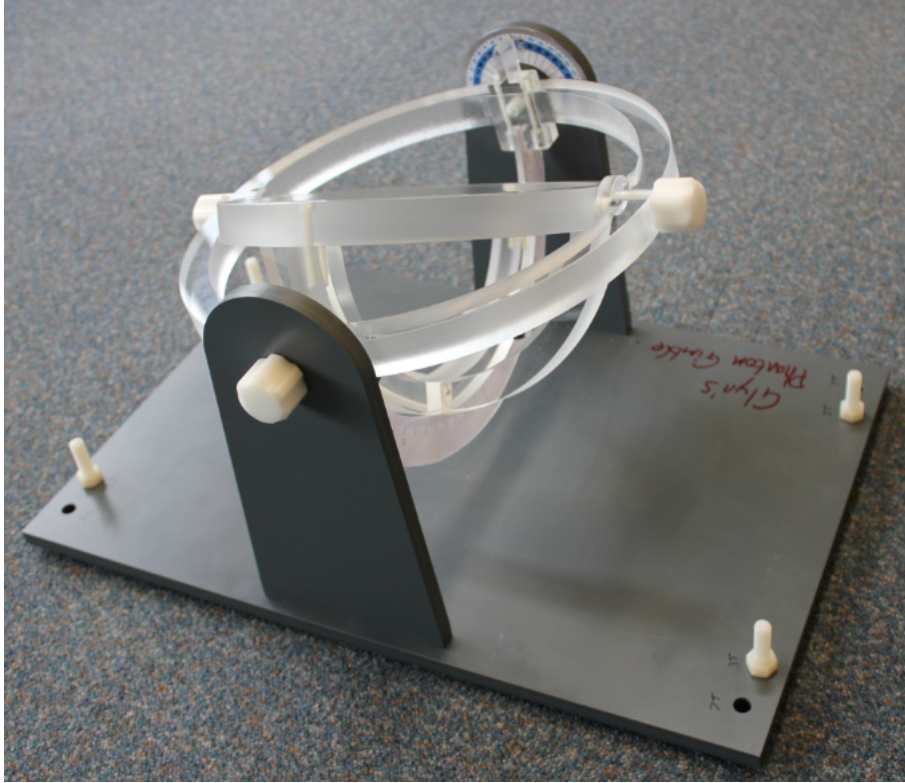
Figure 6.4: A custom gimbal for rotating the spherical phantom within the bore of the MRI scanner.

MatLab (Mathworks) was used to process the EEG data. The EEG data, were averaged across slice acquisitions before calculating the average GA over the central $5\,\mathrm{ms}$ of the ramp-up and ramp-down periods (as indicated in Figure 6.3). The difference between the average amplitude for each peak and trough for each gradient direction was then taken, giving a measure of the magnitude of the x, y and z-gradient artefacts induced at each position.

These difference values were then analysed in two separate ways:

1. **Single Variable Analysis:** For each of the three types of position change the measure of the induced artefact for a longitudinal, z-gradient and a transverse x-gradient are plotted against the measured movements for the z-translation and the z- and x-rotations respectively. Using the MATLAB function fit, estimates of the change in the artefact due to small displacements were calculated. Based on the assumption of linearity, the type of fit used was a simple, first-order polynomial fit. The gradients of the fit-

ted lines were then exported to Brain Vision Analyzer 2 (Brain Products) where they were plotted on flatmaps. The flatmaps were interpolated using spherical-splines of order 4 and plotted over a maximum angle of 120°. These flatmaps were then compared to simulated results based on the expressions in Equations 6.9 to 6.11 and 6.13 to 6.15

2. **Multiple Variable Analysis:** Because of the larger number of data points, only the data sets acquired from the session B were used in this analysis. The difference values for each position are plotted against the image number and the movement parameters are combined into a general linear model. These were then regressed using an ordinary least-squares fit to show that the magnitude of the artefacts vary linearly with position. R^2 values (a measure of the correlation between the actual and predicted values supplied by the fit) were calculated to assess the goodness of fit.

6.3.3 Results and Discussion

The co-registration of the images in recording data set 1 showed a net difference of 0.11 mm (Euclidean distance between phantom positions [see Equation 5.24]) and 0.016° (the magnitude of rotation about the Euler axis characterising the difference in phantom orientations [see Equation 5.25]) respectively. This indicates that the registration error is within acceptable bounds. Following this, the rest of the GE images were co-registered across the respective data sets to quantify the change in position of the phantom for each respective type of movement.

Figure 6.5 shows the results of the co-registration of the GE images from datasets 2–4 of phantom data acquired during session B. However, it seems an error occurred for one of the measurements. The phantom position for image 9 from the z-translation set of data appears to have only been displaced by 6 mm instead of the expected 8 mm. This is likely due to a misreading of the scale. However, this should not affect subsequent analyses and was therefore not excluded. The rest of the movement parameters are as expected, showing reasonable differentia-
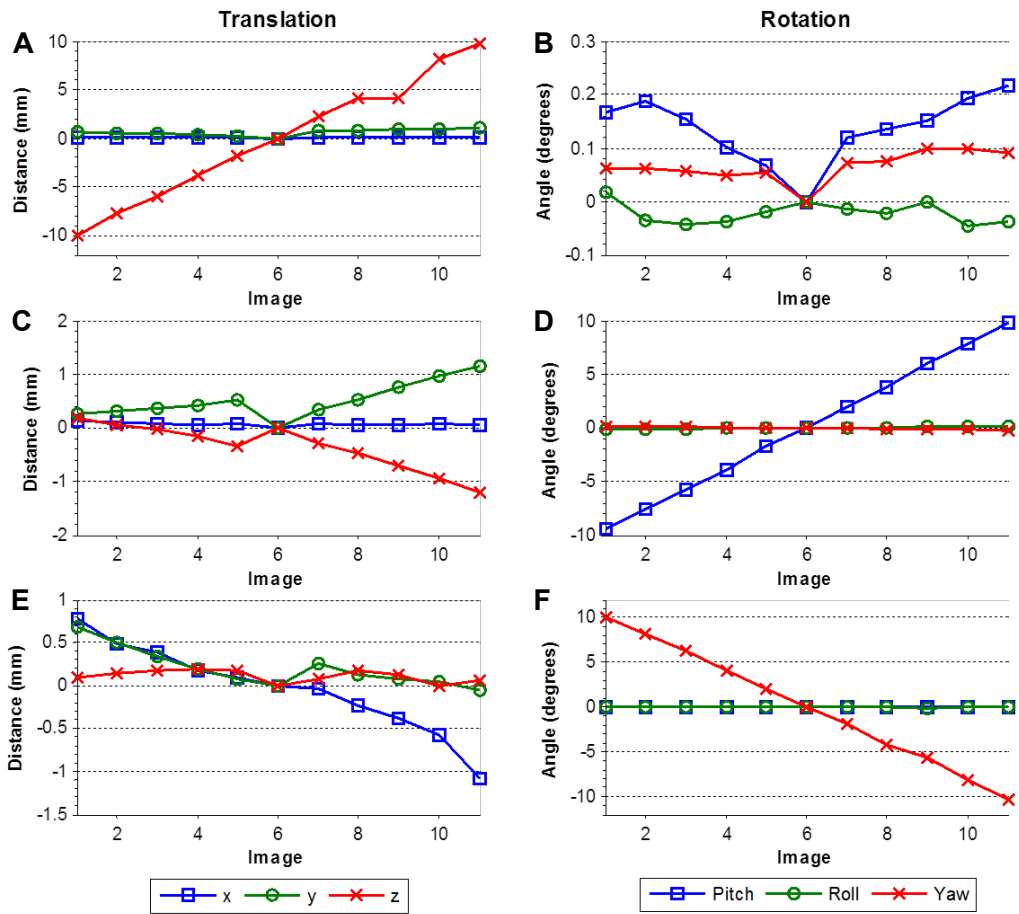
Figure 6.5: The translation and rotation parameters from the co-registered GE images for each of the three types of movement: z-translation (**A**&**B**), rotation about the x-axis (**C**&**D**) and rotation about the z-axis (**E**&**F**)

tion of the three different types of movement. However, there are components of measured movement that are significantly larger than the net co-registration errors along axes for which there should have been no displacement (i.e. Figure 6.5**E**&**F**). Rotational motions could introduce translational errors in two possible ways. If the centre of the circular phantom is not exactly aligned with the centre of rotation of the gimbal, then rotations may also produce actual translations of the phantom. The other potential source of error is that the estimated centre of mass of the phantom from the realignment algorithm may not correspond to the physical centre of rotation of the phantom. Additionally translational errors may be caused by heating of the passive shim elements, which can alter the average Larmor frequency and thus shift the image. However, the effect is much smaller than that of the dominant movements.

Single Variable Analysis

The fitted results for the change in the magnitude of the GA with respect to the set of typical head movements for a gradient applied along the z-direction are shown for a selection of electrodes in Figures 6.6–6.8. Similar results were obtained for the other gradients and types of movement. Overall, the induced artefacts appear to scale linearly with angle for the small movements considered here. However, there do appear to be some small, regular deviations from the line of best fit (for example, compare the plot for electrodes O2 and T8 in Figure 6.6). It is likely that these regular deviations are caused by components of the movement that differed across the range of angles considered. In Figure 6.7 there appear to be some quite significant random deviations within an interval of $50\,\mu V$ either side of the line-of-best fit. These deviations are particularly noticeable in plots 6.7**A**&**C**. In order to alter the position of the phantom along the z-axis it was necessary to disconnect the cable bundle from the ribbon cable. It is therefore likely that the path of the cable bundle varied randomly between recordings leading to a random variation in the amplitude of the GA not characterized by a change in position along the z-axis.
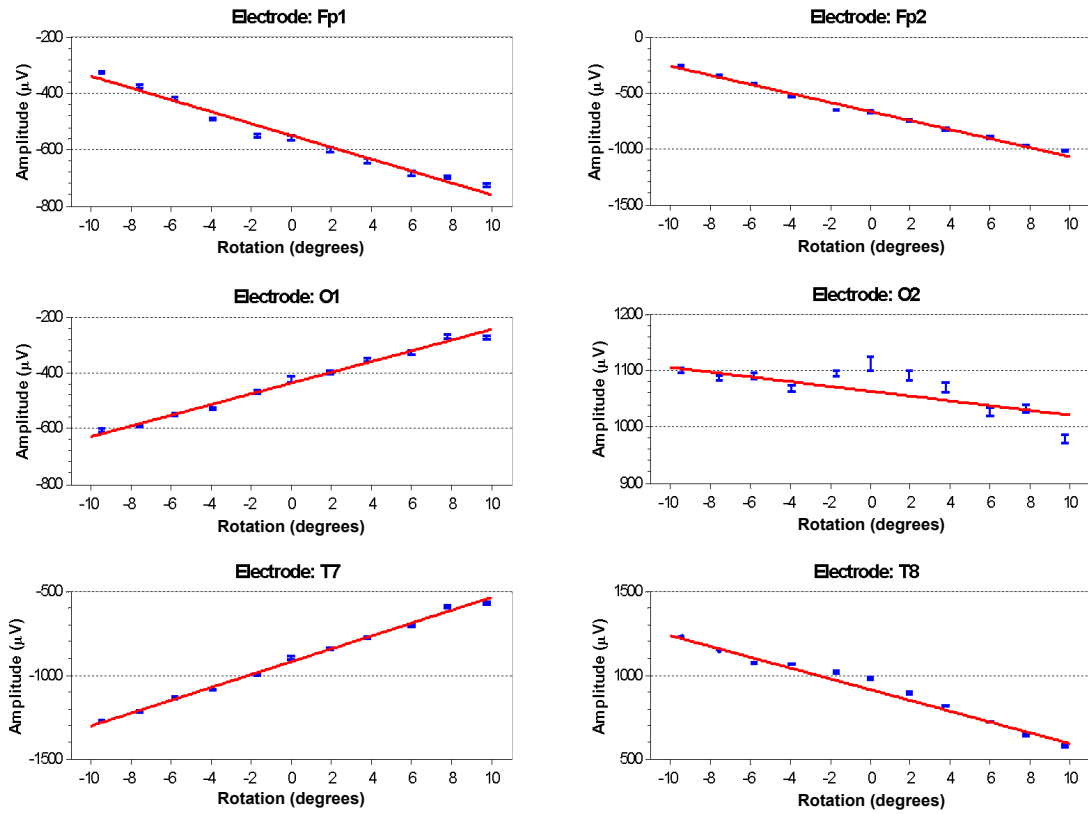
Figure 6.6: The change in amplitude of the GA due to a gradient applied along the z-direction for a rotation about the x-axis. Data were collected from the second session and a variety of representative electrodes have been chosen from across the surface of the phantom. Error bars show the standard error for the estimate of the change in GA.
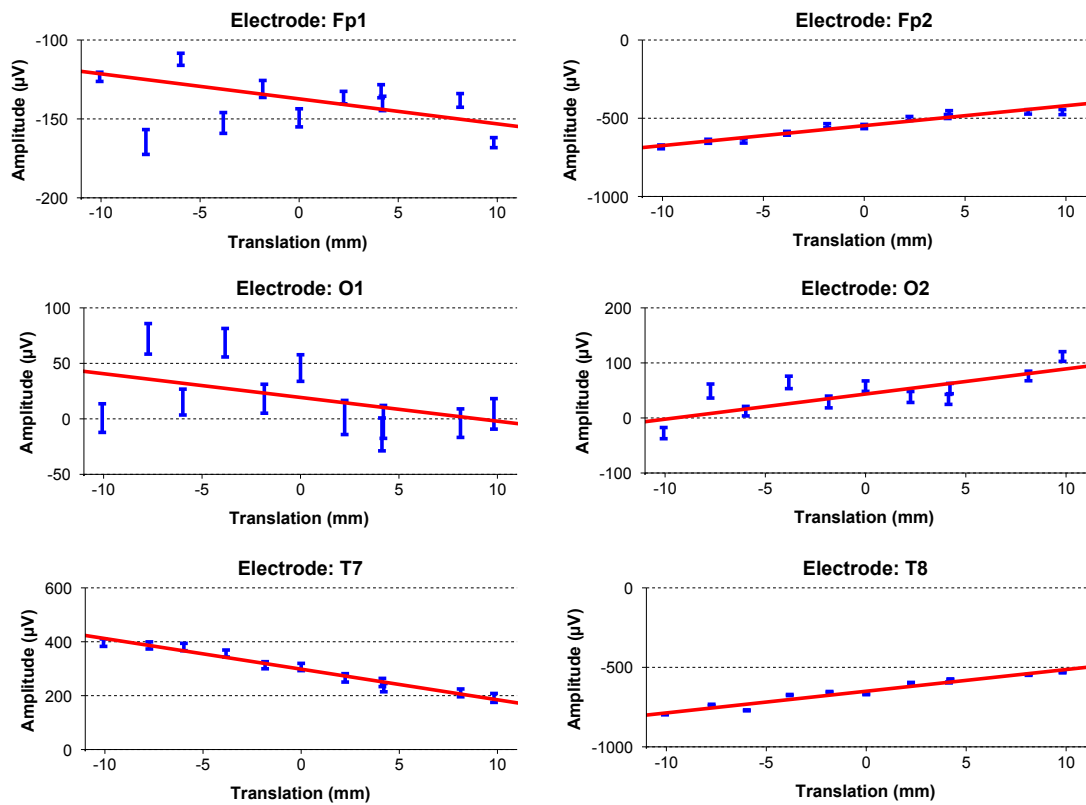
Figure 6.7: The change in amplitude of the GA due to a gradient applied along the z-direction for a translation along the z-axis. Data were collected from the second session and a variety of representative electrodes have been chosen from across the surface of the phantom. Error bars show the standard error for the estimate of the change in GA.

Figure 6.8: The change in amplitude of the GA due to a gradient applied along the z-direction for a rotation about the z-axis. Data were collected from the second session and a variety of representative electrodes have been chosen from across the surface of the phantom. Error bars show the standard error for the estimate of the change in GA.
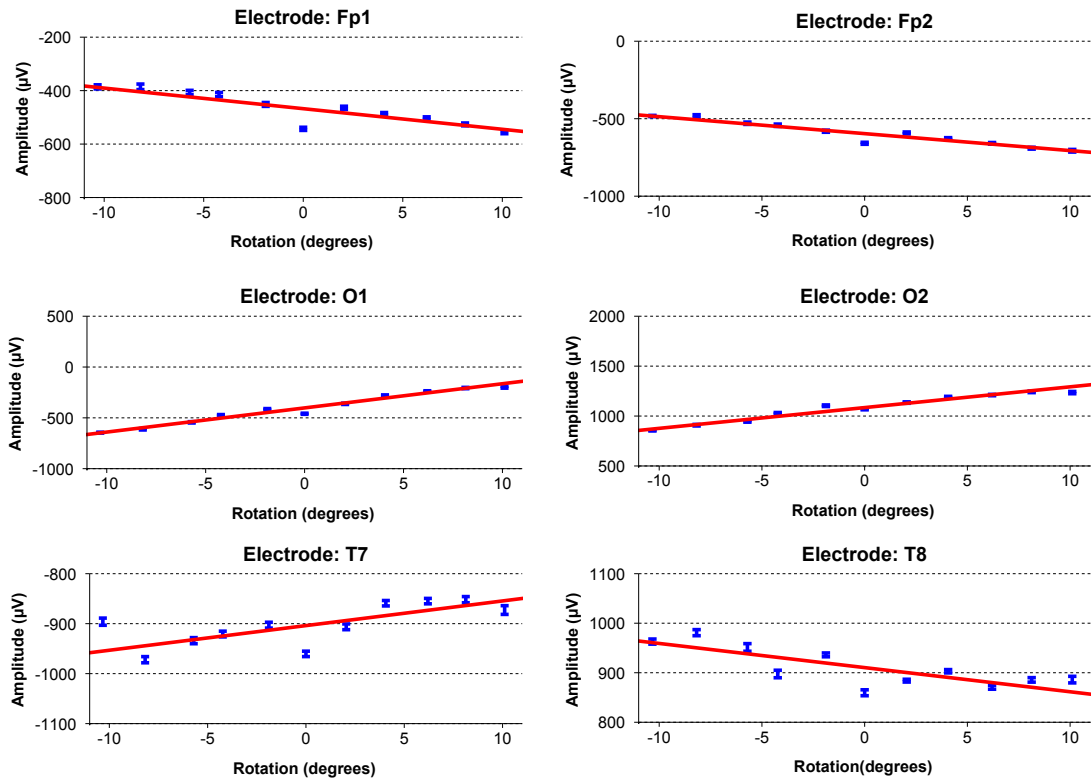
The gradients of the lines of best fit from all electrodes were plotted on flat-maps using Brain Vision Analyzer 2. These were then compared to simulated results generated from Equations 6.9 to 6.11 and 6.13 to 6.15. The results of this approach can be seen in Figures 6.9 and 6.10. It is clear that the shapes of the results across the electrodes match reasonably well with the patterns expected from theory. z-translation and rotation about the z-axis does produce a much smaller variation in the artefact than a rotation around the x-axis for both the longitudinal, z-, and transverse x-gradients (see Figures 6.9 and 6.10). The smaller variations in the magnitude of the GA may help explain why there are more obvious discrepancies between the shape of the patterns from the experimental data and the theoretical predications for the z-translation and rotation about the z-axis. This is because the calculated gradients for the smaller variations in GA with respect to position will be more susceptible to random noise than the calculated gradients for types of movement which produce a larger variation in the GA. Discrepancies may also be associated with the assumptions made for the models. For example, the models assumed that the wire paths ran along lines of longitude across the surface of the phantom, whereas in reality the wires follow more complicated paths. Also it is assumed that, there is no deformation of the wire paths during the movements, this also is unlikely to be true, but it is unclear what non-linear effect, if any, this would have on the results. Because of the $\sin \eta$ term in Equations 6.9 and 6.11 it was expected that the change in amplitude of the GAs due to the longitudinal gradients (foot-head) would be smaller for both z-translation and rotation about the z-axis. This expectation was confirmed by the experimental measurements.

Multiple Variable Analysis

For the multiple variable analysis, the movement parameters were collected together into a general linear model. This model was then regressed from the data characterising the change in amplitude of the GA for different gradient directions and different movements. The results of the fit and the residuals for a selection of types of dominant movement, gradient direction and electrodes can be seen in
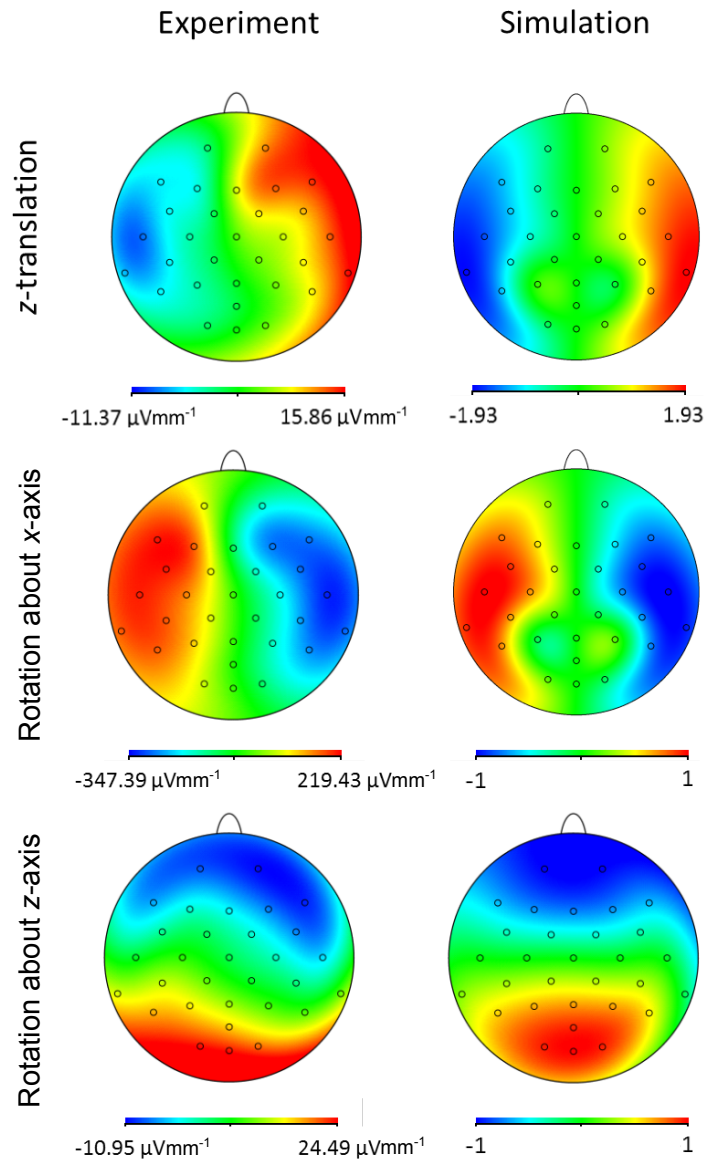
Figure 6.9: Comparing theoretical and experimental scalp patterns of the change in amplitude of GA due to a time-varying longitudinal gradient (foot-head) of magnitude $2\,\mathrm{T\,m^{-1}\,s^{-1}}$ with respect to various typical movements.
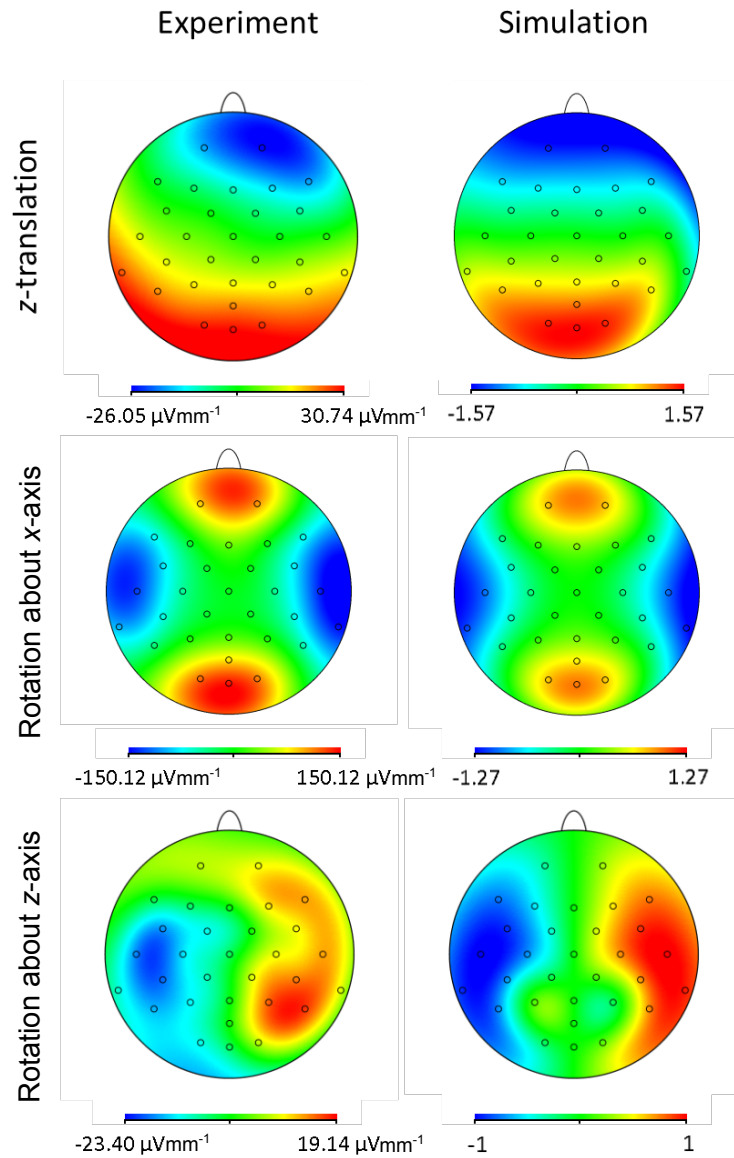
Figure 6.10: Comparing theoretical and experimental scalp patterns of the change in amplitude of GA due to a time-varying x-gradient (right-left) of magnitude $2\,\mathrm{T\,m^{-1}\,s^{-1}}$ with respect to various typical movements.

Movement	Gradient	R^2
	AP	0.99 ± 0.01
x-**Rotation**	RL	0.93 ± 0.09
	FH	0.99 ± 0.03
	AP	0.97 ± 0.05
z-**Rotation**	RL	0.989 ± 0.007
	FH	0.95 ± 0.07
	AP	0.9 ± 0.1
z-**Translation**	RL	0.95 ± 0.09
	FH	0.91 ± 0.10

Table 6.1: The goodness of fit measures for the multiple variable regression analysis. Mean values and standard deviations of R^2 were calculated across all 31 electrodes for each type of movement and each gradient direction.

Figure 6.11.

Overall, by fitting the movement parameters, the variations in the amplitudes of the GA across positions for each gradient direction were well characterised. Residuals after regression were mostly within the range $\pm 20\,\mu V$ across all electrodes and datasets. The goodness-of-fit was assessed using the R^2 measure. The average and standard deviation of these R^2-values across channels for each data set are reported in Table 6.1.

While the movement parameters were able effectively to characterise the variation in the amplitudes of the GAs, there appears to be a problem of estimation bias for the scaling parameters output by the fitting. Plotting these fit parameters across the surface of the phantom yielded patterns which were not similar to the flat-maps from the theoretical models or the single variable analysis (Figures 6.9 and 6.10). This is most likely due to correlations between the movement regressors. For example, the yaw and x-movements in Figures 6.5E&F show correlated changes. This can also be seen in the pitch and roll in Figure 6.5D or the y and z movement parameters shown in Figure 6.5C.

To avoid estimation bias, recordings with random and mixed variations in position could be made. This would mean that there would not necessarily be similar trends in the movement parameters and therefore unique solutions to the fitting problem
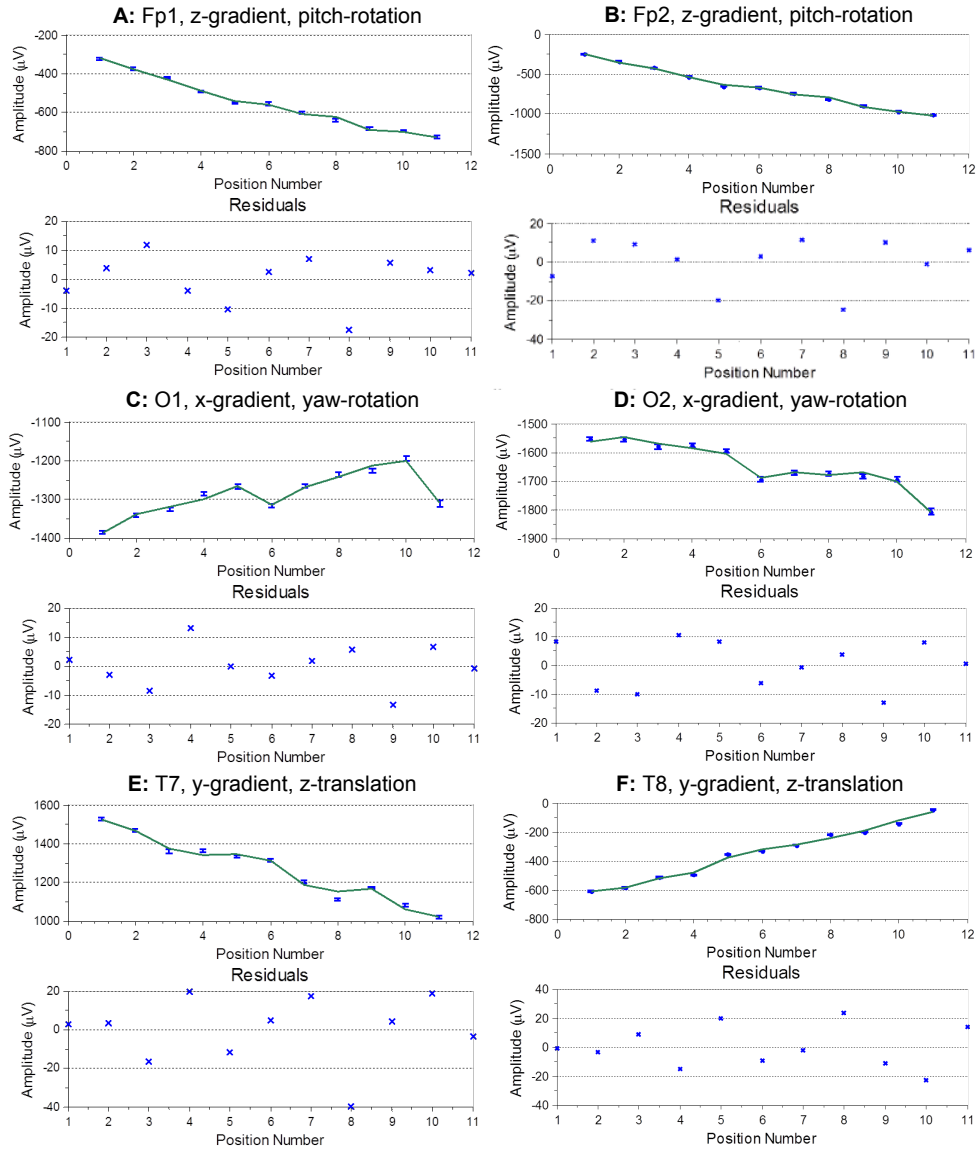
Figure 6.11: Amplitude data from various electrodes acquired for different phantom positions and orientations during session B for gradients applied along different directions. The data are plotted with the line of best fit from the multi-variable regression in the top graph. The bottom graph shows the residuals from the regression. **A**&**B** show the results of the fitting for electrodes Fp1 and Fp2 respectively with a gradient pulse applied along the z-direction. The phantom was rotated around the x-axis with eleven approximately equally spaced positions between $-10°$ and $+10°$. **C**&**D** show the results for electrodes O1 and O2 respectively, with a gradient pulse applied along the x-axis and different phantom orientations around the z-axis between approximately $-10°$ and $+10°$. **E**&**F** show the results for electrodes T7 and T8 respectively, with a gradient pulse applied along the y-axis for various, equally spaced positions along the z-axis between approximately $-10\,\mathrm{mm}$ and $+10\,\mathrm{mm}$. Error bars show the standard error for the estimate of the change in GA.

could be found. This type of experiment might also yield more information about the relative contributions of each type of movement to the change in amplitude of each GA component.

In conclusion, the flat-maps from the single variable analysis (Figures 6.9 and 6.10) were in strong agreement with the predicted spatial variation of the change in GA with respect to position. It also seems highly likely that the magnitude of the GA components vary linearly with respect to position as the multiple variable analysis is able effectively to characterise the change in GA. However, to confirm definitively the linearity, further experimentation may be required. For the remainder of this Chapter, it is assumed that the magnitude of the GA components vary linearly with respect to small changes in subject position.

6.4 Methods

Simultaneous EEG-fMRI recordings were made on three healthy human volunteers. fMRI data were acquired using a Philips Achieva 3T MR scanner. RF excitation was carried out using the whole body coil with a flip angle of 80°, while the signals were measured using the 32-channel SENSE head coil. A standard EPI sequence was used to acquire 20 slices of fMRI data with TE=40 ms, TR=2 s and a SENSE factor of 2.3. The matrix size was 80×77 with a resolution of 3×3 mm^2 and the slice thickness was set to 3 mm. For each recording 220 volumes (~ 5 min) were acquired. Dynamic Stabilisation was switched off.

EEG recordings were made using a 32-channel BrainAmp MR plus amplifier, Brain Vision Recorder software (Brain Products) and a BrainCap (EasyCap). Electrodes were placed according to Figure 3.7. The data were recorded with a 5 kHz sampling rate and band filtered to the range 0.016–250 Hz with a roll-off rate of 30 dB/octave. Synchronisation of the MRI and EEG clocks was achieved by using the SyncBox (BrainProducts GmbH).

Figure 6.12 shows a schematic explaining the implementation of the difference model subtraction (DMS) method. Each recording was split into two stages, a

prep-period and an experimental period. During the prep-period subjects were visually cued to make two small changes in position of the head for each type of movement (z-rotation, x-rotation and z-translation) before returning to the initial position. Each position was held for 8 TR-periods (16 s), giving 160 slices of GA data for each position. During the experimental period, subjects were visually cued to make small, head movements to simulate the typical position changes that might occur during an EEG-fMRI experiment. Subjects were instructed to make small positional changes along a single axis (simple) for 2 recordings, and subsequently in any direction (complex) for another 2 recordings. During each experimental data recording, 6 positional changes were made ~ 39 s apart so as not to be separated in time by a multiple of the TR-period. The MR images were co-registered using SPM8 to estimate the size and direction of the movements made by the subjects.

To form templates of the change in GA with respect to the different types of change in position, each set of 160 slices were averaged together. These average waveforms were then subtracted from each other for each type of movement to form a set of difference models (see Figure 6.12) for each EEG channel. The data acquired during the experimental period were corrected using AAS (template formed over all slices) in Brain Vision Analyzer 2.0. The difference models were then fitted to, and subtracted from, each slice-GA using the customised, regularised least-squares method (see Chapter 5, Equation 5.23).

To compare the level of residual artefacts after AAS and AAS-DMS, the EEG signals before and after correction using the different methods were Fourier transformed and the average signal magnitude at each slice harmonic (10 Hz fundamental frequency) over a bandwidth of 0.4 Hz was found. The attenuation of the GA relative to raw data produced by each correction method were then calculated. Differences in performance between AAS and AAS-DMS at each harmonic of the GA were evaluated for significance using a paired Wilcoxon signed rank test.
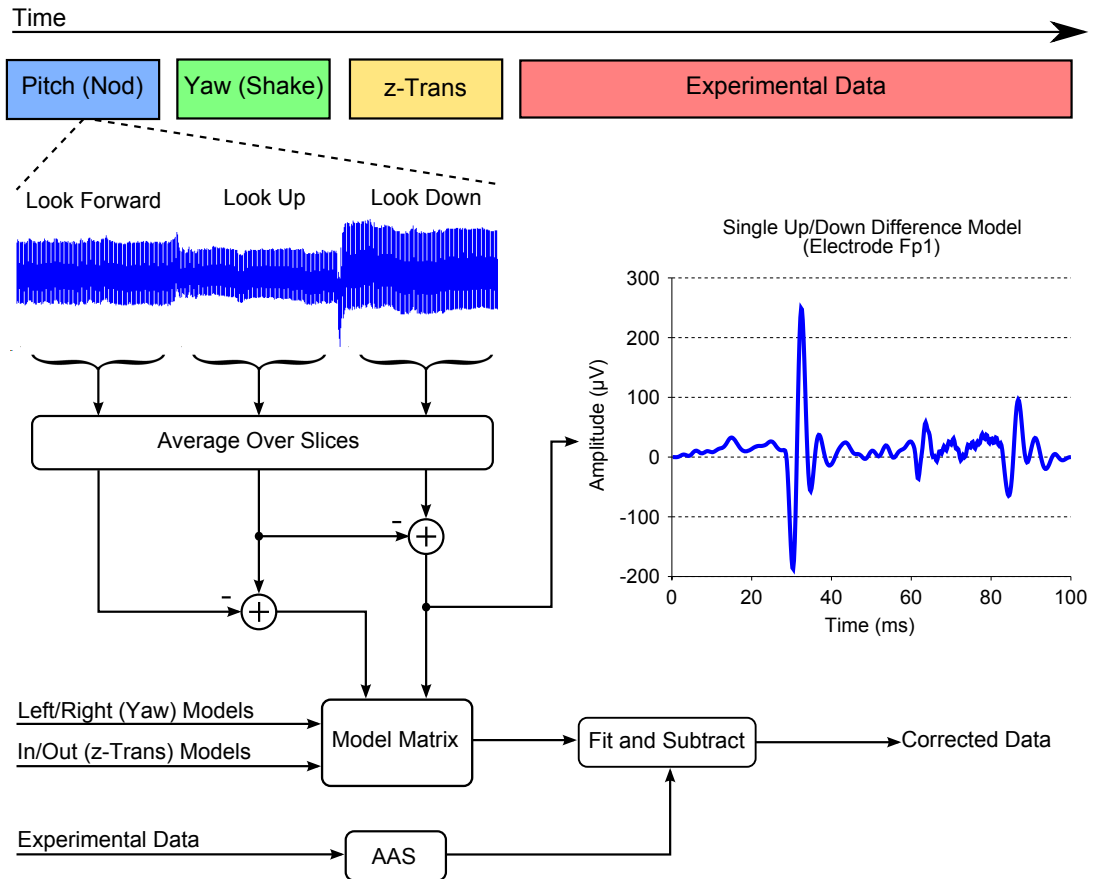
Figure 6.12: Schematic of the AAS-DMS method. Using slice markers output by the MRI scanner, slice-average GA are calculated at each head position. The differences in the GA for each basis movement are calculated and combined into a linear model of the change in GA with position for each channel. The models are then fitted and subtracted from the experimental data after AAS correction. The inset shows a single difference model of the GA on electrode Fp1 for head pitch.

6.5 Results

Models characterising the change in GA with respect to a basis set of movements were successfully generated from data acquired during the prep-period. Examples of these models for a selection of electrodes from a single data-set can be seen in Figures 6.13–6.15.

Overall, AAS-DMS performs significantly better than AAS alone for all recorded, movement corrupted data. Figure 6.16 shows example raw data and residuals after both correction methods for segments before and after an instance of subject movement. In agreement with Chapter 5, it is clear, from the raw data (see Figures 6.12 and 6.16), that the subject movement has a substantial affect on the size and shape of the GA. The performance of AAS is severely compromised by the movement, meaning that visible residual GA remains in the corrected EEG data (see Figure 6.16). This residual GA was between one and three orders of magnitude larger than typical brain signals in an EEG recording. Applying DMS after AAS significantly attenuates these residual components across all recordings.

Comparisons of the performance of both methods across all the recorded data are reported in Figure 6.17. Attenuations of the harmonic components of the fundamental slice frequency (10 Hz) produced by using AAS or AAS-DMS were calculated for each EEG channel for the data sets with simple and complex movements. These were then averaged across channels and then across all data sets collected from the three subjects. For both simple, single axis movements and for complex, mixed axis movements the performance of AAS-DMS was significantly better than AAS alone across the majority of harmonics. For the simple movements (Figure 6.17A), there is a greater attenuation of the harmonic components for both methods when compared to the complex movements (Figure 6.17B). However, there is a larger difference in the attenuations achieved when using AAS compared to AAS-DMS for the complex movements than for the simple movements. For simple movements, the average difference between attenuations using the AAS and AAS-DMS methods for harmonics above 50Hz was 4.5 ± 0.2 dB; while for complex movements it was 5.7 ± 0.3 dB.

Figure 6.13: Plots of DMS models formed from data recorded on healthy human subject at electrode location Fp1. The models represent the differences in the GA with respect to small position and orientation changes along axes describing pitch (**A**), yaw (**B**) and z-translation (**C**) type movements.
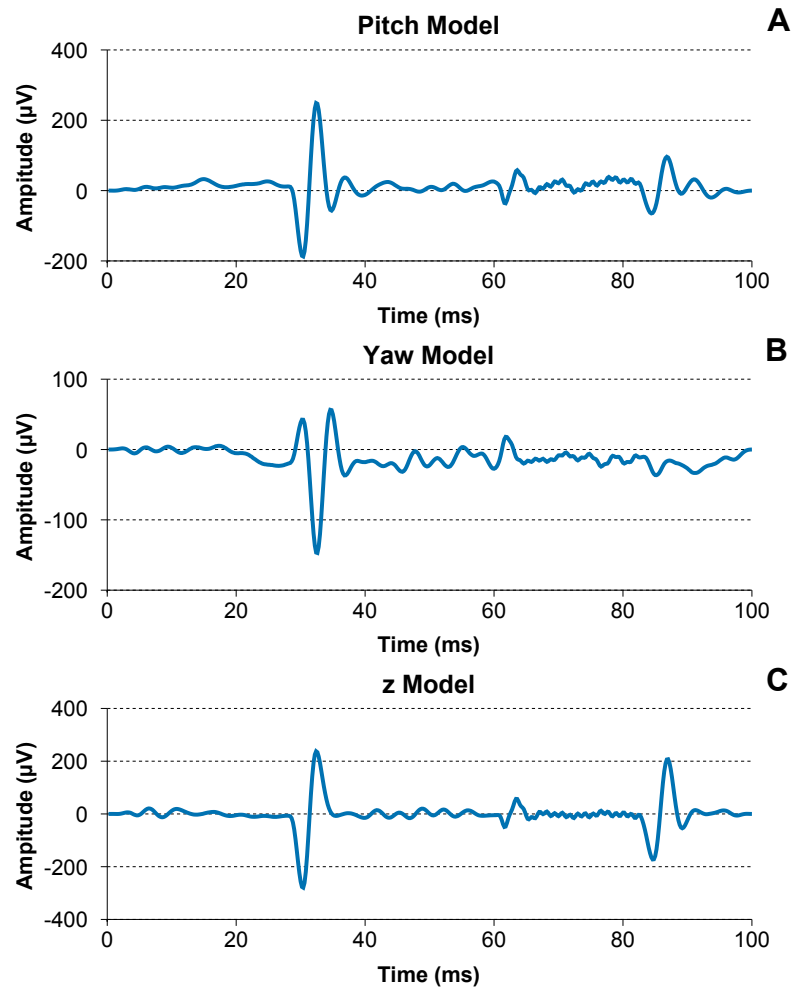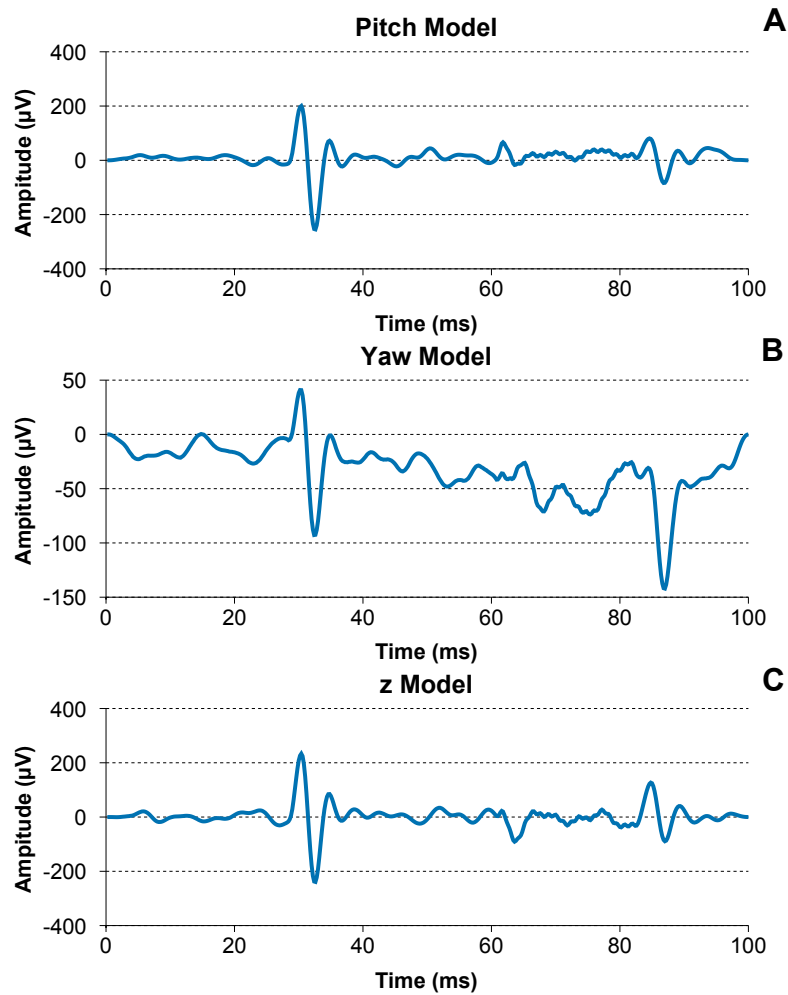
Figure 6.14: Plots of DMS models formed from data recorded on healthy human subject at electrode location O11. The models represent the differences in the GA with respect to small position and orientation changes along axes describing pitch (**A**), yaw (**B**) and z-translation (**C**) type movements.

Figure 6.15: Plots of DMS models formed from data recorded on healthy human subject at electrode location T7. The models represent the differences in the GA with respect to small position and orientation changes along axes describing pitch (**A**), yaw (**B**) and z-translation (**C**) type movements.
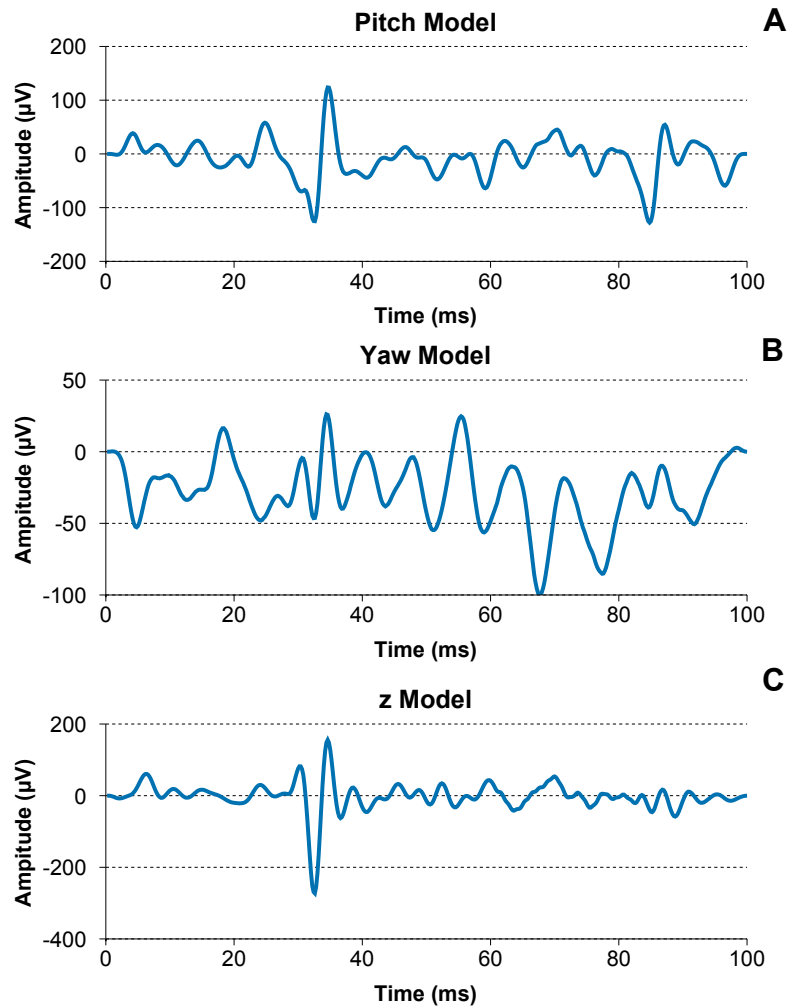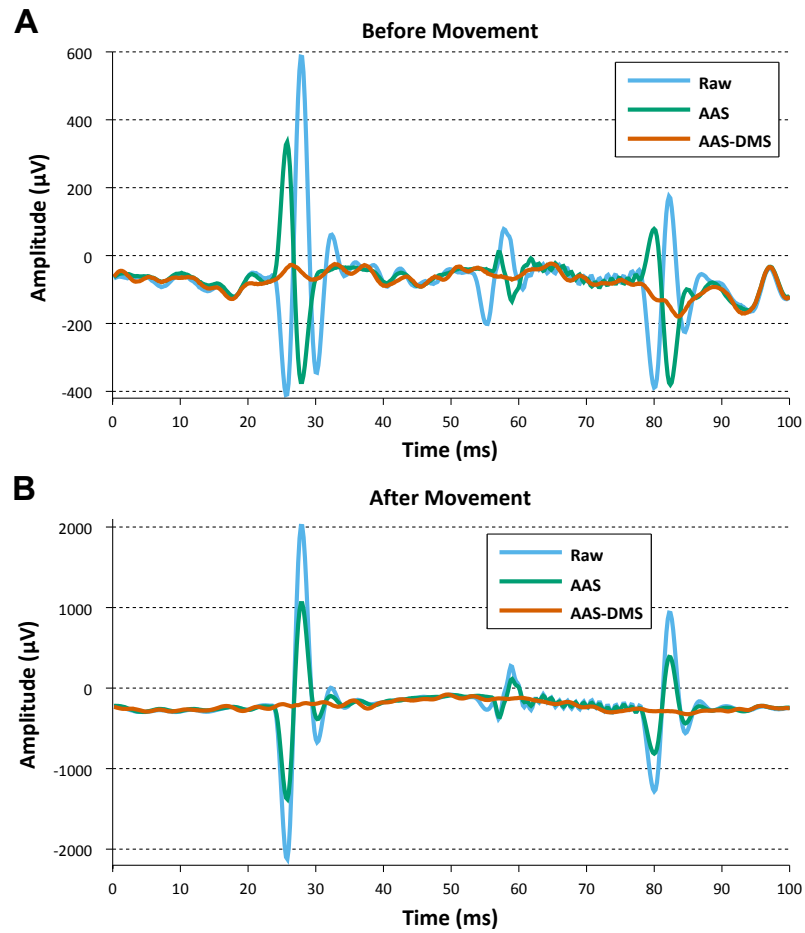
Figure 6.16: Raw GA (blue) and the residual GAs after correction with AAS only (green) and with subsequent use of DMS (orange) in movement-corrupted EEG data recorded on electrode Fp1 for a representative subject. The data shows a single slice acquisition before (**A**) and after (**B**) a complex head movement had occurred.

Figure 6.17: Average attenuation of signal power over all channels when using AAS alone or AAS-DMS. For simplicity, only the attenuations of every third harmonic of the fundamental frequency (10 Hz) for the simple movements (**A**) and complex movements (**B**) are shown. Error bars show the standard deviation across data sets and subjects. * denotes significant difference (p<0.05) in performance of AAS and AAS-DMS (Wilcoxon signed rank test).
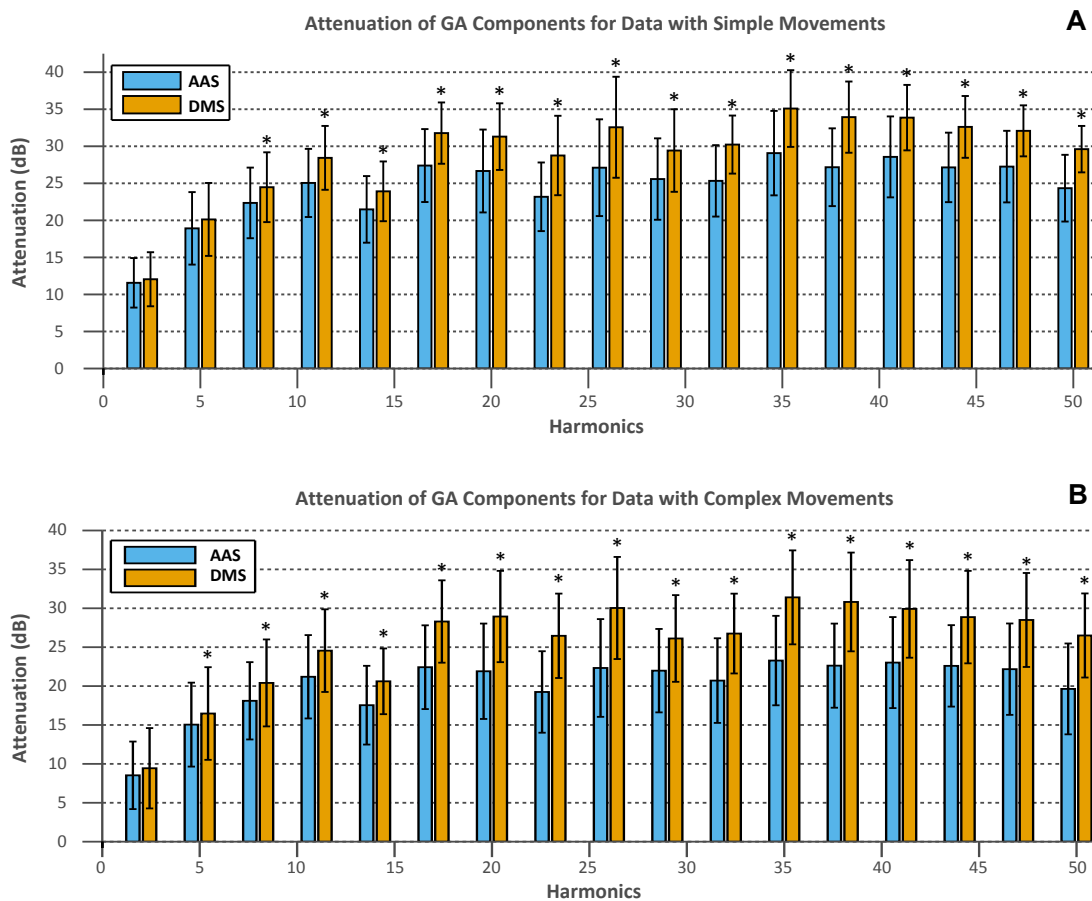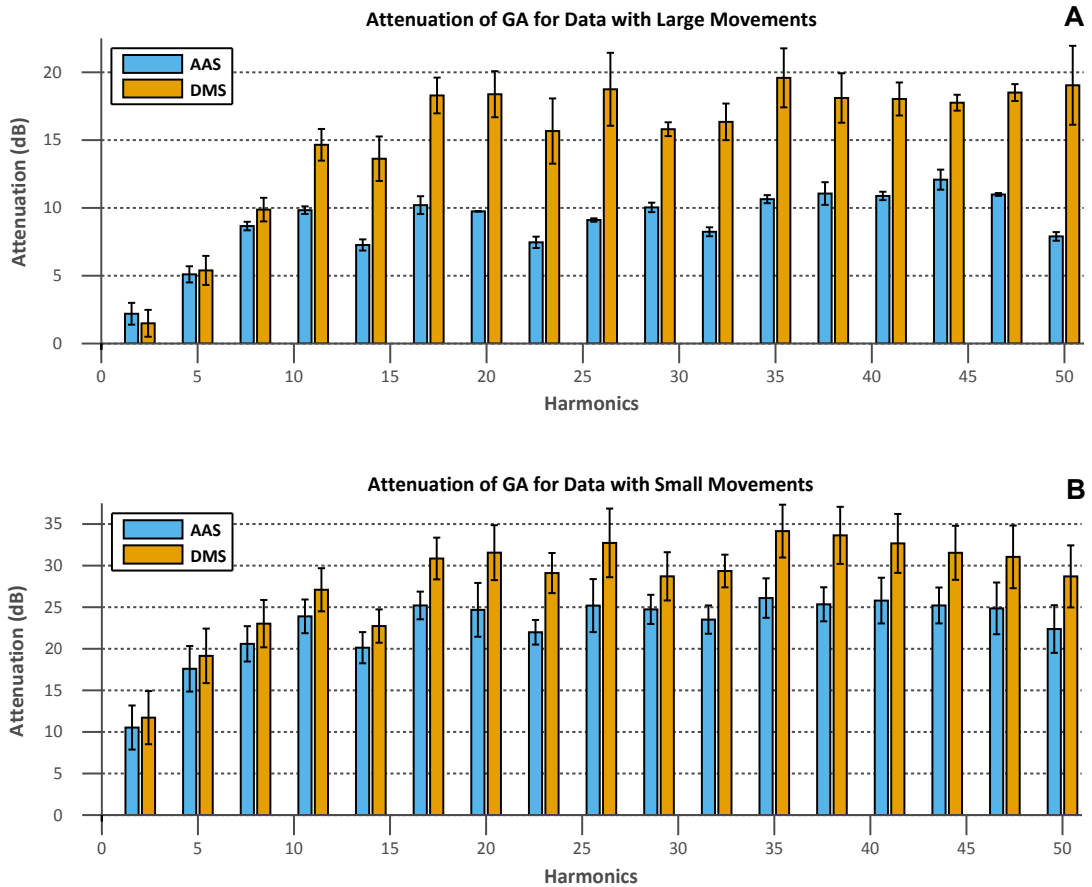
Figure 6.18: Average attenuation of signal power over all channels when using AAS alone or AAS-DMS. The attenuation of every third harmonic of the fundamental frequency (10 Hz) for the data sets containing large, complex movements (**A**) and those containing small complex movements (**B**) are shown. Error bars show the standard deviation across data sets and subjects.

It was noticed that for two of the subjects the movements were small. Their net displacement from the initial position was no larger than ±5 mm and ±5° across all their recordings. The third subject performed substantially larger movements with the majority within the range ±20 mm and ±20°, with one instance of a movement of approximately 25 mm. A comparison of the data sets acquired during small, complex movements with those acquired during larger, complex movements of the attenuation of harmonics of the GA by each method can be seen in Figure 6.18. While the performance for both methods is overall, better for smaller subject movements, the use of AAS-DMS shows a much larger improvement over AAS for the data set corrupted by larger movements.

6.6 Discussion

In this study, a novel, GA correction method which accounts for the effect of small subject movements was developed and the performance was evaluated for multiple recordings from three healthy subjects. The technique is an extension of the widely used GA correction method (AAS), originally proposed by Allen *et al.* [2]. The results show that applying DMS after AAS provides a significant improvement in GA correction over the use of AAS alone when the experimental data has been corrupted by subject movement. This is reflected both visually in the time series (see Figure 6.16) and the harmonic measures (Figures 6.17 and 6.18).

As expected from theory (see Chapters 4 and 5 and the theory section of this chapter), previous experiments (see Chapter 5) and the work of others [118, 119] head movements severely impair the performance of AAS. However, the residuals left behind were found to be well characterised by the difference models created using the DMS method as predicted in the theoretical model work, described above (see Equation 6.7). While the performance of the DMS method may be affected by larger head movements (see Figure 6.18), it is less susceptible than AAS to the effect of large movements.

For the work detailed here, it was assumed that the most likely head movements could be described by a basis set comprising rotations about the x- and z-axes as well as translation in the z-direction. This assumption appears to have worked well. Additional movements could easily be added to the prep-period to capture the effects of other types of head movement. However, it is doubtful that these will offer much more value to the DMS method and will also increase the scan duration, which is generally undesirable.

For this work, two models were produced for each type of movement. However, it is possible to reduce this to only one model per movement. This would have the advantage of reducing the additional scan time required. On the other hand, having two models means that if anything goes wrong in the prep-period such that one of the models is affected (for example, too large a movement or additional

movements) the second model can readily be used to correct the EEG data.

The data were acquired using the Brain Products Sync Box to synchronize the MR scanner and EEG clocks and the slice TR was selected to be an integer multiple of the sampling period. This ensured that the artefact waveforms were sampled at the same times over all slices. It is important for any template based correction method (such as AAS) that the sampling of the GA is consistent across the chosen template periods [116]. AAS-DMS is not an exception to this and could be severely affected in cases of unstable or no synchronization. This means that the data for forming the models needs to be acquired during the same run as the experimental data. Thus ensuring that the sampling points of the models align perfectly with the sampling points of the GA across all slices.

AAS-DMS is well suited to dealing with any EEG-fMRI experiment where subject movement is likely to occur; for example, studies involving patients or children. Additionally, AAS-DMS appears to perform very well in eliminating the high frequency ($>50\,\text{Hz}$) components of the GA (see Figure 6.17). This means that this technique could be applicable to studies of gamma band activity. One of the main limitations of the DMS method is that the method can significantly increase the scan duration as a period for collecting the data required for forming the models needs to be collected at the beginning of every scan. Also, the method requires the subjects to be able to follow very specific instructions at the beginning of each scan so that the models are able to characterise all likely, small variations in the head position.

A potential extension of the AAS-DMS method would be to include non-linear components within the DMS models. So far it has been assumed that the GA will vary linearly with changes in position. While, this assumption does appear to work very well, as demonstrated by the preliminary experiments presented in this chapter, it is possible that deformation of the wire paths may add subtle non-linearities to the GA. For correcting such effects for the PA, Le Van *et al.* [99] propose a method for generating and including additional non-linear components in their model. Their work showed that this approach offered a significant im-

provement in PA reduction over simply a linear method. As a result their work suggests that non-linear effects on the EEG artefact components due to subject movement can be a problem. A similar approach could be employed to account for non-linear effects within the DMS method.

6.7   Conclusion

The results presented in this chapter show that using DMS after AAS offers significantly improved performance over the use of AAS alone when small subject movements occur during EEG-fMRI experiments. DMS is easy to apply without the need for additional MR pulse programming and only requires a maximum of 5 min of additional data acquisition at the beginning of an experiment. AAS-DMS is shown to attenuate the high frequency GA components and should therefore be highly beneficial for investigation of gamma frequency band neuronal activity. It is also likely to be beneficial for subject groups, such as children, where significant movement is likely to occur during data acquisition.

Chapter 7

Comparison of GMF and DMS

7.1 Introduction

Both the GMF (Chapter 5) and DMS (Chapter 6) methods offer an improvement on GA correction in the presence of subject movement over the commonly used AAS method. Moreover, both methods have been shown to be effective at attenuating high-frequency GA components, thus extending potentially the usable bandwidth of EEG recordings acquired simultaneously with fMRI. However, it is unclear which of the two methods perform best. Therefore, some experiments which directly compare the performance of the two methods should be carried out. Some preliminary results produced by applying the two methods to the same data are described in this chapter.

7.2 Methods

Three different EEG recordings were made on one healthy human volunteer in a Philips Achieva 3 T MR scanner using a 32-channel EEG system (Brain Products, 5 kHz sampling rate, 250 Hz low-pass filter, with MR and EEG clocks synchronised). MRI data were acquired using a standard EPI sequence (285 volumes, 80x80x20 matrix, $3 \times 3 \times 3 \, \text{mm}^3$ voxels, TR = 2 s, TE = 35 ms). Each record-
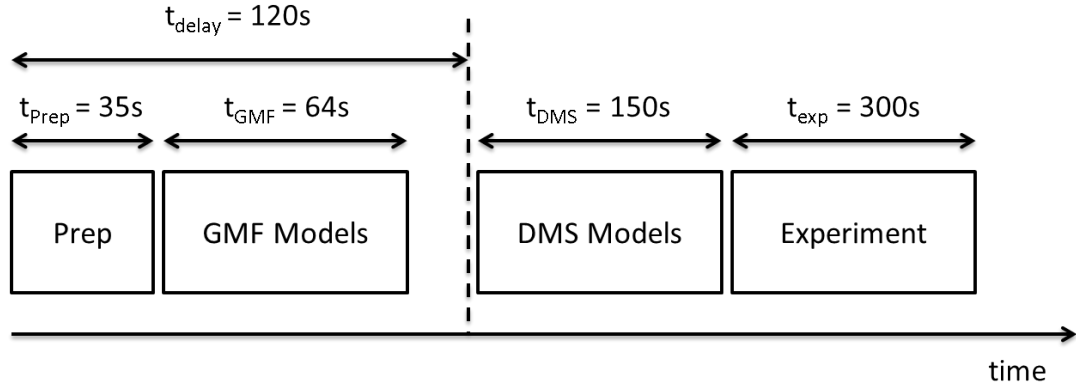
Figure 7.1: A schematic showing the splitting of the recordings into the various sections for forming the different models and performing the experiment. t_{prep} is the preparation time between the MR scanner operator initiating the scan and the start of the data collection. After this period of time are the two segments where data is collected for the forming the models for the GMF and DMS methods. Since t_{prep} can be very variable between separate recordings a pause of approximately 20 s was inserted between the periods for acquiring the GMF model data and the DMS model data preventing any possible overlap between the GMF and DMS model segments. The experimental period follows the model recording stages. The whole recording lasts approximately 9.5 min (285 volumes)

ing was split into three stages: recording of data for derivation of GMF models, recording of data for derivation of DMS models and an experimental period (see Figure 7.1).

During the first period, data for forming models for each GA component were sequentially recorded by nulling three of the four waveforms (RF, read, phase or slice) in turn for periods of 8 volume acquisitions per component (see Figure 5.1 in Chapter 5). Models were formed using methods detailed in Section 5.2.2.

During the DMS models period, the subject was visually cued to make two small changes in position of the head for each type of movement (yaw, pitch and z-translation) before returning to the initial position. Data were used to form models according to the methods detailed in Section 6.4.

During the experimental period the subject was instructed to move both feet via plantar/dorsal ankle flexion for 5 s and then keep still for 39 s (total of 7 movements within the experimental period). The foot movements were performed to simulate

changes in the position of a subject's head as might occur during a typical EEG-fMRI study with a longer duration.

For comparison, the experimental data were corrected using the three different methods (AAS, AAS-DMS and GMF-AAS). First, the data were corrected using AAS (template formed over all slice acquisitions during the experimental period) in Brain Vision Analyzer 2.0. Second, the DMS models were fitted to, and subtracted from, each slice of AAS corrected GA using a custom, regularised least-squares method (see Chapter 6). Thirdly, the GMF models were fitted and subtracted from each slice of GA in the raw EEG data using a custom, regularised least-squares method (see Chapter 5) before being corrected using AAS (template formed over all slices during experimental period) in Brain Vision Analyzer 2.0.

The EEG signals pre- and post-correction using the different methods were Fourier transformed and the average magnitude at each slice harmonic (10 Hz fundamental frequency) over a bandwidth of 0.4 Hz was found. The attenuations of the GA using each correction method relative to raw, uncorrected data were then calculated. Changes in head position were calculated from the fMRI data using SPM8.

7.3   Results and Discussion

For all three recordings, the head translations did not exceed 2 mm along the x-, y- or z-axes and head rotations did not exceed 1° around any of the three axes. However, as seen in the results reported in Chapters 5 and 6, these movements produced significant changes in the shape of the GA. These changes in the GA are consistent with a linear variation of the different GA components with position and orientation, as predicted by theory [95, 94].

As expected, the change in shape of the GA, due to the movement, causes the AAS correction to perform poorly. However, the residuals after AAS are well characterised by the difference models thus allowing their removal by DMS. Consequently, DMS performs well at removing residual GAs throughout the data acquisition. Similarly the GA component models were also able to characterise

the GA at all the different positions, allowing the combination of GMF-AAS to correct the GA. Consistent with the results of Chapter 5, GMF reduced the variability of the GA across slices allowing the residual artefacts to be removed with AAS.

Figure 7.2 shows the attenuation of the GA at every 3rd harmonic of the fundamental slice frequency (10Hz) produced by using AAS, AAS-DMS or GMF-AAS averaged across all three data sets before averaging across channels. The significance of differences between the performances of AAS-DMS and GMF-AAS across channels at each harmonic were evaluated using a wilcoxon signed rank test. An improvement in the attenuation of harmonic components of the GA can be seen for both AAS-DMS and GMF-AAS compared with AAS alone across the majority of harmonics. However, from the attenuations it appears that the combination of GMF-AAS significantly outperforms DMS across most harmonics. This suggests that GMF-AAS is able to better account for the changes in GA due to typical subject movements. It is unclear why GMF-AAS appears to outperform DMS, however, it is possible that the basis set of head movements does not account for all of the variation in the GA due to any small subject head movement. Further experimentation would be required to assess the particular differences between the two methods.
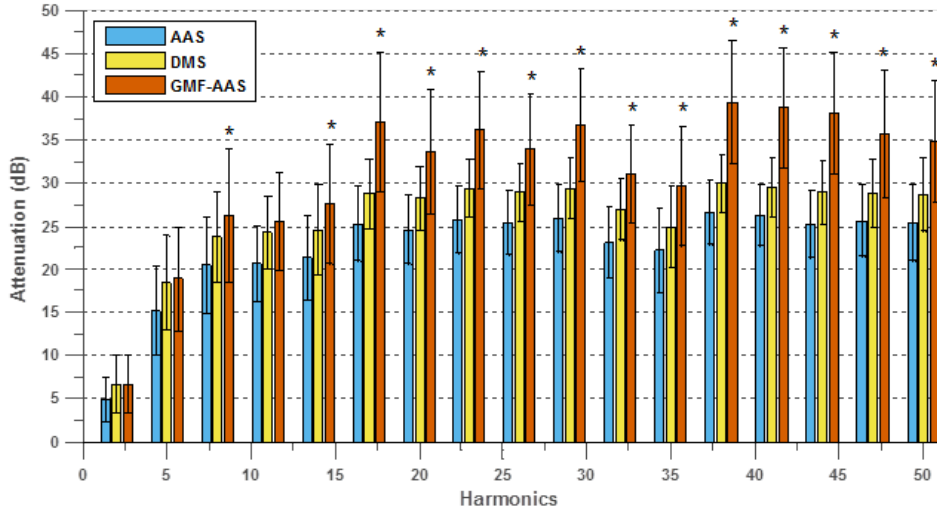
Figure 7.2: Average attenuation of signal power over all channels when using AAS alone and when combined with DMS and GMF. For convenience, only the attenuations of every third harmonic of the fundamental frequency (10 Hz) are plotted. Error bars indicate the standard deviations across all channels and stars indicate significant difference (p<0.05) in performance between AAS-DMS and GMF-AAS.

7.4 Conclusion

In agreement with previous work (Chapters 5 and 6), both the GMF-AAS and AAS-DMS methods offer advantages over the use of AAS alone in correction of the GA in the presence of subject movement. It appears that the GMF-AAS method offers a better performance in GA correction than the AAS-DMS method. From the preliminary work, it is unclear why the GMF-AAS method outperforms AAS-DMS and further experimentation is required to investigate the difference in performance. On the other hand, the AAS-DMS method is far easier to implement than the GMF method, since DMS requires no additional pulse programming. Therefore, both methods are still relevant to simultaneous EEG-fMRI experiments involving subject groups, such as children, where significant movement during recordings may occur.

Chapter 8

Using the GMF Method with 3D-EPI

8.1 Introduction

Three-Dimensional (3D) EPI pulse sequences can offer significant improvements in signal-to-noise over two-dimensional (2D) EPI sequences when scanning large numbers of slices [20]. To create a 3D-EPI sequence, the 2D-EPI sequence described in Chapter 2 can be modified according to Figure 8.1. A low amplitude gradient is applied during RF excitation to excite a large volume. After this, phase-encoding gradients are applied along the slice direction prior to the application of a standard 2D-EPI readout sequence. The sequence is then repeated for different amplitudes of the phase-encoding gradient along the slice direction.

As a result of the signal-to-noise advantage, there is an interest in using 3D-EPI rather than 2D-EPI for acquiring high-resolution fMRI data at 3 T [135] and higher field strengths. However, 3D-EPI can be problematic for simultaneous EEG-fMRI experiments. The additional phase-encoding gradient pulses in 3D-EPI cause the waveform of the GA to vary over successive TR periods. It is therefore, difficult to correct the GA using standard methods such as AAS. However, it is possible that GMF methods could be used to correct such a GA, provided that an appropriate
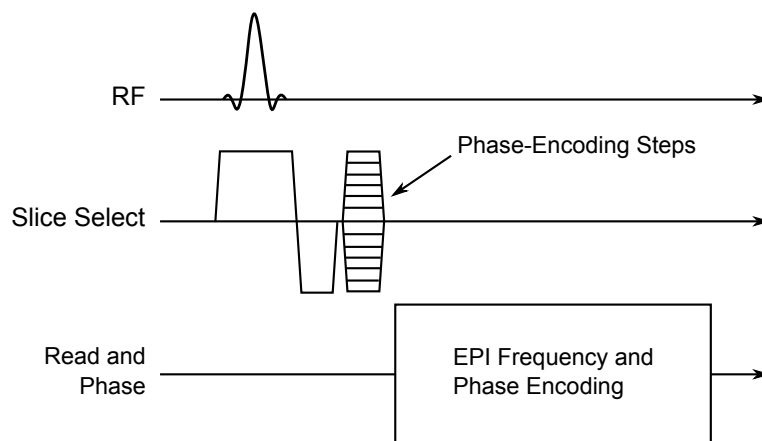
Figure 8.1: Schematic of the modifications made to the slice channel of a 2D-EPI sequence to produce a 3D-EPI sequence, based on diagram from "EPI and Functional MRI" [134].

model for the GA component, due to the additional phase-encoding gradients, can be generated. The following preliminary experiment was performed to see if this was feasible.

8.2   Methods

The 32-Channel EEG system (BrainAmp MRplus, Brain Products GmbH, $5\,kHz$ sampling rate, $250\,Hz$ low-pass filter, with MR and EEG clocks synchronised) was attached to a spherical conducting agar phantom. This was placed inside a Philips $3\,T$ Acheiva scanner. Three simultaneous recordings were acquired using a customised 3D-EPI pulse sequence (26 phase-encode steps, TR $=100\,ms$ per phase-encode step, TE $=35\,ms$, $36 \times 36 \times 20$ matrix, $3\,mm^3$). The sequence modifications were the same that were used in Chapter 5 where the channels of the imaging sequence were selectively nulled in an early preparatory stage in order to collect data for forming the GMF models (see Figure 8.2). Unfortunately, with the current, in-house modifications to the MRI scanner software we were unable to null the additional phase-encoding gradients applied in the slice select direction. However, it was possible to null all other gradients. This meant that each of the models for the slice, phase, measure and RF components also contained
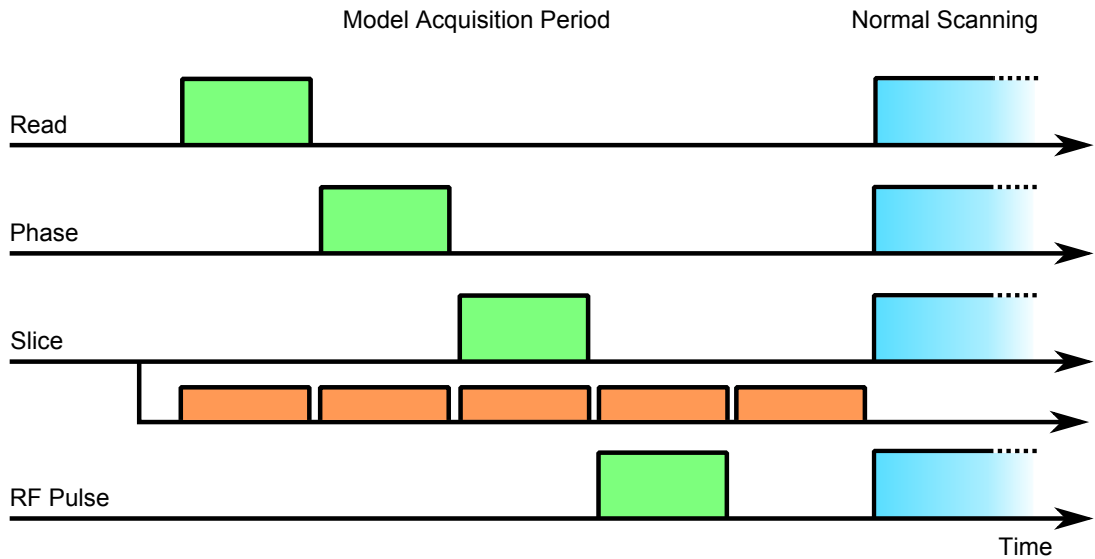
Figure 8.2: A diagram of the custom pulse sequence used to acquire the data for forming the models for the 3D-GMF method. Channels of the MRI sequence are nulled in sequential blocks of 6 volumes (shown in green) of EPI data to effectively isolate the induced artefact components on the EEG recordings prior to an EEG-fMRI experiment (shown in blue). The orange blocks represent the phase-encoding along the slice direction. With the current, in-house modifications to the MRI scanner software it was not possible to null the phase-encoding along the slice select direction. However, it was possible to null all other gradient components. This means that the data recorded for forming each component of the GA is contaminated by the GA due to the phase-encoding gradients applied along the slice direction. However, since the GA is comprised of a linear combination of these GA components, these contaminating features can be regressed out in the fitting process.

components due to the phase-encoding along the slice direction. However, because the GA is a linear combination of GAs induced by the separate components of the MRI sequence, by recording an additional model just containing the GA due to the phase-encoding along the slice select direction, any contaminating components in the other models could be regressed out in the fitting and subtracting process used in the GMF method.

8.3 Analysis

Data from all slice acquisitions within each block of 6 volumes for each model are averaged together to form the five models for each individual EEG channel. These are then baseline corrected by subtracting the temporal mean over the entire slice and a weighted average across EEG channels calculated using the peak absolute value (including the sign) of each channel as the weights. This process formed the final single model of the GA from each of the MR components (slice volume excitation, slice phase encoding, read, phase and RF) which was used to fit to the rest of the 3D-EPI data collected during the same acquisition.

Fitting was achieved using the custom, regularized, least-squares fit developed in Chapter 5. After fitting and subtracting, AAS was applied using Brain Vision Analyzer2 (BrainProducts GmbH). For comparison, AAS was also performed on the raw uncorrected EEG data.

As used in previous in previous analyses in this thesis, the EEG signals pre- and post-correction using the different methods were Fourier transformed and the average magnitude at each slice harmonic (10 Hz fundamental frequency) over a bandwidth of 0.4 Hz was found. The attenuation of the GA using each correction method relative to raw, uncorrected data were then calculated.

8.4 Results and Discussion

Figure 8.3 shows the 26 separate GA components induced by each of the different amplitudes of the phase-encode gradient applied along the slice direction for a single electrode. The 26 separate GA components were determined by averaging each acquisition over the 6 volumes of model data. A GMF model of the GA component due to the phase-encoding along the slice direction averaged over channels can be seen in Figure 8.4. To test the linearity, the GMF model of the phase-encoding along the slice direction (Figure 8.4) was fitted to the different phase-encode amplitudes shown in Figure 8.3. These coefficients were then used
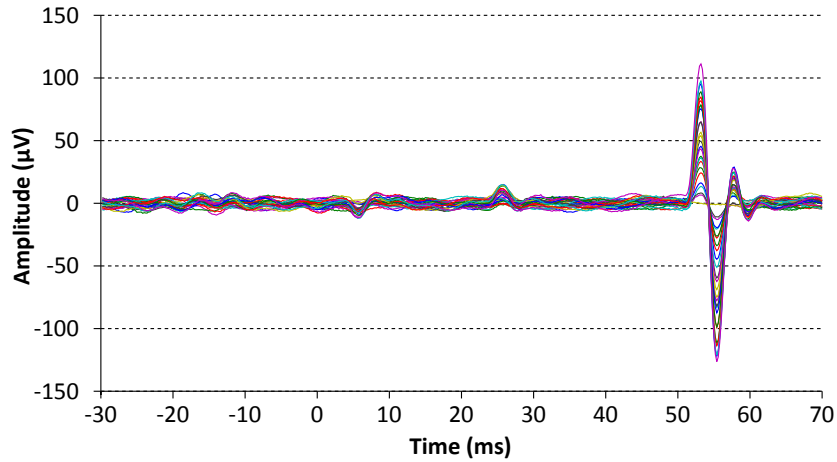
Figure 8.3: In 3D-EPI an additional phase-encode gradient is applied along the slice direction with varying amplitudes across successive acquisitions. Shown are the GA components induced by this amplitude varying phase-encode gradient ($\sim$5 ms and $\sim$25 ms relative to the EEG slice marker at 0 ms) and associated spoiler gradient ($\sim$55 ms) on the EEG channel at electrode location P3. These components were formed by averaging across 6 volumes where the other components of the pulse sequence had been nulled and then segmenting into the 26 successive acquisitions. Note that half of the components have been multiplied by -1 to match the sign of all components for ease of comparison.

in a linear-fit to show that the weights scale linearly with phase-encode number (see Figure 8.5). These results indicate that the GA component due to the phase-encoding along the slice direction scales as expected over successive acquisitions. This implies that a model for this GA component can be formed and used within the GMF method to fit and subtract the GA due to a 3D-EPI sequence.

Figure 8.6 shows a single TR-period of GA corrected using AAS and 3D-GMF-AAS for a single channel. It is clear that AAS is unable to account for the GA due to the varying phase-encode gradient applied along the slice direction. On the other hand, the 3D-GMF-AAS is able to track effectively the variation in amplitude of this GA component and show a large attenuation of overall GA due to a 3D-EPI sequence.

Figure 8.7 shows the attenuations of harmonics of the fundamental frequency (10 Hz) of the GA due to both AAS and 3D-GMF-AAS. The attenuation values
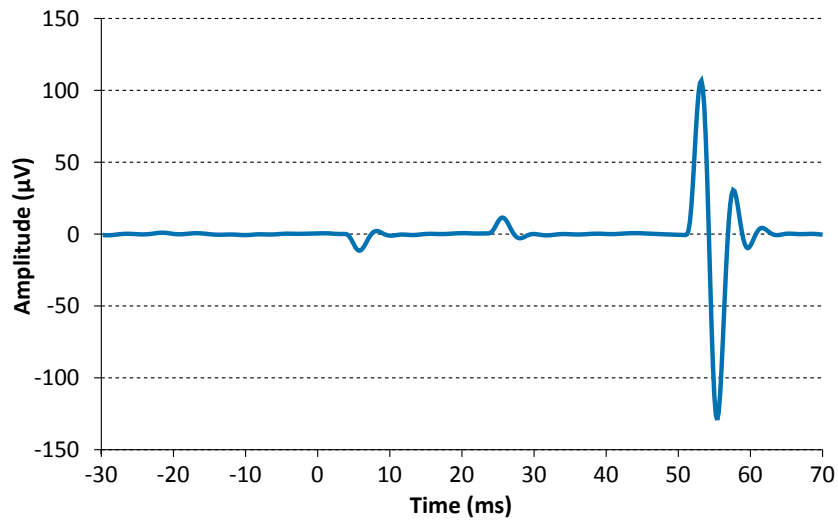
Figure 8.4: 3D-GMF Model of the GA component due to the phase-encoding along the slice direction. The model was averaged across all slice-encoding acquisitions within the 6 volumes of model data and averaged, using weights corresponding to the peak artefact value, across channels.

Fit Parameters
Gradient = 0.0770 ± 0.0003
Intercept = -1.080 ± 0.004
R^2 = 0.9998
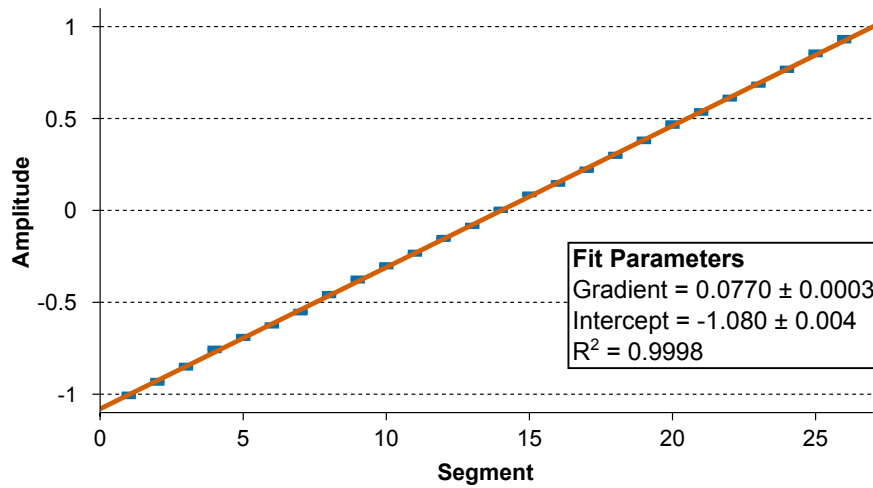
Figure 8.5: Plot showing the linear scaling of the phase-encoding steps. A set of coefficients were calculated by fitting (least-squares) the 3D-GMF Model shown in Figure 8.4 to each of the 26 phase-encode steps recorded on electrode P3 (see Figure 8.3). These coefficients were then plotted according to phase-encode number (blue) with error bars corresponding to the error on the calculated coefficients. A line-of-best-fit (orange) shows that, as expected, the GA scales linearly across the phase-encoding steps.
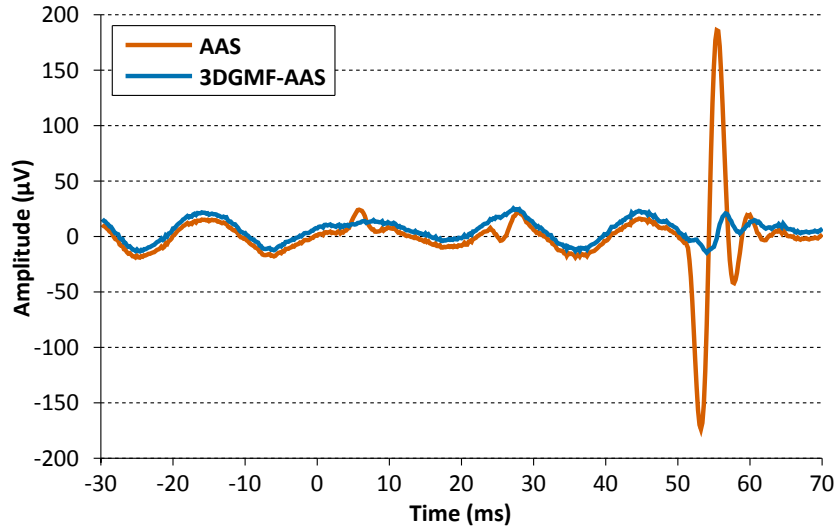
Figure 8.6: A single TR-period of EEG corrected using AAS (blue) and 3DGMF-AAS (orange) for data recorded on electrode Fp2.

suggest that 3D-GMF-AAS outperforms AAS in correcting the GA induced on a phantom by a 3D-EPI sequence. In order to assess significance, more data-sets would be required. Moreover, it would be useful to perform this experiment on a group of healthy human subjects.

The results also suggest that any residual GA due to the phase-encoding contaminated models for the read, phase, slice (volume excitation) and RF pulses is adequately accounted for by the model for the GA due to the phase-encoding gradient applied along the slice direction. While it is not ideal for the regular GMF models to be contaminated by the phase-encoding GA, the results do indicate that 3D-EPI based simultaneous EEG-fMRI recordings with GA correction on a slice basis rather than volume basis are made possible by the GMF method.
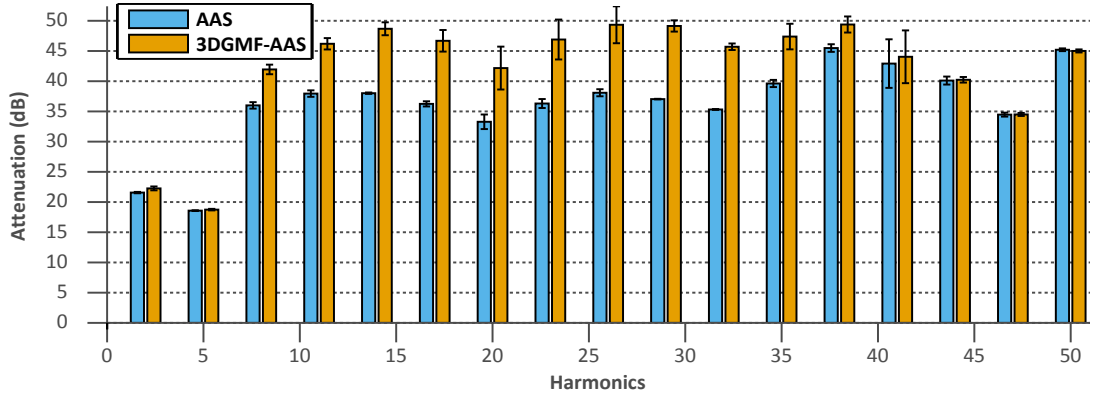
Figure 8.7: Average attenuation of signal power over all channels when using AAS alone or 3D-GMF-AAS. For convenience, the attenuations of every third harmonic of the fundamental frequency (10 Hz) are shown. Error bars show the standard deviation across the three data sets.

8.5 Conclusion

In conclusion, the phantom work suggests that the GA due to a 3D-EPI sequence can be corrected using a modified GMF method. To the best of my knowledge, this is the first example of a correction method which can attenuate the GA due to a 3D-EPI sequence on a slice rather than volume basis. This is therefore relevant to anyone wishing to push the boundaries of simultaneous EEG-fMRI experiments by involving 3D-EPI. However, more work is required to explore fully this potential avenue. Further, in-house modifications to the MRI scanner software are required such that the phase-encoding gradient along the slice direction can be separately nulled. This would prevent the regular GMF models from being contaminated by additional varying GA components. Also, recordings on a group of healthy human volunteers would also help to assess and confirm the efficacy of this method in correcting the GA induced by a 3D-EPI sequence.

Part III

Conclusions

Chapter 9

Discussion

9.1 Summary

The overall aim of the work presented in this thesis was to improve the quality of EEG recordings made in simultaneous EEG-fMRI experiments. The primary focus was on developing methods for correcting the GA in the presence of head movement without the need for additional hardware.

The GA was described in detail in Chapter 4 along with reviews of the many other challenges associated with simultaneous EEG-fMRI. Various GA correction methods were reviewed, but all struggle to correct the GA adequately when the position of the subject's head changes during the recording process. Based on theory and modelling work, completed by others [95, 94], it is reasonable to assume that the GA is comprised of a linear combination of artefacts induced by the changing magnetic fields associated with the separate components of the MR Imaging sequence. Moreover, based on the work of Yan *et al.* [94], a further assumption can be made. It is possible to assume that the weightings of the relative contributions of each of the component artefacts should vary linearly with respect to small variations in subject position. Based on these assumptions of linearity, two novel GA correction methods were developed. These are termed GMF (see Chapter 5) and DMS (see Chapter 6).

The GMF method is based upon generating models of the underlying GA components which are then adaptively fitted and subtracted from slice acquisitions of the GA. The models were generated in two separate ways. The first required the data for forming the models to be recorded within the same MRI scan as the experimental data. The second allowed higher temporal-resolution versions of the models to be recorded in a separate scan. These high-temporal-resolution models could then be temporally aligned with the experimental data before down-sampling, fitting and subtracting. No significant difference in performance was observed between the results produced using the two types of models and therefore preference is left to the experimenter. Experiments were conducted on both a conductive phantom and three human subjects with controlled changes in head position to simulate the movements which might occur during a typical fMRI experiment. The GMF methods were performed and compared to AAS. Overall the combination of GMF-AAS proved to be best, showing a significant reduction in the GA compared with using either AAS or GMF alone.

Based on the spatial form of the GA, it was assumed that small changes in position would produce linear changes in the GA. This was largely confirmed in the preliminary phantom work detailed in Chapter 6, however further work is required to confirm this definitively and to determine what size of movement causes this linearity to break-down.

The DMS method involved estimating the residual GA remaining after AAS by modelling the changes in GA using a basis set of artefact templates corresponding to the most likely head movements. This involved asking the subject to make controlled axial head translations and rotations about the x- and z-axes and then calculating the changes in GA produced by the different movements. These models were effective at characterising the change in GA due to typical head movements and showed a significant improvement in the attenuation of the GA over using AAS alone.

In Chapter 7 some preliminary results comparing the GMF and DMS methods were shown. The work indicated that the GMF-AAS method produced a better

attenuation of the GA than the AAS-DMS method.

Finally Chapter 8 shows preliminary work where the GMF method is used to correct the GA due to a 3DEPI sequence. To the best of my knowledge, this is the first correction method that has been able to account for the variation in the waveform of the GA due to the additional gradients used in 3D-MRI sequences on a slice by slice basis.

9.2   Comparison of GA Correction Methods

A selection of different methods for correcting the GA have previously been reviewed in this thesis (Chapter 4). However, to date, the (HTR)GMF and DMS methods presented here have only been compared to AAS as implemented by Brain Vision Analyzer 2.0 and each other. This section aims to compare some of the known strengths and limitations of the various correction methods that have previously been described to the two methods presented within this thesis.

Ritter *et al.* [136] highlighted that there is not a consistent, standardised method for evaluating the performances of the various GA correction methods available. This makes it difficult for people to judge which of the available methods would be more suitable for them to use for their particular application. To enable a better comparison of the methods, it may be possible to construct a theoretical framework within which comparisons can be properly interpreted. This framework should be based on a good understanding of how the GA is produced in the EEG system. The theoretical descriptions of the GA presented in Chapters 4, 5 and 6 could be used to build such a framework.

Perhaps the most similar technique for correcting the GA to the (HTR)GMF method, is the approach described by Felblinger *et al.* [95]. Both methods seek to model the underlying components of the GA, however, the methods of generating the individual models differ. With a slight adjustment, it might be possible to adapt the method proposed by Felblinger *et al.* [95] so that the modelled components scale to fit successive instances of the GA, much like the (HTR)GMF

methods. The advantage of the approach by Felblinger *et al.* [95] is that, provided the impulse response function can be adequately characterised, the sequence of gradients applied by the MRI scanner could change across the scan period. This could lead to more complex MRI sequences being used in simultaneous EEG-fMRI measurements. However, this method has only been shown to be effective for recovering ECG signals. EEG signals recorded simultaneously with fMRI typically have a much lower SNR than ECG signals and therefore, the effectiveness of using the impulse response to generate the models is yet to be assessed. It may be that the difference between the typical amplitudes of the EEG signal of interest and GA is too great for the EEG to be recovered using the method described by Felblinger *et al.* [95].

Template subtraction methods, such as the AAS method proposed by Allen *et al.* [2], have generally proved to be the most effective overall at attenuating the GA [136]. Signal averaging (as used in AAS) is effective at estimating the overall GA, provided that the relative contributions of the underlying GA components do not change. Unfortunately, as shown in Chapter 5, this condition is compromised when the subject changes position during the recording. Therefore, from the theoretical work, it seems reasonable that the (HTR)GMF methods should provide a better performance, as they characterise the components of the GA due to the separate parts of the MRI sequence. This means that the (HTR)GMF models provide a more general description of the GA, which can be adapted to specific instances of GA. Whereas, the AAS template, though very effective when the subject is stationary, is inflexible in describing the GA. It is interesting to note, though, that the combination of (HTR)GMF and AAS out performs either method used in isolation (see Chapter 5). This suggests that there are aspects of the combined GA that are not captured by the (HTR)GMF models. It is reasoned that this might be due to differences in the scanner vibration between the separate application of components of the imaging sequence and the combined application. However, the exact cause of the subtle differences between the instances of GA estimated by (HTR)GMF and AAS require further investigation.

Over the years various extensions have been made to AAS to improve the efficacy of the technique when dealing with EEG data corrupted by subject movement [124, 118, 119]. Some advantages of these methods over (HTR)GMF and DMS are that they do not require considerable, expert customisation of the MRI scanner software nor do they require the careful cooperation of subjects to implement. Additionally these methods do not require additional scanner time. Unfortunately, these methods only work in ideal cases of limited subject movement, whereas (HTR)GMF and DMS should be able to cope with a wider variety and frequency of subject movements.

The FASTR method proposed by Niazy *et al.* [120] extends the AAS method by using temporal PCA to define an optimal basis set for regressing out any residual GA. The original aim of the PCA based method is to characterise slight variations in the morphology of the GA across successive slices due to the asynchronous EEG and MRI clock signals. It seems reasonable that the FASTR method should be able to capture some small changes in the GA due to slight subject movement. However, it is important to note that Niazy *et al.* [120] do suggest that the method is compromised by significant head movement. In principle, the FASTR method seems to be similar to AAS-DMS; since DMS seeks to capture the temporal variation of the GA with respect to orthogonal movements. It may be that both methods are doing a similar job, but by using different approaches; one statistically driven, the other model based. Further work would be need to assess this idea. For example, it should be possible to compare the temporal characteristics and the spatial morphology across the scalp of the principle components from FASTR and the DMS models.

9.3 Limitations and Considerations

There a number of possible limitations and considerations concerning the work presented in this thesis. For example, the choice of regularization parameter used in the fitting algorithm (Equation 5.22) was chosen manually as the best value

for visually attenuating the GA. The choice of parameter could be improved using simulations. GA could be simulated using the GMF models for a variety of different scaling parameters. EEG data, recorded inside the scanner without an image sequence being applied could then be added to the simulated GA. The fit algorithm could then be used to recover recorded EEG data and a statistical measure, such as the correlation between the original EEG data and the simulated GA corrected EEG or the root-mean-square difference between the actual scaling parameters and the estimated fit parameters, could then be numerically optimised to determine the best choice of regularization parameter.

Another potential limitation of the methodology used here is the statistical analysis used to assess whether there is a significant difference between the harmonic attenuations of the various GA correction methods. In this analysis there is a mixture of within-subject and between-subject variance. The analytical expressions derived by Yan *et al.* [94] suggested that the dominant contribution of the GA were from the wire leads and not the from the difference in scalar potential induced upon the scalp. This meant that I did not expect any significant differences in the GA and consequently it's removal between individual subjects. However, a variations in the performance of the GA correction methods do depend upon the size, types and frequencies of movements made by subjects during the experiments. This means that there may be some differences in variance of the performance of the GA correction methods within and between subjects if the types and sizes of movements vary considerably between subjects and not within subjects. This may have more of an effect on the performance of the DMS method as it is theoretically only valid for small positional changes. The performance of the GMF methods should theoretically not be effected by the size of the movements as the GA should always be a linear summation of the individual artefact components. This is corroborated experimentally by using models of the artefact components formed as an average across all channels to remove the GA. However, it is important to note that any large movements will have a substantial effect on the fMRI data, which may be discarded anyway.

A point to consider regarding both the GMF and DMS methods presented here is that their effect upon the neuronal signals of interest is largely unknown. However, both the GMF and DMS methods are based upon replicating the shape of the GA, therefore, provided that the GMF and DMS models have no explanatory power over the shape of the neuronal data of interest, the methods should have no effect on the fidelity of the recovered neuronal data. The majority of the models produced from the data presented in this thesis (see Figures 5.2 and 6.13) form complex waveforms which bear no resemblance to known neuronal signals. Therefore it is not likely that the models would fit and subtract neuronal data. It may be possible that the models describing much simpler waveforms could possess some similarity with neuronal data and consequently affect recovery of such data. For example, the GMF model for the GA due to an RF pulse presented in this work (Figure 5.2, inset) has a simple, short, pulse-like waveform. It is therefore reasonable to believe that if some component of the neuronal activity has a similar shape to the RF model, then the neuronal data may be attenuated. However, this would require the pulse-like neuronal signal to perfectly align with the time-point of RF excitation, which is highly unlikely. A specific limitation of AAS, regarding neuronal data, is that the timings of evoked-potentials cannot be an integer multiple or factor of the period of the AAS template. Otherwise the neuronal responses will be coherently combined to form the AAS template and consequently the periodic neuronal data will be filtered out in the subtraction process. However, the GMF methods are based on replicating the shape of the GA rather than attenuating periodic data Therefore, provided that there is no explicit stimulus present in the period for collecting data to form the models, (HTR)GMF does not possess this limitation on stimulus timings. It is important to note that combined (HTR)GMF-AAS, as recommended by this thesis, will suffer from the limitation on stimulus timing.

As shown earlier in Chapter 4, the AAS method can be viewed as involving the application of a set of notch filters at harmonics of the fundamental GA frequency. This allows AAS to be used for real-time correction of the GA. Similarly, it should be possible to adjust the fitting algorithm for the GMF and DMS methods to

also allow for real-time correction of the GA. Instead of using normal equations as the solution for the fit parameters, an iterative method such as gradient descent could be used. This would possibly require some refinements to be made to the model-forming processes, so that they could be calculated quickly, but provided that the models are successfully formed, it does not seem unreasonable that both the GMF and DMS methods could be adapted for real-time artefact correction.

There may be circumstances where one method is preferable over the other. The GMF methods require considerable, expert customisation of the MRI scanner software to be able to selectively null the applied gradients. On the other hand DMS requires no such customisation. The DMS method can add a considerable amount of time onto the experiment if multiple recordings are required, whereas, using the HTRGMF method requires one additional short duration recording in order to collect data for forming the models. Also, DMS requires a level of cooperation from the subject when following the instructions during the period for collecting the data to form the models, whereas GMF simply requires the subject to keep as still as possible for the model data collection period.

9.4   Applications

Simultaneous EEG-fMRI measurements offer unique advantages over the isolated use of each modality in the investigation of spontaneous brain activity. Both the GMF and DMS methods are relevant to simultaneous EEG-fMRI experiments where subject movement is likely to occur, such as in studies involving patients or children. Further to this, both methods showed significant reduction in the GA in the high-frequency bands. Therefore, these novel correction methods may also be useful for investigating high-frequency neuronal activity. Here I provide a short overview and discussion of the potential applications of simultaneous EEG-fMRI measurements and the methods developed in this thesis for the correction of the GA.

9.4.1 Epilepsy

The idea of simultaneous acquisition of EEG and fMRI data was originally conceived and driven by the desire of epileptologists to localize the sources of epileptic seizures within the brains of their patients [71, 137]. However, since the very first simultaneous recordings of epileptic activity were made [88, 138]; many methodological developments have been made to improve the quality of the data acquired (see Chapters 4, 5 and 6). Nowadays, the main concerns of simultaneous EEG-fMRI in adults with epilepsy are improving the current understanding of the generators of epileptic activity and to improve the surgical treatment of the disease.

In a number of cases, EEG-fMRI measurements have been successful in identifying regions of BOLD response, correlated with interictal epileptic discharges (IEDs) [139, 140, 141]. The likelihood of a significant fMRI signal change depends upon, the number of IEDs, morphology, ease of classification of the IEDs and the temporal spread [142, 143, 144]. The successful classification of IEDs is dependent upon the noise present within the data. Therefore, reliable and robust methods for removing noise such as the GA are important to the efficacy of such simultaneous measurements.

While interictal EEG-fMRI measurements have been able to identify regions correlated with IEDs, these regions may not correspond to epileptogenic zones [75, 137, 145]. Therefore the relevance of EEG-fMRI measurements of IEDs to presurgical evaluations is still unknown.

High-frequency oscillations (100-500 Hz) have been more closely linked with seizure onset zones than spiking activity. These have typically been observed using implanted electrodes [146, 147, 148], however some EEG studies have suggested that these oscillations can be measured at the scalp [149, 150]. As previously mentioned, current GA correction methods are inadequate at attenuating the GA at frequencies greater than 80 Hz. This would mean that simultaneous EEG-fMRI investigations into high-frequency oscillations as a biomarker for the seizure onset zones would be impossible. However, the work presented in this thesis, suggests

that the (HTR)GMF (Chapter 5) and DMS (Chapter 6) methods show a significantly improved attenuation of the GA above 80 Hz over current GA correction methods. If the methods presented here are successful at recovering high-frequency oscillations from the GA-corrupted EEG data and if it is possible to link the oscillations to some feature of the BOLD response, it may be possible to develop a technique for non-invasively identifying the seizure onset zones for surgical treatment. Further work is required to evaluate this possibility.

Studies of ictal activity have a number of practical difficulties [75]. Instances of ictal activity can be infrequent and difficult to predict therefore the chance of a patient experiencing a seizure during an EEG-fMRI is small. It is also ethically dubious to induce ictal responses in patients and in some cases the seizures can be dangerous for the patients. Another problem with ictal activity is that in many cases it is accompanied by head movement. Therefore, GA correction methods that are robust to subject head movement, such as the (HTR)GMF and DMS methods presented here (Chapters 5 and 6), are potentially important to the study of such activity, provided that the fMRI data can be recovered and the movement artefact can be removed from the EEG data.

Simultaneous EEG-fMRI potentially offers unique insights into the understanding of epilepsy as it is able to capture and compare the electropathology with the haemodynamics. For example, in the last ten years there has been an increased interest in the idea that epileptic activity may not result from a single seizure onset zone, but instead is better linked to the abnormal function of a network. For a recent review of this idea see the paper by Pittau *et al.* [151]. Simultaneous EEG-fMRI results have shown that focal electropathology can elicit multifocal BOLD responses potentially corroborating the idea of an "epileptic network". However, further work is needed to assess to potential clinical and neuroscientific utility of network based analyses of epilepsy. Moreover, a recent review [152] suggests that there is a gap in the literature regarding the links between the abnormal connectivity measures in fMRI and the electropathological phenomena associated with epilepsy. Simultaneous EEG-fMRI could potentially and uniquely allow re-

searchers to link certain network abnormalities with associated transient IEDs, thus furthering the understanding of the disease.

As previously mentioned, it maybe possible to adapt the (HTR)GMF and DMS methods presented in this thesis for real-time GA correction. This would therefore allow clinicians to monitor the epileptic activity of a patient in real-time which, could potentially have implications for improving patient safety during EEG-fMRI studies.

9.4.2 Resting-State Measurements

Resting-state experiments involve the evaluation of functional interactions within the brain in the absence of an explicit stimulus. At first this type of approach may seem counter-intuitive as there is no explicit functional task to control the results. However, resting-state analyses allow experimenters to draw links between different dynamic aspects of the measured data. In fMRI, resting-state measurements have been used to evaluate interactions between distinct regions of the brain [153].

EEG measurements acquired simultaneously offer a unique opportunity to further interpret the resting-state fMRI data [137]. For example, a number of studies have been used to correlate oscillatory brain signal fluctuations with variations in the BOLD activity [76, 80, 154, 155]. These types of studies have predominantly been limited to theta, alpha, beta and low gamma frequency bands. This is primarily because, higher frequency oscillatory activity is technically difficult to acquire with simultaneous EEG-fMRI measurements. As noted in earlier chapters, standard GA correction methods do not work well above approximately 80 Hz. Combined fMRI and intracranial EEG recordings in both animal [39, 156, 157] and human subjects [158, 159, 160] have shown much stronger correlations between activity in the high gamma-frequency band and the BOLD response than with activity in other frequency bands. Both the (HTR)GMF and DMS methods have shown greater attenuation of the GA in the high-frequency bands than AAS. Therefore, the methods presented within this thesis may help to further develop any investigations into the links between high-frequency scalp EEG measurements

and the BOLD response.

EEG measurements acquired simultaneously with fMRI can also be used to uniquely link the dynamics of resting functional connectivity measurements with distinct electrophysiological features within the EEG. For example, measures of vigilance on the EEG can be used as a "pseudo-paradigm" to explore the variability across time of the fMRI data [79, 80, 71, 161]. Combined measurements have also been used to link electrophysiological features of pathologies such as epilepsy [152] to variations in resting-state connectivity. Both the (HTR)GMF and DMS methods developed within this thesis offer an increased spectral bandwidth. It may therefore be possible that these methods could uncover additional high-frequency EEG features that would aid in the interpretation of the fMRI data. Moreover, some of these experiments may require long recording-times which, in turn, lead to increased subject discomfort and therefore an increased likelihood of subject movement occurring during the experiment. Both methods presented within this thesis are robust to subject movement and could therefore be used to recover EEG data corrupted by subject position changes.

9.4.3 Trial-by-Trial Analysis

Laufs *et al.* [137] have stated that investigations into trial-by-trial variability of the results suggest that non-reproducible effects can have a significant effect upon the results presented by individual trials. This means that specific, individual-trial-related responses can potentially provide predictive information regarding the BOLD response [162]. For example, Eichele *et al.* [81] used a parametric approach where the predictability of an auditory odd-ball task was varied across trials. Resultant modulations in the amplitude of event-related-potentials were shown to be useful in predicting spatio-temporal fMRI patterns. Also, Debener *et al.* [163] showed that variations in the amplitude of the error-related negativity of the EEG signal between trials was able to predict fMRI activity within the rostral cingulate zone. Mullinger *et al.* [164] used the trial-by-trial variability of the poststimulus response to median nerve stimulation to show that the amplitude and

172

directionality of the poststimulus BOLD response depends upon the synchrony of the neuronal activity within the 8-13 Hz frequency band. This study by Mullinger *et al.* [164] substantially extends the understanding of the origin of the BOLD signal. As previously mentioned, high-frequency neuronal activity has been shown to be more strongly correlated with the BOLD signal [39, 156, 157, 158, 159, 160]. Therefore, it would be interesting to see if any trial-by-trial variability in the high-frequency neuronal activity recovered using either the (HTR)GMF or DMS methods would be useful in interpreting variations in the BOLD response.

9.5 Future Work

Whilst both the GMF and DMS methods, developed in this thesis, have proved successful in eliminating the GA — particularly in EEG-fMRI experiments where subject movement is likely to occur — there is still more work to be done. In this section a couple of possible future projects are presented.

9.5.1 Applying Correction Methods to a Real Experiment

The next step would be to use the (HTR)GMF and DMS methods in a real functional experiment. This would be useful for two reasons. First, it would be important to determine whether either of the methods presented in this thesis have any effect upon the underlying brain signals of interest. Second, it would be interesting to explore whether the new GA correction methods would add any value to the field beyond the correction methods currently available.

In order to tackle the first question, it would be wise to perform a simple, well-known, reproducible, functional task such as a simple eyes-open, eyes-closed experiment. Both comparisons between recordings acquired inside and outside the scanner and comparisons between the new methods and a standard method such as AAS could easily be used to determine whether the new correction methods have any effect upon the neuronal data.

To answer the second question, it would be best to use the (HTR)GMF and DMS methods to try to evaluate EEG data in frequency bands above those that can readily be recovered using methods such as AAS (i.e. $>80\,\mathrm{Hz}$). Perhaps, the simplest type of experiment to start with would be to look at resting-state data and try to correlate high-gamma-frequency power with the simultaneously acquired BOLD signal.

9.5.2 Development and Release of Analysis Software

EEGLAB [165] is an open source MATLAB toolbox for processing electrophysiological data. It has become increasingly popular for researchers to share their analysis software with the wider academic community via this toolbox to increase utility and the impact of new analysis software. Therefore, to this end the MATLAB functions for the GMF and DMS methods will be packaged and released as a plugin for this toolbox so that other researchers may benefit from the GA correction methods developed in this thesis. In order to do this, it is necessary develop a friendly, graphical user interface for the separate methods. It is also necessary to generalize the software so that it can be easily customized to suit any appropriate MRI sequence timings. It must also be rigorously tested and improved so that a robust piece of analysis software can be released. This testing will be done in collaboration with other users within the Sir Peter Mansfield Magnetic Resonance Centre (Nottingham) and from other labs such as the Institute of Mental Health (Nottingham) and the Birmingham University Imaging Centre (Birmingham).

Chapter 10

Conclusion

Simultaneous EEG-fMRI methods offer the experimentalists increased insights into the spontaneous, irreproducible function of the brain. The high-temporal resolution of EEG compliments the relatively long response times of the vascular system as measured in fMRI. Also the millimetre precision of fMRI makes up for the poor spatial resolution of EEG. While many advances have been made to improve the data quality provided by the simultaneous use of each modality, the GA recorded on the EEG can still be a significant problem for anyone wishing to investigate high frequency brain signals (gamma-band activity) or for experiments conducted on groups such as children or patients where subjects are likely to move during the experiment. The two methods (GMF and DMS) developed and presented in this thesis have been shown to outperform the current methods in correcting the GA in both the high frequency band and data-sets where subject movement has occurred. Additionally, preliminary work suggests that the GMF method could be easily adapted to correct the GA induced by a 3D-EPI sequence.

Bibliography

[1] S. Ogawa, T. Lee, A. Kay, and D. Tank, "Brain magnetic resonance imaging with contrast dependent on blood oxygenation," *Proc. Natl. Acad. Sci. USA*, vol. 87, no. 24, pp. 9868–9872, 1990.

[2] P. Allen, O. Josephs, and R. Turner, "A Method for Removing Imaging Artifact from Continuous EEG Recorded during Functional MRI," *NeuroImage*, vol. 12, no. 2, pp. 230–239, 2000.

[3] I. I. Rabi, J. R. Zacharias, S. Millman, and P. Kusch, "A New Method of Measuring Nuclear Magnetic Moment," *Phys. Rev.*, vol. 53, pp. 318–318, 1938.

[4] I. I. Rabi, S. Millman, P. Kusch, and J. R. Zacharias, "The Molecular Beam Resonance Method for Measuring Nuclear Magnetic Moments. The Magnetic Moments of 3Li6, 3Li7 and 9F19," *Phys. Rev.*, vol. 55, pp. 526–535, 1939.

[5] E. M. Purcell, H. C. Torrey, and R. V. Pound, "Resonance Absorption by Nuclear Magnetic Moments in a Solid," *Phys. Rev.*, vol. 69, pp. 37–38, Jan 1946.

[6] F. Bloch, "Nuclear Induction," *Phys. Rev.*, vol. 70, pp. 460–474, Oct 1946.

[7] P. C. Lauterbur, "Image Formation by Induced Local Interactions: Examples Employing Nuclear Magnetic Resonance," *Nature*, vol. 242, pp. 190–191, 1973.

[8] P. Mansfield and P. K. Grannell, "NMR 'diffraction' in solids?," *Journal of Physics C: Solid State Physics*, vol. 6, no. 22, p. L422, 1973.

[9] A. Garroway, P. Grannell, and P. Mansfield, "Image formation in NMR by a selective irradiative process," *Journal of Physics C: Solid State Physics*, vol. 7, no. 24, p. L457, 1974.

[10] A. Kumar, D. Welti, and R. R. Ernst, "NMR fourier zeugmatography," *Journal of Magnetic Resonance*, vol. 18, no. 1, pp. 69–83, 1975.

[11] S. Ogawa, T. Lee, A. Nayak, and P. Glynn, "Oxygenation-Sensitive Contrast in Magnetic Resonance Image of Rodent Brain at High Magnetic Fields," *Magnetic Resonance in Medicine*, vol. 14, no. 1, pp. 68–78, 1990.

[12] S. Ogawa and T. Lee, "Magnetic Resonance Imaging of Blood Vessels at High Fields: In Vivo and in Vitro measurements and Image Simulation," *Magnetic Resonance in Medicine*, vol. 16, no. 1, pp. 9–18, 1990.

[13] M. Goldman, *Quantum Description of High-Resolution NMR in Liquids.* Oxford University Press, 1st ed., 1988.

[14] P. Morris, *Nuclear Magnetic Resonance Imaging in Medicine and Biology.* Oxford University Press, 1st ed., 1986.

[15] D. W. McRobbie, E. Moore, M. Graves, and M. Prince, *MRI: From Picture to Proton.* Cambridge University Press, 2nd ed., 2007.

[16] J. Granwehr, "MPAGS MR1 Foundations of Magnetic Resonance." [Nottingham University Lecture Notes], 2010.

[17] B. Cowan, *Nuclear Magnetic Resonance and Relaxation.* Cambridge University Press, 1st ed., 1997.

[18] M. Levitt, *Spin Dynamics: Basics of Nuclear Magnetic Resonance.* Wiley, 2001.

[19] R. Bowtell, "MPAGS MR3 Advanced Topics in NMR." [Nottingham University Lecture Notes], 2011.

[20] S. Huettel, A. Song, and G. McCarthy, *Functional Magnetic Resonance Imaging.* Sinauer Associates, 2nd ed., 2009.

[21] M. Bernstein, K. King, and X. Zhou, *Handbook of MRI Pulse Sequences.* Elsevier Science, 2004.

[22] P. Mansfield, "Multi-planar image formation using nmr spin echoes," *Journal of Physics C: Solid State Physics*, vol. 10, no. 3, pp. L55–L58, 1977.

[23] R. M. S. Panchuelo, *High Resolution Anatomical and Functional Imaging.* PhD thesis, University of Nottingham, 2009.

[24] P. Glover and A. Howes, "MPAGS MR2 MR Hardware." [Nottingham University Lecture Notes], 2010.

[25] R. Buxton, *Introduction to Functional Magnetic Resonance Imaging: Principles and Techniques.* Cambridge University Press, 2nd ed., 2009.

[26] S. Kim and S. Ogawa, "Biophysical and physiological origins of blood oxygenation level-dependent fmri signals," *J Cereb Blood Flow Metab*, vol. 32, no. 7, pp. 1188–1206, 2012.

[27] K. Kwong, J. Belliveau, D. Chesler, I. Goldberg, R. Weisskoff, B. Poncelet, D. Kennedy, B. Hoppel, M. Cohen, and R. Turner, "Dynamic magnetic resonance imaging of human brain activity during primary sensory stimulation.," *Proceedings of the National Academy of Sciences*, vol. 89, no. 12, pp. 5675–5679, 1992.

[28] R. Sanchez-Panchuelo, S. Francis, R. Bowtell, and D. Schluppeck, "Mapping human somatosensory cortex in individual subjects with 7t functional mri," *Journal of Neurophysiology*, vol. 103, no. 5, pp. 2544–2556, 2010.

[29] G. Berns, J. Chappelow, M. Cekic, C. Zink, G. Pagnoni, and M. Martin-Skurski, "Neurobiological substrates of dread," *Science*, vol. 312, no. 5774, pp. 754–758, 2006.

[30] Y. Aghakhani, A. Bagshaw, C. BÃľnar, C. Hawco, F. Andermann, F. Dubeau, and J. Gotman, "fmri activation during spike and wave discharges in idiopathic generalized epilepsy," *Brain*, vol. 127, no. 5, pp. 1127–1144, 2004.

[31] A. Owen, M. Coleman, M. Boly, M. Davis, S. Laureys, and J. Pickard, "Detecting awareness in the vegetative state," *Science*, vol. 313, no. 5792, p. 1402, 2006.

[32] L. Pauling and C. Coryell, "The magnetic properties and structure of hemoglobin, oxyhemoglobin and carbonmonoxyhemoglobin," *Proc. Natl. Acad. Sci U.S.A.*, vol. 22, no. 4, pp. 210–236, 1936.

[33] K. R. Thulborn, J. C. Waterton, P. M. Matthews, and G. K. Radda, "Oxygenation dependence of the transverse relaxation time of water protons in whole blood at high field," *Biochimica et Biophysica Acta (BBA) - General Subjects*, vol. 714, no. 2, pp. 265 – 270, 1982.

[34] P. Bandettini, E. Wong, R. Hinks, R. Tikofsky, and J. Hyde, "Time course epi of human brain function during task activation," *Magnetic Resonance in Medicine*, vol. 25, no. 2, pp. 390–397, 1992.

[35] S. Ogawa, D. Tank, R. Menon, J. Ellermann, S. Kim, H. Merkle, and K. Ugurbil, "Intrinsic signal changes accompanying sensory stimulation: functional brain mapping with magnetic resonance imaging," *Proceedings of the National Academy of Sciences*, vol. 89, no. 13, pp. 5951–5955, 1992.

[36] C. Roy and C. Sherrington, "On the Regulation of the Blood-supply of the Brain," *The Journal of Physiology*, vol. 11, no. 1-2, pp. 85–158.17, 1890.

[37] D. Attwell and C. Iadecola, "The neuronal basis of functional brain imaging signals," *Trends in Neurosciences*, vol. 25, no. 12, pp. 621–625, 2002.

[38] C. Mathiesen and K. Caesar and N. Akgören and M. Lauritzen, "Modification of activity-dependent increases of cerebral blood flow by excitatory

synaptic activity and spikes in rat cerebellar cortex," *The Journal of Physiology*, vol. 512, no. 2, pp. 555–566, 1998.

[39] N. Logothetis, J. Pauls, M. Augath, T. Trinath, and A. Oeltermann, "Neurophysiological investigation of the basis of the fMRI signal," *Nature*, vol. 412, no. 6843, pp. 15–157, 2001.

[40] K. Thomsen, N. Offenhauser, and M. Lauritzen, "Principle neuron spiking: neither necessary nor sufficient for cerebral blood flow in rat cerebellum," *The Journal of Physiology*, vol. 560, no. 1, pp. 181–189, 2004.

[41] F. Shellock, "Mrisafety.com, your information resource for mri safety, bioeffects and patient management." `http://www.mrisafety.com`, [accessed: 2014 2nd July].

[42] J. Schenck, "Safety of strong, static magnetic fields," *Journal of Magnetic Resonance Imaging*, vol. 12, no. 1, pp. 2–19, 2000.

[43] D. Schaefer, J. Bourland, and J. Nyenhuis, "Review of patient safety in time-varying gradient fields," *Journal of Magnetic Resonance Imaging*, vol. 12, no. 1, pp. 20–29, 2000.

[44] H. Berger, "Über das elektrenkephalogramm des menschen," *Archiv für Psychiatrie und Nervenkrankheiten*, vol. 87, no. 1, pp. 527–570, 1929.

[45] P. Nunez and R. Srinivasan, *Electric fields of the brain: the neurophysics of EEG*. Oxford University Press, 2nd ed., 2006.

[46] S. Sanei and J. Chambers, *EEG Signal Processing*. John Wiley & Sons, 2007.

[47] M. Megías, Z. Emri, T. Freund, and A. Gulyás, "Total number and distribution of inhibitory and excitatory synapses on hippocampal CA1 pyramidal cells," *Neuroscience*, vol. 102, no. 3, pp. 527–540, 2001.

[48] N. Spruston, "Pyramidal neurons: dendritic structure and synaptic integration," *Nature Review Neuroscience*, vol. 9, no. 3, pp. 206–221, 2008.

[49] R. Plonsey and R. Barr, *Bioelectricity: A Quantitative Approach.* Springer Science, 3rd ed., 2007.

[50] A. Hodgkin and A. Huxley, "A quantitative description of membrane current and its application to conduction and excitation in nerve," *The Journal of Physiology*, vol. 117, no. 4, pp. 500–544, 1952.

[51] J. Malmivuo and R. Plonsey, *Bioelectromagnetism - Principles and Applications of Bioelectric and Biomagnetic Fields.* Oxford University Press, web-version ed., 1995.

[52] C. Michel and D. Brandeis, "The Source and Temporal Dynamics of Scalp Electric Fields," in *Simultaneous EEG and fMRI: Recording, Analysis, and Application* (M. Ullsperger and S. Debener, eds.), pp. 3–19, Oxford University Press Inc., 2010.

[53] F. Lopes da Silva and A. Van Rotterdam, "Biophysical aspects of EEG and magnetoencephalogram generation," in *Electroencephalography: Basic Principles, Clinical Applications and Related Fields (5th Edition)* (E. Niedermeyer and F. L. da Silva, eds.), pp. 107–125, Lippincott Williams & Wilkins, 2005.

[54] H. Schwan and C. Kay, "Capacitive properties of body tissues," *Circulation Research*, vol. 5, no. 4, pp. 439–443, 1957.

[55] R. Plonsey and D. Heppner, "Considerations of quasi-stationarity in electrophysiological systems," *The Bulletin of mathematical biophysics*, vol. 29, no. 4, pp. 657–664, 1967.

[56] H. Schwan and C. Kay, "Specific resistance of body tissues," *Circulation Research*, vol. 4, no. 6, pp. 664–670, 1956.

[57] A. Kamp, G. Pfurtscheller, G. Edlinger, and F. L. da Silva, "Technological basis of eeg recording," in *Electroencephalography: Basic Principles, Clinical Applications and Related Fields (5th Edition)* (E. Niedermeyer and F. L. da Silva, eds.), pp. 127–138, Lippincott Williams & Wilkins, 2005.

[58] EASY CAP, "Small Equidistant 29-Channel-Arrangment." `http://www.easycap.de/easycap/e/electrodes/06_M22.htm`, [accessed: 2014 06th May].

[59] Brain Products GmbH., "EEG-fMRI Booklet." `http://www.brainproducts.com/filedownload.php?path=products/brochures\_material/EEG-fMRI-Booklet.pdf`, 2011.

[60] F. L. da Silva, "EEG: Origin and Measurement," in *EEG-fMRI: Physiological Basis, Technique and Applications* (C. Mulert and L. Lemieux, eds.), pp. 19–37, Springer, 2010.

[61] K. Mullinger, P. Castellone, and R. Bowtell, "Best current practice for obtaining high quality EEG data during simultaneous FMRI," *JoVE (Journal of Visualized Experiments)*, no. 76, pp. e50283–e50283, 2013.

[62] A. M. V. Rijn, A. Peper, and C. Grimbergen, "High-quality recording of bioelectric events," *Medical and Biological Engineering and Computing*, vol. 29, no. 4, pp. 433–440, 1991.

[63] B. Winter and J. Webster, "Reduction of interference due to common-mode voltage in biopotential amplifiers," *IEEE Transactions on Biomedical Engineering*, vol. 30, no. 1, pp. 58–62, 1983.

[64] Brain Products GmbH., "Brain Products GmbH / Products & Applications / BrainAmp MR plus." `http://www.brainproducts.com/productdetails.php?id=6`, [accessed: 2014 2nd Feb].

[65] B. Winter and J. Webster, "Driven-right-leg circuit design," *IEEE Transactions on Biomedical Engineering*, vol. 30, no. 1, pp. 62–6, 1983.

[66] W. Walter and M. Camb, "The location of cerebral tumours by electroencephalography," *The Lancet*, vol. 2, no. 5893, pp. 305–308, 1936.

[67] D. Brandeis, C. Michel, and F. Amzica, "From Neuronal Activity to Scalp Potential Fields," in *Electrical Neuroimaging* (C. Michel, T. Koenig, D. Bran-

deis, L. Gianotti, and J. Wackermann, eds.), pp. 1–24, Cambridge University Press, 2009.

[68] W. Walter and V. Dovey, "Electroencephalography in cases of sub-cortical tumour," *J. Neurol. Neurosurg. Psychiatry*, vol. 7, no. 3–4, pp. 57–65, 1944.

[69] E. Niedermeyer, "The Normal EEG of the Waking Adult," in *Electroencephalography: Basic Principles, Clinical Applications and Related Fields (5th Edition)* (E. Niedermeyer and F. L. da Silva, eds.), pp. 167–192, Lippincott Williams & Wilkins, 2005.

[70] A. Snyder and M. Raichle, "Studies of the Human Brain Combining Functional Neuroimaging and Electrophysiological Methods," in *Simultaneous EEG and fMRI: Recording, Analysis, and Application* (M. Ullsperger and S. Debener, eds.), pp. 47–65, Oxford University Press Inc., 2010.

[71] H. Laufs, "A personalized history of EEG-fMRI integration," *NeuroImage*, vol. 62, pp. 1056–1067, 2012. 20 YEARS OF fMRI 20 YEARS OF fMRI.

[72] L. Lemieux, A. Salek-Haddadi, O. Josephs, P. Allen, N. Toms, C. Scott, K. Krakow, R. Turner, and D. Fish, "Event-Related fMRI with Simultaneous and Continuous EEG: Description of the Method and Initial Case Report," *NeuroImage*, vol. 14, no. 3, pp. 780–787, 2001.

[73] A. Salek-Haddadi, M. Merschhemke, L. Lemieux, and D. Fish, "Simultaneous EEG-Correlated Ictal fMRI," *NeuroImage*, vol. 16, no. 1, pp. 32–40, 2002.

[74] J. Baudewig, H. Bittermann, W. Paulus, and J. Frahm, "Simultaneous EEG and functional MRI of epileptic activity: a case report," *Clinical Neurophysiology*, vol. 112, no. 7, pp. 1196–1200, 2001.

[75] H. Laufs and R. Thornton, "Clinical Applications: Epilepsy," in *Simultaneous EEG and fMRI: Recording, Analysis, and Application* (M. Ullsperger and S. Debener, eds.), pp. 295–310, Oxford University Press Inc., 2010.

[76] R. Goldman, J. Stern, J. E. Jr., and M. Cohen, "Simultaneous EEG and fMRI of the alpha rhythm," *NeuroReport*, vol. 13, no. 18, pp. 2487–2492, 2002.

[77] B. Feige, K. Scheffler, F. Esposito, F. D. Salle, J. Hennig, and E. E. Seifritz, "Cortical and subcortical correlates of electroencephalographic alpha rhythm modulation," *Journal of Neurophysiology*, vol. 93, no. 5, pp. 2864–2872, 2005.

[78] J. de Munck, S. Gonçalves, L. Huijboom, J. Kuijer, P. Pouwels, R. Heethaar, and F. L. da Silva, "The hemodynamic response of the alpha rhythm: An EEG/fMRI study," *NeuroImage*, vol. 35, no. 3, pp. 1142–1151, 2007.

[79] H. Laufs, K. Krakow, P. Sterzer, E. Eger, A. Beyerle, A. Salek-Haddadi, and A. Kleinschmidt, "Electroencephalographic signatures of attentional and cognitive default modes in spontaneous brain activity fluctuations at rest," *Proceedings of the National Academy of Sciences*, vol. 100, no. 19, pp. 11053–11058, 2003.

[80] H. Laufs, A. Kleinschmidt, A. Beyerle, E. Eger, A. Salek-Haddadi, C. Preibisch, and K. Krakow, "EEG-correlated fMRI of human alpha activity," *NeuroImage*, vol. 19, no. 4, pp. 1463–1476, 2003.

[81] T. Eichele, K. Specht, M. Moosmann, M. Jongsma, R. Quiroga, H. Nordby, and K. Hugdahl, "Assessing the spatiotemporal evolution of neuronal activation with single-trial event-related potentials and functional MRI," *Proceedings of the National Academy of Sciences of the United States of America*, vol. 102, no. 49, pp. 17798–17803, 2005.

[82] V. Calhoun, T. Adali, G. Pearlson, and K. Kiehl, "Neuronal chronometry of target detection: Fusion of hemodynamic and event-related potential data," *NeuroImage*, vol. 30, no. 2, pp. 544–553, 2006.

[83] G. Iannetti and R. Wise, "BOLD functional MRI in disease and pharmacological studies: room for improvement?," *Magnetic Resonance Imaging*, vol. 25, no. 6, pp. 978–988, 2007.

[84] I. Gutberlet, "Recording EEG Signals Inside the MRI," in *Simultaneous EEG and fMRI: Recording, Analysis, and Application* (M. Ullsperger and S. Debener, eds.), pp. 69–83, Oxford University Press Inc., 2010.

[85] K. Mullinger, M. Brookes, C. Stevenson, P. Morgan, and R. Bowtell, "Exploring the feasibility of simultaneous electroencephalography/functional magnetic resonance imaging at 7 T," *Magnetic Resonance Imaging*, vol. 26, no. 7, pp. 968–977, 2008.

[86] I. Neuner, T. Warbrick, J. Arrubla, J. Felder, A. Celik, M. Reske, F. Boers, and N. J. Shah, "EEG acquisition in ultra-high static magnetic fields up to 9.4 T," *NeuroImage*, vol. 68, pp. 214–220, 2013.

[87] L. Lemieux, P. Allen, F. Franconi, M. Symms, and D. Fish, "Recording of EEG during fMRI Experiments Patient Safety," *Magnetic Resonance in Medicine*, vol. 38, no. 6, pp. 943–952, 1997.

[88] J. Ives, S. Warach, F. Schmitt, R. Edelman, and D. Schomer, "Monitoring the patient's EEG during echo planar MRI," *Electroencephalography and Clinical Neurophysiology*, vol. 87, no. 6, pp. 417 – 420, 1993.

[89] T. Stevens, J. Ives, L. Klassen, and R. Bartha, "MR compatibility of EEG scalp electrodes at 4 tesla," *Journal of Magnetic Resonance Imaging*, vol. 25, no. 4, pp. 872–877, 2007.

[90] K. Mullinger, S. Debener, R. Coxon, and R. Bowtell, "Effects of simultaneous EEG recording on MRI data quality at 1.5, 3 and 7 tesla," *International Journal of Psychophysiology*, vol. 67, no. 3, pp. 178 – 188, 2008.

[91] K. Mullinger and R. Bowtell, "Influence of EEG Equipment on MR Image Quality," in *Simultaneous EEG and fMRI: Recording, Analysis, and Application* (M. Ullsperger and S. Debener, eds.), pp. 107–117, Oxford University Press Inc., 2010.

[92] C. Klein, J. Hänggi, and L.Jäncke, "The influence of a high-density eeg cap on t1- and t2*-weighted mr images," Presented at the International Conference on Basic and Clinical Multimodal Imaging (BaCI), Geneva, 2013.

[93] Q. Luo and G. Glover, "Influence of dense-array eeg cap on fmri signal," *Magnetic Resonance in Medicine*, vol. 68, no. 3, pp. 807–815, 2012.

[94] W. Yan, K. Mullinger, M. Brookes, and R. Bowtell, "Understanding gradient artefacts in simultaneous EEG/fMRI," *NeuroImage*, vol. 46, no. 2, pp. 459–471, 2009.

[95] J. Felblinger, J. Slotboom, R. Kreis, and B. Jung, "Restoration of Electrophysiological Signals Distorted by Inductive Effect of Magnetic Field Gradients During MR Sequences," *Magentic Resonance in Medicine*, vol. 41, no. 4, pp. 715–721, 1999.

[96] F. Huang-Hellinger, H. Breiter, G. McCormack, M. Cohen, K. Kwong, J. Sutton, R. Savoy, R. Weisskoff, T. Davis, J. Baker, J. Belliveau, and B. Rosen, "Simultaneous functional magnetic resonance imaging and electrophysiological recording," *Human Brain Mapping*, vol. 3, no. 1, pp. 13–23, 1995.

[97] R.M. Müri, J. Felblinger, K. Rösler, B. Jung, C. Hess, and C. Boesch, "Recording of Electrical Brain Activity in Magnetic Resonance Environment: Distorting Effects of the Static Magnetic Field," *Magnetic Resonance in Medicine*, vol. 39, no. 1, pp. 18–22, 1998.

[98] E. L. Reilly, "Eeg recording and operation of the apparatus," in *Electroencephalography: Basic Principles, Clinical Applications and Related Fields (5th Edition)* (E. Niedermeyer and F. L. da Silva, eds.), pp. 139–160, Lippincott Williams & Wilkins, 2005.

[99] P. LeVan, J. Maclaren, M. Herbst, R. Sostheim, M. Zaitsev, and J. Hennig, "Ballistocardiographic artifact removal from simultaneous EEG-fMRI using an optical motion-tracking system," *NeuroImage*, vol. 75, pp. 1–11, 2013.

[100] K. Anami, O. Saitoh, M. Yumoto, F. Tanaka, Y. Kawagoe, T. Ohnishi, and H. Matsuda, "Reduction of ballistocardiogram with a vacuum head-fixating system during simultaneous fmri and multi-channel monopolar EEG recording," *International Congress Series*, vol. 1232, pp. 427–431, 2002.

[101] W. Nakamura, K. Anami, T. Mori, O. Saitoh, A. Cichocki, and S. Amari, "Removal of ballistocardiogram artifacts from simultaneously recorded eeg and fmri data using independent component analysis," *Biomedical Engineering, IEEE Transactions on*, vol. 53, no. 7, pp. 1294–1308, 2006.

[102] S. Debener, K. Mullinger, R. Niazy, and R. Bowtell, "Properties of the ballistocardiogram artefact as revealed by EEG recordings at 1.5, 3 and 7 t static magnetic field strength," *International Journal of Psychophysiology*, vol. 67, no. 3, pp. 189–199, 2008.

[103] T. Eichele, M. Moosmann, L. Wu, I. Gutberlet, and S. Debener, "Removal of MRI Artifacts from EEG Recordings," in *Simultaneous EEG and fMRI: Recording, Analysis, and Application* (M. Ullsperger and S. Debener, eds.), pp. 95–106, Oxford University Press Inc., 2010.

[104] J. Sijbers, I. Michiels, M. Verhoye, J. V. Audekerke, A. V. der Linden, and D. V. Dyck, "Restoration of MR-induced artifacts in simultaneously recorded MR/EEG data," *Magnetic Resonance Imaging*, vol. 17, no. 9, pp. 1383–1391, 1999.

[105] R. Feynman, R. Leighton, and M. Sands, *Feynman Lectures on Physics*. Basic Books, the new millennium ed., 2011.

[106] I. Grant and W. Phillips, *Electromagnetism*. John Wiley & Sons, 2nd ed., 1990.

[107] T. Tenforde, "Magnetically induced electric fields and currents in the circulatory system," *Progress in Biophysics and Molecular Biology*, vol. 87, no. 2–3, pp. 279–288, 2005.

[108] S. Debener, C. Kranczioch, and I. Gutberlet, "Eeg quality: Origin and reduction of the eeg cardiac-related artefact," in *EEG-fMRI: Physiological Basis, Technique and Applications* (C. Mulert and L. Lemieux, eds.), pp. 135–151, Springer, 2010.

[109] K. Mullinger, W. Yan, and R. Bowtell, "Reducing the gradient artefact in simultaneous eeg-fmri by adjusting the subject's axial position," *NeuroImage*, vol. 54, no. 3, pp. 1942 – 1950, 2011.

[110] M. Chowdhury, K. Mullinger, and R. Bowtell, "Simultaneous eeg-fmri: Gradient artefact reduction through cabling configuration.," Presented at the 20th Annual Meeting of the ISMRM, Melbourne, 2012.

[111] K. Anami, T. Mori, F. Tanaka, Y. Kawagoe, J. Okamoto, M. Yarita, T. Ohnishi, M. Yumoto, H. Matsuda, and O. Saitoh, "Stepping stone sampling for retrieving artifact-free electroencephalogram during functional magnetic resonance imaging," *NeuroImage*, vol. 19, no. 2, pp. 281–295, 2003.

[112] M. Laudon, J. Webster, R. Frayne, and T. Grist, "Minimizing interference from magnetic resonance imagers during electrocardiography," *Biomedical Engineering, IEEE Transactions on*, vol. 45, pp. 160–164, Feb 1998.

[113] R. Masterton, D. Abbott, S. Fleming, and G. Jackson, "Measurement and reduction of motion and ballistocardiogram artefacts from simultaneous EEG and fMRI recordings," *NeuroImage*, vol. 37, no. 1, pp. 202–211, 2007.

[114] M. Chowdhury, K. Mullinger, P. Glover, and R. Bowtell, "Reference layer artefact subtraction (RLAS): A novel method of minimizing EEG artefacts during simultaneous fMRI," *NeuroImage*, vol. 84, pp. 307–319, 2014.

[115] K. Mullinger, M. Brookes, G. Geirsdottir, and R. Bowtell, "Average gradient artefact subtraction: the effect on neuronal signals," Presented at the Annual Meeting of the OHBM, Melbourne, 2008.

[116] H. Mandelkow, P. Halder, P. Boesiger, and D. Brandeis, "Synchronization facilitates removal of MRI artefacts from concurrent EEG recordings and

increases usable bandwidth," *NeuroImage*, vol. 32, no. 3, pp. 1120–1126, 2006.

[117] R. Becker, P. Ritter, M. Moosmann, and A. Villringer, "Visual evoked potentials recovered from fmri scan periods," *Human Brain Mapping*, vol. 26, no. 3, pp. 221–230, 2005.

[118] M. Moosmann, V. Schönfelder, K. Specht, R. Scheeringa, H. Nordby, and K. Hugdahl, "Realignment parameter-informed artefact correction for simultaneous EEG-fMRI recordings," *NeuroImage*, vol. 45, no. 4, pp. 1144–1150, 2009.

[119] F. Freyer, R. Becker, K. Anami, G. Curio, A. Villringer, and P. Ritter, "Ultrahigh-frequency EEG during fMRI: Pushing the limits of imaging-artifact correction," *NeuroImage*, vol. 48, no. 1, pp. 94–108, 2009.

[120] R. Niazy, C. Beckmann, G. Iannetti, J. Brady, and S. Smith, "Removal of FMRI environment artifacts from EEG data using optimal basis sets," *NeuroImage*, vol. 28, no. 3, pp. 720–737, 2005.

[121] P. Allen, G. Polizzi, K. Krakow, D. Fish, and L. Lemieux, "Identification of EEG Events in the MR Scanner: The Problem of Pulse Artifact and a Method for Its Subtraction," *NeuroImage*, vol. 8, no. 3, pp. 229–239, 1998.

[122] H. Xia, D. Ruan, and M. Cohen, "Separation and reconstruction of bcg and eeg signals during continuous eeg and fmri recordings," *Frontiers in Neuroscience*, vol. 8, no. 163, 2014.

[123] Q. Luo, X. Huang, and G. Glover, "Ballistocardiogram artifact removal with a reference layer and standard EEG cap," *Journal of Neuroscience Methods*, vol. 233, no. 0, pp. 137–149, 2014.

[124] C. Bénar, Y. Aghakhani, Y. Wang, A. Izenberg, A. Al-Asmi, F. Dubeau, and J. Gotman, "Quality of EEG in simultaneous EEG-fMRI for epilepsy," *Clinical Neurophysiology*, vol. 114, no. 3, pp. 569–580, 2003.

[125] E. Briselli, G. Garreffa, L. Bianchi, M. Bianciardi, E. Macaluso, M. Abbafati, M. Marciani, and B. Maraviglia, "An independent component analysis-based approach on ballistocardiogram artifact removing," *Magnetic Resonance Imaging*, vol. 24, no. 4, pp. 393–400, 2006.

[126] D. Mantini, M. Perrucci, S. Cugini, A. Ferretti, G. Romani, and C. D. Gratta, "Complete artifact removal for EEG recorded during continuous fMRI using independent component analysis," *NeuroImage*, vol. 34, no. 2, pp. 598–607, 2007.

[127] S. Debener, A. Strobel, B. Sorger, J. Peters, C. Kranczioch, A. Engel, and R. Goebel, "Improved quality of auditory event-related potentials recorded simultaneously with 3-T fMRI: Removal of the ballistocardiogram artefact," *NeuroImage*, vol. 34, no. 2, pp. 587–597, 2007.

[128] W. Yan, K. Mullinger, G. Geirsdottir, and R. Bowtell, "Physical modeling of pulse artefact sources in simultaneous EEG/fMRI," *Human Brain Mapping*, vol. 31, no. 4, pp. 604–620, 2010.

[129] M. Bencsik, R. Bowtell, and R. Bowley, "Electric fields induced in a spherical volume conductor by temporally varying magnetic field gradients," *Physics in Medicine and Biology*, vol. 47, no. 4, pp. 557–576, 2002.

[130] J. Maclaren, B. Armstrong, R. Barrows, K. Danishad, T. Ernst, C. Foster, K. Gumus, M. Herbst, I. Kadashevich, T. Kusik, Q. Li, C. Lovell-Smith, T. Prieto, P. Schulze, O. Speck, D. Stucht, and M. Zaitsev, "Measurement and correction of microscopic head motion during magnetic resonance imaging of the brain," *PLoS ONE*, vol. 7, p. e48088, 11 2012.

[131] A. Papoulis, *Probability, Random Variables, and Stochastic Processes*. McGraw Hill, 2nd ed., 1984.

[132] S. Kay, *Intuitive probability and random processes using MATLAB*. Springer, 2011.

[133] M. Koskinen and N. Vartiainen, "Removal of imaging artifacts in EEG during simultaneous EEG/fMRI recording: Reconstruction of a high-precision artifact template," *NeuroImage*, vol. 46, no. 1, pp. 160 – 167, 2009.

[134] M. Cohen, "EPI and Functional MRI." `http://www.brainmapping.org/MarkCohen/Papers/EPI-fMRI.html`, [accessed: 2014 19th September].

[135] A. Lutti, D. L. Thomas, C. Hutton, and N. Weiskopf, "High-resolution functional MRI at 3T: 3D/2D echo-planar imaging with optimized physiological noise correction," *Magnetic Resonance in Medicine*, vol. 69, no. 6, pp. 1657–1664, 2013.

[136] P. Ritter, R. Becker, F. Freyer, and A. Villringer, "Eeg quality: The image acquisition artefact," in *EEG-fMRI: Physiological Basis, Technique and Applications* (C. Mulert and L. Lemieux, eds.), pp. 153–171, Springer, 2010.

[137] H. Laufs, J. Daunizeau, D. Carmichael, and A. Kleinschmidt, "Recent advances in recording electrophysiological data simultaneously with magnetic resonance imaging," *NeuroImage*, vol. 40, no. 2, pp. 515–528, 2008.

[138] M. Patel, A. Blum, J. Pearlman, N. Yousuf, J. Ives, S. Saeteng, D. Schomer, and R. Edelman, "Echo-Planar Functional MR Imaging of Epilepsy with Concurrent EEG Monitoring," *American Journal of Neuroradiology*, vol. 20, no. 10, pp. 1916–1919, 1999.

[139] J. Gotman, C. Bénar, and F. Dubeau, "Combining EEG and FMRI in epilepsy: methodological challenges and clinical results," *Journal of Clinical Neurophysiology*, vol. 21, no. 4, pp. 229–240, 2004.

[140] K. Hamandi, A. Salek-Haddadi, D. Fish, and j. L. Lemieux, "EEG/functional MRI in epilepsy: the Queen Square experience,"

[141] K. Krakow, D. Messina, L. Lemieux, J. Duncan, and D. Fish, "Functional MRI activation of individual interictal epileptiform spikes," *Neuroimage*, vol. 13, no. 3, pp. 502–505, 2001.

[142] A. Al-Asmi, C. Bénar, D. Gross, Y. Khani, F. Andermann, B. Pike, F. Dubeau, and J. Gotman, "fMRI activation in continuous and spike-triggered EEG–fMRI studies of epileptic spikes," *Epilepsia*, vol. 44, no. 10, pp. 1328–1339, 2003.

[143] A. Liston, J. D. Munck, K. Hamandi, H. Laufs, P. Ossenblok, J. Duncan, and L. Lemieux, "Analysis of EEG–fMRI data in focal epilepsy based on automated spike classification and Signal Space Projection," *Neuroimage*, vol. 31, no. 3, pp. 1015–1024, 2006.

[144] A. Salek-Haddadi, B. Diehl, K. Hamandi, M. Merschhemke, A. Liston, K. Friston, J. Duncan, D. Fish, and L. Lemieux, "Hemodynamic correlates of epileptiform discharges: an EEG-fMRI study of 63 patients with focal epilepsy," *Brain research*, vol. 1088, no. 1, pp. 148–166, 2006.

[145] C. Grova, J. Daunizeau, E. Kobayashi, A. Bagshaw, J. Lina, F. Dubeau, and J. Gotman, "Concordance between distributed EEG source localization and simultaneous EEG-fMRI studies of epileptic spikes," *Neuroimage*, vol. 39, no. 2, pp. 755–774, 2008.

[146] A. Bragin, J. Engel, C. Wilson, I. Fried, and G. Buzsáki, "High-frequency oscillations in human brain," *Hippocampus*, vol. 9, no. 2, pp. 137–142, 1999.

[147] J. Jacobs, P. LeVan, R. Chander, J. Hall, F. Dubeau, and J. Gotman, "Interictal high-frequency oscillations (80âĂŞ500 Hz) are an indicator of seizure onset areas independent of spikes in the human epileptic brain," *Epilepsia*, vol. 49, no. 11, pp. 1893–1907, 2008.

[148] J. Jacobs, M. Zijlmans, R. Zelmann, C. Chatillon, J. Hall, A. Olivier, F. Dubeau, and J. Gotman, "High-frequency electroencephalographic oscillations correlate with outcome of epilepsy surgery," *Annals of Neurology*, vol. 67, no. 2, pp. 209–220, 2010.

[149] L. Andrade-Valenca, F. Dubeau, F. Mari, R. Zelmann, and J. Gotman, "Interictal scalp fast oscillations as a marker of the seizure onset zone," *Neurology*, vol. 77, no. 6, pp. 524–531, 2011.

[150] K. Kobayashi, Y. Watanabe, T. Inoue, M. Oka, H. Yoshinaga, and Y. Ohtsuka, "Scalp-recorded high-frequency oscillations in childhood sleep-induced electrical status epilepticus," *Epilepsia*, vol. 51, no. 10, pp. 2190–2194, 2010.

[151] F. Pittau, F. Grouiller, L. Spinelli, M. Seeck, C. Michel, and S. Vulliemoz, "The role of functional neuroimaging in pre-surgical epilepsy evaluation," *Frontiers in neurology*, vol. 5, 2014.

[152] M. Centeno and D. Carmichael, "Network connectivity in epilepsy: resting state fMRI and EEG–fMRI contributions," *Frontiers in neurology*, vol. 5, 2014.

[153] B. Biswal, F. Z. Yetkin, V. Haughton, and J. Hyde, "Functional connectivity in the motor cortex of resting human brain using echo-planar mri," *Magnetic Resonance in Medicine*, vol. 34, no. 4, pp. 537–541, 1995.

[154] J. de Munck, S. GonÃğalves, R. Mammoliti, R. Heethaar, and F. L. da Silva, "Interactions between different EEG frequency bands and their effect on alphaâĂŞfMRI correlations," *NeuroImage*, vol. 47, no. 1, pp. 69–76, 2009.

[155] A. Giraud, A. Kleinschmidt, D. Poeppel, T. Lund, R. Frackowiak, and H. Laufs, "Endogenous cortical rhythms determine cerebral specialization for speech perception and production," *Neuron*, vol. 56, no. 6, pp. 1127–1134, 2007.

[156] N. Logothetis, "The neural basis of the blood–oxygen–level–dependent functional magnetic resonance imaging signal," *Philosophical Transactions of the Royal Society B: Biological Sciences*, vol. 357, no. 1424, pp. 1003–1037, 2002.

[157] J. Niessing, B. Ebisch, K. Schmidt, M. Niessing, W. Singer, and R. Galuske, "Hemodynamic signals correlate tightly with synchronized gamma oscillations," *Science*, vol. 309, no. 5736, pp. 948–951, 2005.

[158] "Coupling between neuronal firing, field potentials, and FMRI in human auditory cortex,"

[159] J. Lachaux, P. Fonlupt, P. Kahane, L. Minotti, D. Hoffmann, O. Bertrand, and M. Baciu, "Relationship between task-related gamma oscillations and BOLD signal: New insights from combined fMRI and intracranial EEG," *Human brain mapping*, vol. 28, no. 12, pp. 1368–1375, 2007.

[160] A. Brovelli, J. Lachaux, P. Kahane, and D. Boussaoud, "High gamma frequency oscillatory activity dissociates attention from intention in the human premotor cortex," *Neuroimage*, vol. 28, no. 1, pp. 154–164, 2005.

[161] S. Horovitz, M. Fukunaga, J. de Zwart, P. van Gelderen, S. Fulton, T. Balkin, and J. Duyn, "Low frequency BOLD fluctuations during resting wakefulness and light sleep: A simultaneous EEG-fMRI study," *Human brain mapping*, vol. 29, no. 6, pp. 671–682, 2008.

[162] J. Jorge, W. van der Zwaag, and P. Figueiredo, "EEGâĂŞfMRI integration for the study of human brain function," *NeuroImage*, vol. 102, no. 0, pp. 24–34, 2014.

[163] S. Debener, M. Ullsperger, M. Siegel, K. Fiehler, D. V. Cramon, and A. Engel, "Trial-by-trial coupling of concurrent electroencephalogram and functional magnetic resonance imaging identifies the dynamics of performance monitoring," *The Journal of Neuroscience*, vol. 25, no. 50, pp. 11730–11737, 2005.

[164] K. Mullinger, S. Mayhew, A. Bagshaw, R. Bowtell, and S. Francis, "Poststimulus undershoots in cerebral blood flow and BOLD fMRI responses are modulated by poststimulus neuronal activity," *Proceedings of the National Academy of Sciences*, vol. 110, no. 33, pp. 13636–13641, 2013.

[165] A. Delorme and S. Makeig, "EEGLAB: an open source toolbox for analysis of single-trial EEG dynamics including independent component analysis," *Journal of Neuroscience Methods*, vol. 134, no. 1, pp. 9–21, 2004.